# Attractive Electrostatic Self-Assembly of Ordered and Disordered Heterogeneous Colloids

by

Garry R. Maskaly

Bachelor of Science, Materials Science and Engineering
Massachusetts Institute of Technology, 2000

Submitted to the Department of Materials Science and Engineering in Partial Fulfillment
of the Requirements for the Degree of

Doctor of Philosophy in Materials Science and Engineering

at the

MASSACHUSETTS INTITUTE OF TECHNOLOGY

FEBRUARY 2005

© 2005 Massachusetts Institute of Technology. All Rights Reserved.

Signature of Author……………………………………………………………………
Department of Materials Science and Engineering
September 22, 2004

Certified by…………………………………………………………………………
Yet-Ming Chiang
Kyocera Professor of Ceramics
Thesis supervisor

Certified by…………………………………………………………………………
W. Craig Carter
Lord Foundation Professor of Materials Science and Engineering
Thesis supervisor

Accepted by…...……………………………………………………………………
Carl V. Thompson II
Stavros Salapatas Professor of Materials Science and Engineering
Chair, Departmental Committee on Graduate Students

# Attractive Electrostatic Self-Assembly of Ordered and Disordered Heterogeneous Colloids

By

Garry Russell Maskaly

Submitted to the Department of Materials Science and Engineering
on September 22nd, 2004 in partial fulfillment of the
requirements for the degree of
Doctor of Philosophy in Materials Science

## Abstract

Ionic colloidal crystals are here defined as multicomponent ordered colloidal structures stabilized by attractive electrostatic interactions. These crystals are colloidal analogues to ionic materials including zincblende, rocksalt, cesium chloride, and fluorite. A thermodynamic study revealed that the screening ratio, charge ratio, and monodispersity are critical parameters in ionic colloidal crystal (ICC) formation. Experimentally, small ordered regions were observed under ideal thermodynamic conditions. However, no larger crystalline regions were found in these samples. The kinetics of ICC formation was studied using a variety of computational techniques, including Brownian dynamics, Monte Carlo, and a Newton's method solver. These techniques have each elucidated properties and processing conditions that are important to crystallization. The Brownian dynamics and Monte Carlo simulations showed that the previous experiments were highly undercooled. Furthermore, a narrow crystallization window was found, demonstrating the need to create particle systems that meet the narrow parameter space where ICCs should be stable. Pair interaction potentials were evaluated for their accuracy using a Poisson-Boltzmann (PB) equation solver. The PB solver was also used to further refine crystalline formation energies so that systems can be more accurately tailored. A surprising result from the PB solver showed that the lowest formation energy occurs when the quantity of surface charges on both particles are equal. Although this result is not predicted by any colloidal pair potentials, it was verified experimentally. This further illustrates that thermal mobility in these systems can be sufficient to maintain a stable solution despite attractive electrostatic interactions. Tailoring particle systems to balance the thermal and electrostatic interactions should allow widespread crystallization. However, these conditions require highly monodisperse particles to be fabricated with controlled surface charge and sizes. Currently these particles are not widely available and further research in this area should aid in the full realization of the ICC concept. In conclusion, all results are integrated to predict which particle systems should be produced to allow the formation of large ordered structures.

**Keywords:** Ionic colloidal crystal, Colloidal crystal, Heterocoagulation, Self-assembly, Electrostatic forces, Brownian dynamics, Charge ratio, Colloid

# Acknowledgements

The last several years have been a process for which I am very thankful. The process has had its ups and downs and while I have learned a great deal about colloidal science and doing research, I am most thankful for the growth of my faith in my Lord and Savior Jesus Christ throughout this time. At the start, I trusted in the Lord for my eternal salvation, however, I trusted in myself for many things of this world. When things were not going smoothly and I was in doubt about finishing, I brought upon myself a lot of anxiety and some sleepless nights. I knew in my mind that I could trust in the Lord and His promises, but I did not feel it in my heart. In the deepest depths of this experience, I found that indeed I can trust in His Word: *"And we know that God causes all things to work together for good to those who love God, to those who are called according to His purpose.*" (Romans 8:28 NASB) I now know in my heart that this is Truth. While all things may not work together exactly how I desire, I know that I can trust that all things will work for the good despite how dark they may look at the time. I trust in this just as I know that I am a sinner in need of a Savior, *"for all have sinned and fall short of the glory of God"* (Romans 3:23 NASB) However, despite this sin, through faith in my Savior, I know that my sins are forgiven, "*For it is by grace you have been saved, through faith--and this not from yourselves, it is the gift of God*" (Ephesians 2:8 NASB) I am very grateful that I now know in my heart that despite my failures, I can trust the Lord in all things, especially for my eternal salvation.

Secondly, I am thankful to my wife Karlene for all of her loving support. She was always there to lift me up when I was down. She stayed up many late nights reading page after page of this thesis. Without her support I would not have finished this process. She has been the greatest wife I could have ever hoped for. I know that the Lord has blessed me by bringing her into my life. I know that even in leaving MIT, I will always be at home as long as she is with me.

I am indebted to my parents as well. I am so thankful for the upbringing they have given me. While I have grown a lot in my faith recently, I am thankful that I was raised knowing the Lord. I am also thankful for their support as I left home to attend MIT. They have always been there for me, even when at times I may have made it difficult for them.

I would also like to thank my advisors, Yet-Ming Chiang and W. Craig Carter. I greatly appreciate the freedom they have given me to pursue this project in the ways I wanted. From this experience, I have gained confidence in myself as a researcher and have learned how to do research. I am also grateful for the freedom to take some time to go to Los Alamos to pursue an internship. That experience gave me the connections to find my post-doctoral appointment and allowed me to find a wonderful place to live and raise a family.

I also would like to acknowledge the Deshpande Center and the Fannie and John Hertz Foundation for their funding support. I would like to especially recognize the Fannie and John Hertz Foundation and thank them for the freedom to pursue the research topic of my choice. This freedom allowed me to pursue a topic with little funding. Also, the connections I have gained through the Hertz Foundation have been invaluable in setting up my future career.

As with anything, the people you meet are often the most important part of an experience. This has been no exception and I would next like to thank all of the friends I have made during my graduate studies. Most importantly, I would like to thank all of the members of the Thursday night GCF Bible Study for their prayers and support. Thursday nights have been a great time for me to focus on what is truly important. I have learned a lot from all of you. In particular, I would like to thank Shandon Hart for his guidance in my walk with the Lord. While he and I had our differences early on in our relationship, the love of our Lord, which can overcome all, brought us together as brothers. I am grateful for the guidance he has given me and the encouragement, guidance, and admonishment I have received from him. May the Lord bless Colleen and him in everything they do.

Cody Friesen also is very deserving of thanks. He has been very helpful discussing many of the details of my work and giving me advice on how to proceed. He and Kristy have been great friends to Karlene and me. We have really enjoyed the many trips we have taken together. We look forward to many more in the future.

In closing, I would like to thank all members of the Chiang and Carter groups past and present for useful discussions and for the many times they helped me. In particular, Steven Tobias has been a great friend. I thank him for teaching me all of the intricacies of van der Waals interactions. I also thank him for dragging me out of work to hike from time to time, even if that did mean I dragged him up the Huntington Ravine Trail.

Scripture taken from the NEW AMERICAN STANDARD BIBLE®, © Copyright 1960, 1962, 1963, 1968, 1971, 1972, 1973, 1975, 1977, 1995 by The Lockman Foundation Used by permission. (www.lockman.com)

# Table of Contents

# List of Figures

# List of Tables

# Glossary of Symbols

---

## Lower-Case Symbols

$a$ – Particle radius
$a^*$ – Activity
$c$ – Concentration
$e_c$ – Electron charge
$f$ - Function
$h$ – Planck's constant
$k$ – Boltzmann's constant
$m$ – Mass
$n$ – Surface normal
$p$ – Momentum
$q$ – Charge
$r$ – Center-to-center separation distance
$t$ – Time
$v$ – Velocity
$z$ – Ion charge (in $e_c$)

## Capital Symbols

$A$ – Hamaker constant
$\langle A \rangle$ – Gaussian deviate
$D$ – Diffusivity of the particle
$E$ – Applied electric field
$F$ – Force
$G$ – Green's function
$H$ – Surface-to-surface separation distance
$I$ – Flux
$J$ – Jacobian
$K$ – Conductivity
$M_{sum}$ – Madelung summation
$N$ – Number
$N_A$ – Avagadro's number
$P$ – Pressure
$Q$ – Charge Ratio
$R$ – Ideal gas constant
$R_{\mathrm{size}}$ – Ratio of particle sizes
$R_{\Psi}$ – Ratio of particle surface potentials
$S$ – Entropy
$T$ – Temperature
$U$ – Interaction energy
$V$ – Volume

## Greek Symbols

$\alpha$ – Polarizability
$\beta$ – Stokes parameter ($6\pi a \eta$ for a sphere)
$\varepsilon_0$ – Permittivity of free space
$\varepsilon_r$ – Relative dielectric constant
$\varepsilon'$ – Real part of $\varepsilon_r$
$\varepsilon''$ – Imaginary part of $\varepsilon_r$
$\zeta$ – Zeta potential
$\eta$ – Viscosity
$\kappa$ – Debye parameter
$\mu$ – Mobility
$\mu_{chem}$ – Chemical potential
$\nu_0$ – Frequency (Hz)
$i\xi$ – Imaginery frequency
$\rho$ – Charge density
$\psi$ – Electrostatic potential
$\psi_s$ – Surface potential
$\omega$ – Frequency (in radians)
$\Lambda$ – Screening ratio
$\Lambda^0$ – Equivalent conductivity

# Chapter 1: Ionic Colloidal Crystals

There has been increasing interest in the scientific community over ordered colloidal materials, primarily due to their photonic properties [1-3]. These arrays are generally composed of a single particle type, severely limiting the number of possible structures. The optical properties of these structures are not as technologically useful as those of more complex structures such as zincblende, which has a complete photonic band gap [4]. Despite these limitations, large arrays of single component crystals have been produced through a variety of techniques. They can be stabilized in solution through repulsive interactions or condensed through drying front or fluid flow forces. Even with nonideal photonic properties, these materials have been used in a variety of devices, including lasers [5-10] and sensors [11-13].

In efforts to produce a wider variety of structures, various two-component approaches have been implemented, including the use of layer-by-layer growth with electrostatic repulsion [14] and hard-sphere interactions [15-23]. The resulting structures are those that occur in metallic systems, such as the AB, $AB_2$, and $AB_{13}$ structure types. While some of these structures have ionic analogues (such as CsCl), their stability does not arise from attractive electrostatic forces. Instead, these structures form through the maximization of the particles' vibrational entropy. This approach requires careful control of the overall particle volume fraction as well as the volume fractions of each particle type. Furthermore, this method typically produces multiple phases, with one phase often being a colloidal liquid phase, where particles have high mobility and move fluidly around one another.

In this thesis, the possibility of creating two-component colloidal crystals that are stabilized by attractive electrostatic interactions is studied. On the atomic scale, a mixture of positively and negatively charged ions of appropriate size and charge ratios rapidly form into complex order structures. However, an analogue to these ionic materials in the colloidal regime has not been realized. Yet, no self-consistent, convincing argument has thus far been put forward that prohibits such behavior in colloidal systems. Here it is proposed that a mixture of positively and negatively charged particles tailored within certain experimental constraints can be made to form a new type of colloidal crystal, an "ionic colloidal crystal" (ICC), stabilized by long range attractive forces.

A system utilizing these attractive forces should allow rapid crystallization while also opening up a more diverse phase space through the variation of system parameters, which tune these interactions. This enthalpy-driven, rather than entropy-driven, crystallization would yield a single robust equilibrium phase, similar to natural ionic materials. Structures that could be potentially realized include zincblende, which can have a large complete photonic band gap [4], and rutile, which has potential catalysis and filtration applications due to the presence of ordered channels in the structure. Figure 1.1 illustrates the ion channels in the ruthenium oxide structures relative to the dense packing of the FCC structure.

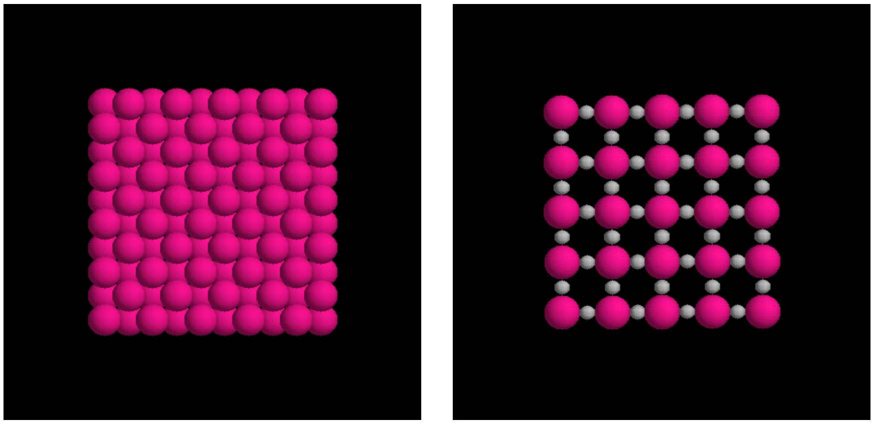

Figure 1.1 The FCC structure on the left is very dense with no clear channels through the materials. Some ICC structures, such as $ReO_3$ on the right, could exhibit fast diffusion pathways, which could make them of interest for catalysis applications where a high surface area with a minimum diffusion length is desired.

In this thesis, the conditions under which ICCs form are studied through a variety of computational and experimental approaches. It is shown that ICC formation does not occur if the system has a high charge asymmetry. However, it is also necessary to control the system kinetics as systems with ideal charge ratios can still form into metastable disordered heterocoagulates such as the low packing density non-crystalline reaction-limited cluster aggregation or diffusion-limited cluster aggregation structures that are often observed in heterocoagulating systems [24-26]. Control over the kinetics requires the limitation of the bond strength, as well as the possible application of forces, to prevent gelation. We find the conditions under which ICCs are energetically favorable and kinetically feasible at room temperature to be restrictive, suggesting that they are unlikely to occur accidentally. This may explain the lack of a previous observation of these structures.

Despite the difficulty in fabricating these materials, their technological benefits could be enormous. The complete photonic band gap of the zincblende structure makes it very attractive for photonic crystal lasing applications, where the lasing threshold is greatly reduced. The future realization of large scale ICCs will require careful attention to particle properties, and may require the production of particles with properties that are not readily available commercially.

Chapter 2 gives a background of colloidal forces with Chapter 3 applying those concepts directly to the problem of ionic colloidal crystals. The use of surfactants, the role of van der Waals forces, and the electrostatic interactions are discussed.

Chapter 4 uses a Madelung sum approach to calculate the regions where ionic colloidal crystals should be thermodynamically stable. Two dimensionless parameters, the screening ratio and charge ratio, are introduced that described the thermodynamic interactions. Low screening ratios, requiring either very low ionic strengths or small particles, are necessary to obtain the colloidal mobility necessary for ICC formation. Likewise, it is necessary to mitigate any other short range attractive forces. Finally, the impact of dispersity in particle sizes is examined through this model. A CV of 3% is desired to try to minimize the impact of dispersity.

Chapter 5 discusses some preliminary ICC experiments showing signs of preliminary ordering in a silica/polystyrene system. However, small clusters sizes indicated the need for kinetic strudies.

Chapter 6 and 7 discuss Brownian Dynamics and Monte Carlo results. Melting behavior of ICC systems are examined. The system in Chapter 5 is shown to be significantly undercooled and is therefore kinetically trapped. The mobility of such systems are also studied shown both critical nuclei sizes and glass transition behavior. A small region where crystallization should be expected is observed. Finally, means to improve nucleation in such systems are discussed.

Due to the small kinetic window studied in Chapter 7, Chapter 8 aims to more accurately evaluate the thermodynamic interactions in an ICC system. As all previous approaches use pair potentials, the Poisson-Boltzmann equation is solved over a periodic repeat unit. The maximum formation energy for a crystal is shown to occur when the amount of charges on both colloidal surfaces is equal. This result is not predicted by any colloidal pair potentials. The Yukawa potential is shown to be the most useful potential at low ionic strengths, while the Ohshima potential is more appropriate for high ionic strengths.

Chapter 9 utilizes the results from Chapter 8 to evaluate the impact of charge ratio in heterocoagulating systems. Heterocoagulation behavior is controlled through the variation of the relative charges on both particles. The results are shown to match very favorably with the charge ratio definition in Chapter 8. These results not only shown that charge ratio can control heterocoagulation behavior, but also indicate that thermal energy can be sufficient to prevent heterocoagulation in some systems. Both of these behaviors must be possible for ICC formation to occur.

# Chapter 2: An Introduction to Colloidal Forces

The understanding and engineering of colloidal materials has been important to the development of many technologies. The first scientific studies of these materials were conducted in the mid-17th century by Thomas Graham. Since then, there has been a large body of literature detailing the findings and theories of this subject. In this chapter, the salient points of colloidal forces are reviewed in the context of ionic colloidal crystals More detailed discussions of these topics are found in a variety of books [27-34]. *Foundations of Colloidal Science* by R.J. Hunter [27] and *Principles of Colloid and Surface Chemistry* by Paul C. Hiemenz and Raj Rajagopolan [28] are two excellent references which were primary source materials for this review.

Colloidal materials are dispersions where the suspended items are much larger than the other molecules in the system. The name colloid comes from a study of these materials by Thomas Graham in 1860 when he examined the behavior of various solutions passing through a dialysis membrane. Certain solutes would pass through the membrane, while others could not. One solute that could not diffuse through the dialysis membrane was a natural gum, after which Graham coined the term colloid (from the Greek word *kolla* meaning glue) to describe the materials trapped by the membrane. Because colloids are large particles, they are generally unable to pass through the small pores of a dialysis membrane. If the size of the particles is below approximately 1 nanometer, the dispersed particles become indistinguishable from a true solute, placing a lower bound on the size considered to be a colloid. At the other extreme, colloids are generally considered smaller than 1 micron because above that size, gravitational forces prevent the particles from staying dispersed. However, in practice, larger particles can remain dispersed and smaller particles of high density can rapidly settle indicating that a size-based definition may be less practical than a phenomenological criterion.

Systems that are considered colloidal materials are from a broad range of technological and natural origins. Milk, blood, paints, inks, and smog are all colloidal dispersions. Colloidal science has enabled the development of important technologies including food processing, xerography, ceramic processing, ore floatation, oil recovery, and pollution control methods. More recently, the behavior of nanoparticles, nanotubes, and proteins have been described by colloidal science. Colloidal particles have also modified for applications in rapid DNA sequencing [35]. One of the widest uses for colloidal materials is in making self-assembled photonic crystals [1-3, 36].

Colloidal suspensions can be composed of any phase combination except that of a gas in a gas: aerosols (solids or liquids dispersed in a gas), foams (gas dispersed in a solid or liquid), emulsions (liquid droplets dispersed in another liquid), and dispersions or sols (solids dispersed within a liquid). While different names are used to describe the various phase mixtures, their behavior all falls under the purview of colloidal science. For the remainder of this thesis, a colloidal suspension will refer to a solid dispersed in a liquid phase.

The interactions governing colloidal interactions can cause a wide variety of behavior. These interactions include van der Waals (or Hamaker) forces, depletion forces, steric repulsion, solvation forces, electrostatic forces, and random thermal fluctuations (Brownian motion). Colloidal properties can be modified by engineering these forces. While electrostatic forces are the focus of this thesis, an understanding of other colloidal interactions is necessary to evaluate and, if possible, mitigate their effects.

## 2.1 van der Waals Forces

The term van der Waals force is used to describe an ensemble of forces resulting from interactions of dipoles, quadrapoles, and higher multipoles. For further detail on these interactions, the review by French is recommended [37]. Three major components are generally considered to contribute to the overall interaction: dipole-dipole interactions (Keesom forces [38-40]), dipole-induced dipole interactions (Debye forces [41, 42]), and induced dipole-induced dipole interactions (London forces [43, 44]). In general, colloidal particles do not have permanent dipole moments. The van der Waals interactions are then typically dominated by London interactions. London dispersion forces are the interactions between spontaneous fluctuations of the electron cloud and dipoles induced by those fluctuations in nearby atoms. The form given by London for these interactions is shown in Equation 2.1 [44].

$$U = -\frac{3}{4}\frac{h\nu_0\alpha^2}{r^6} \tag{2.1}$$

After London's work, Hamaker published work correlating these forces to macroscopic bodies in an attempt to explain coagulation of colloidal systems [45]. In his work, it was assumed that London interactions for multiple oscillators could be summed pairwise. While these summations are complex, several cases can be solved explicitly. Of great importance to colloidal science was that of two spherical particles.

$$U_A = \frac{-A_{132}}{6}\left[\frac{2a_1a_2}{r^2-(a_1+a_2)^2} + \frac{2a_1a_2}{r^2-(a_1-a_2)^2} + \ln\left\{\frac{r^2-(a_1+a_2)^2}{r^2-(a_1-a_2)^2}\right\}\right] \tag{2.2}$$

At particle contact, the potential in Equation 2.2 is divergent. This results from the Hamaker's approximation that matter is homogeneous. A cutoff radius can be applied to limit the interaction energy. This cutoff radius is usually take to be on the order of the molecular radius (~0.1 nm). Hough and White showed that the surface energy can be used to approximate the value of this cutoff radius [46].

The value of the Hamaker constant can be difficult to calculate, but approximate values for various materials in vacuum are 100-300 zJ (zJ = $10^{-23}$ Joules) for metals, 10-30 zJ for ionic materials, and ~3 zJ for hydrocarbons. In a solvent, these values will be greatly reduced. While the interaction between two identical materials is always attractive, the interaction between different materials ($A_{132}$) can be either attractive or repulsive depending on the dielectric response function of the particles and of the solvent in which the particles are dispersed. If the materials are dispersed in a vacuum, the value of $A_{132}$ must be positive. A form for the Hamaker constant between dissimilar particles in an arbitrary solvent can be approximated from the Hamaker constants of the individual materials in vacuum.

$$A_{132} = \left( A_{1v1}^{1/2} - A_{3v3}^{1/2} \right)\left( A_{2v2}^{1/2} - A_{3v3}^{1/2} \right) \tag{2.3}$$

Modern dispersion theory presents a numerical solution to avoid many of the approximations in the calculation of $A_{132}$. While this theory only treats flat plates, the replacement of the Hamaker constant in Equation 2.2 by that obtained through modern theory yields good results [47]. The numerical summation presented by Ninham and Parsegian [48] provides insight into the magnitude of van der Waals interactions.

$$A_{132} = \frac{3kT}{2} \sum_{n=0}^{\infty}{}' \sum_{s=1}^{\infty} \left[ \frac{\varepsilon_1(i\xi_n) - \varepsilon_3(i\xi_n)}{\varepsilon_1(i\xi_n) + \varepsilon_3(i\xi_n)} \right]^s \left[ \frac{\varepsilon_2(i\xi_n) - \varepsilon_3(i\xi_n)}{\varepsilon_2(i\xi_n) + \varepsilon_3(i\xi_n)} \right]^s \Big/ s^3 \tag{2.4}$$

The prime on the first summation denotes that the first term of the sum should be halved. The dielectric constants are all evaluated at $i\xi$, which is obtained from the Kramers-Kronig relation.

$$\varepsilon(i\xi) = \varepsilon_0 \left( 1 + \frac{2}{\pi} \int_0^{\infty} \frac{\omega \varepsilon_r''(\omega)}{\omega^2 + \xi^2} d\omega \right) \tag{2.5}$$

Figure 2-1 (after Hunter, page 557) shows the comparison of $\varepsilon''(\omega)$, $\varepsilon'(\omega)$, and $\varepsilon(i\xi)$. In Equation 2.4, the evaluated points of the dielectric constant are discretely sampled at the frequencies shown in Equation 2.6.

$$\xi_n = \left[ 2\pi kT / \hbar \right] n \tag{2.6}$$

As per Hunter Appendix A1, these frequencies are the only ones that satisfy the dispersion condition. The spacing of these frequencies at 300K is on the order of $3\times10^{14}$

rad/s. At large n, the dielectric constant of all materials falls to 1. Therefore, the higher-order terms in Equation 2.4 approach zero. Practically, this limits the number of terms necessary for the summation to converge. Likewise, the summation over *s* converges rapidly, thus requiring few iterations of the second summation. Due to that large spacing of relevant frequencies, dielectric properties across the ultraviolet and visible regimes are the most significant. The Tabor-Winterton approximation [49] assumes that the dielectric response functions do not change relative to one another. The dielectric constant is evaluated only in visible regime and treated as a constant (the square of the index of refraction). However, it must be verified that this is consistent with the dielectric behavior in the UV regime, otherwise large errors, even errors in the sign of the Hamaker constant, can be incurred.

The relative dielectric response function values for a materials system give insight into the strength of the Hamaker interactions. Materials with very similar dielectric response functions have negligible Hamaker interactions. Also, if the dielectric response function of the solvent is between that for the end members, the Hamaker interaction of the two plates is repulsive. While repulsive Hamaker forces are rare, these forces do give rise to the interesting properties of materials such as Teflon, which is repulsive with most materials when in a solvent.

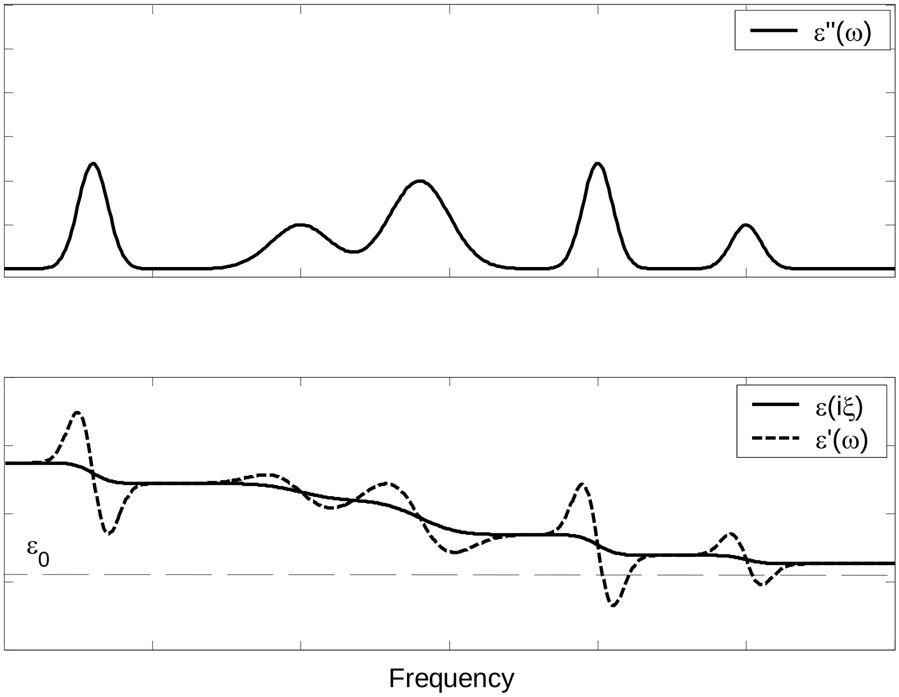

Figure 2.1: The values of the real and imaginary components of the dielectric constant are shown relative to dielectric constant at an imaginary frequency (ε(iξ)). Note that the ε'(ω) and ε(iξ) are nearly identical between resonant frequencies.

## 2.2 Steric and Solvation Forces

Steric and solvation forces result from size effects on the interactions of colloidal particles. Surfactants are commonly used to introduce steric interactions. Surfactants adsorb to the surface of a colloidal particle while leaving other interactions relatively unchanged. In a good solvent, a surfactant molecule elongates due to entropy. For particles to approach beyond the point where the surfactant molecules would overlap, the polymer chains would need to be compressed. This compression decreases the entropy of the system and thus acts as a repulsive force. Thus, these molecules limit the closest approach of particles to approximately two times the molecule length. At these separations, Hamaker forces are usually negligible for good solvents. The surfactant limits the rapid coagulation of a colloidal suspension. Surfactants are categorized into nonionic, anionic, and cationic. Nonionic surfactants only impose a short range steric interaction as they have no impact on the surface charge of the colloid, while anionic and cationic surfactants form a salt when dissolved and therefore carry some charge to the colloid surface, altering the electrostatic interactions.

Solvation forces have a similar origin, but are due to the presence of the solvent molecules rather than surfactants. These are especially relevant for the interaction of flat surfaces, where layers of solvent must move large distances during the close approach of the surfaces. Solvation forces may also increase the force necessary to separate particles in contact as solvent must rewet the two surfaces before the particles can be separated.

## 2.3 Depletion Forces

Depletion forces are the result of osmotic pressure from smaller particles on larger particles in a suspension. The smaller particles move more quickly under the thermal fluctuations in the system. These particles impinge on the large particles from all sides. When the larger particles come close enough together that they are separated by less than the small particle radius, the small particles can no longer impinge on the facing surfaces, but continue to bombard the external surfaces. In effect, this results in an osmotic pressure pushing the two large particles together. These forces can lead to interesting phase behavior including phase separation[50-54].

Generally, these depletion interactions are shorter range than electrostatic interactions in a colloidal suspension. However, they can be significant in a hard sphere colloidal system. Furthermore, these forces exist across a broad range of particle sizes, even beyond what is typically considered a colloidal particle. For the purposes of this thesis, the electrostatic forces are assumed to be substantially stronger than any depletion interactions.

## 2.4 Random Driving Forces

When a droplet containing colloidal particles of a few hundred nanometers in diameter are placed on a glass slide and observed at high magnification, the particle trajectories appear to be random with the particle making sharp jumps in seemingly random directions. This behavior, called Brownian motion, was first observed by Robert

Brown in an examination of pollen grains. Since those days, many scientists have tried to develop models to understand this behavior. In 1906, Einstein [55] and von Smoluchowski [56] developed a set of equations to describe this aspect of colloidal behavior. A summary of the derivation of the diffusion of colloidal particles is included below.

Colloidal particles in solution can be treated as a chemical species. The chemical driving force on a system of particles due to a gradient in chemical potential is given by Equation 2.7.

$$F_{chem} = -\frac{\nabla \mu_{chem}}{N_A} \tag{2.7}$$

From the definition of chemical potential, this force can be calculated in terms of the activity of the material.

$$\mu_{chem\,i} = \mu_{chem0} + RT\ln\left(a_i^{'}\right) \tag{2.8}$$

$$\nabla \mu_{chem\,i} = RT\nabla\left(\ln a_i^{*}\right) \tag{2.9}$$

$$\nabla \mu_{chem\,i} = RT\frac{\nabla a_i}{a_i} \tag{2.10}$$

$$F_{chem} = -\frac{RT}{N_A}\frac{\nabla a_i^{*}}{a_i^{*}} \tag{2.11}$$

At low concentrations in an ideal solution, the activity is closely approximated by the concentration of species.

$$F_{chem} = -\frac{RT}{N_A}\frac{\nabla c_i}{c_i} = -kT\frac{\nabla c_i}{c_i} \tag{2.12}$$

In a solution, the particles are not continually accelerated under such a force because a drag of some form is present. In a colloidal system, this drag is due to the Stokesian flow of liquid around the particles. Under these conditions, the terminal velocity can be determined through a force balance.

$$F_{chem} - F_{drag} = 0 \tag{2.13}$$

$$kT\frac{\nabla c_i}{c_i} - \beta v = 0 \tag{2.14}$$

$$v = \frac{kT}{\beta}\frac{\nabla c_i}{c_i} \tag{2.15}$$

The steady-state flux of particles under this force balance is this velocity multiplied by the concentration. This flux can be compared to the flux from Fick's First Law of Diffusion to find the particles' diffusivity.

$$I = vc_i = \frac{kT}{\beta}\nabla c_i \tag{2.16}$$

$$\frac{kT}{\beta}\nabla c_i = -D\nabla c_i \tag{2.17}$$

Solving for the diffusivity of the molecule gives the Einstein relation.

$$D = \frac{kT}{\beta} \tag{2.18}$$

For spherical particles, the Stokesian term takes on the simple form: 6πηa.

$$D = \frac{kT}{6\pi\eta a} \tag{2.19}$$

Fick's Second Law of Diffusion can now be applied to determine the spatial evolution of a large concentration of particles over time. For a constant diffusivity, the three-dimensional solution for a point source of magnitude $c_0$ with a zero flux boundary condition at infinity is a Gaussian distribution [57] with a standard deviation of the square root of 2*Dt*.

$$\frac{\partial c_i}{\partial t} = \nabla(D\nabla c_i) = D\nabla^2 c_i \tag{2.20}$$

$$c_i = \frac{c_0}{8(\pi Dt)^{3/2}}\exp\left(\frac{\left|\bar{r} - \bar{r_0}\right|^2}{4Dt}\right) \tag{2.21}$$

This solution can also be used to represent the probability for finding one particle a certain distance away from its starting point after a given amount of time.

## 2.5 Electrostatic Forces

Particle surfaces become charged in solution due to a chemical driving force for the charging species to either dissociate from the surface into solution or associate with the surface from solution. For ceramic particles, one charging mechanism is the dissolution of hydroxyl groups from the surface (leaving a positively charged surface) or the reaction of hydroxyl groups with the surface (creating a negatively charged surface). For a polymer system, charging is most commonly due to the ionization of initiators used in the fabrication of the particles, or through the dissolution of functional groups on the surface of the particle added during or after the polymerization. These groups are very diverse. They include sulfate and carboxyl groups (generally negatively charged at a neutral pH due to the dissolution of a hydrogen ion when in solution) and amine and amidine groups (generally positively charged due to the localization of hydrogen ions within them). Although other charging mechanisms exist, these are the ones most commonly encountered in monodisperse colloidal suspensions.

In a colloidal system, these charged particles are surrounded by small, highly-mobile ions. These ions include dissociated salts, self-dissociated solvent molecules, and counterions of the charges on the colloidal particles. These ions are much more mobile than the particles, allowing them to sample many energetic states. Thus, in the statistical mechanics treatment of this system, the salt ions are assumed to be ergotic. This allows the ions to be treated as a continuous charge distribution described spatially by a Boltzmann probability distribution around a fixed colloidal particle, rather than as a series of discrete charges. The units of concentration are number of ions per cubic meter.

$$\rho_i(r) = z_i e_c c_i^* \exp\left(-\frac{z_i e_c \psi}{kT}\right) \tag{2.22}$$

The Poisson equation (Equation 2.23) can be used to determine the electric field from this charge distribution.

$$\nabla^2 \psi = -\frac{\sum_i \rho_i}{\varepsilon_0 \varepsilon_r} \tag{2.23}$$

Substituting Equation 2.22 into 2.23 yields the Poisson-Boltzmann equation (Equation 2.24).

$$\nabla^2 \psi = -\frac{1}{\varepsilon_0 \varepsilon_r} \sum_i z_i e_c c_i^* \exp\left(-\frac{z_i e_c \psi}{kT}\right) \tag{2.24}$$

The first treatments of a charged surface with the Poisson-Boltzmann equation were performed independently by Gouy [58] and Chapman [59]. The resulting model for a system where the Poisson-Boltzmann equation holds is thus called the Gouy-Chapman model.

### 2.5.1 Boundary Conditions

The total surface charge is limited by the total number of sites that can become ionized. Additionally, continued surface charging is hindered by an electrostatic penalty for either the association of a charged species with a like charged particle or the separation of a charged species from a dissimilarly charged particle. The relative balance of these factors in the electrochemical potential creates three distinct cases of boundary conditions: constant charge distribution, constant potential, and charge regulating.

In the event that the chemical driving force overwhelms any electrostatic penalty for charging, all available sites on a particle surface will become charged. Further charging is prevented by a limitation in the number of sites, and discharging does not occur in the presence of a potential field due to the large chemical driving force. Thus, the particle can be treated as having a constant charge distribution boundary condition. Highly acidic or basic surface groups, such as those found on some latexes, are well approximated by this boundary condition [60].

Conversely, in the case of the constant potential boundary condition, the solution is considered to have an infinite source of ions and the particle surface is viewed as having an infinite number of available charging sites. Under these assumptions, the charging event does not change the chemical potential of a species in solution. Therefore, the chemical driving force also remains unchanged. As a result, the surface charges freely to maintain the local electrical potential at a constant value. Because the particle has an infinite number of charging sites, the surface is never saturated with ions, which would limit the degree to which the surface could charge.

The last type of boundary condition, charge regulating, is a result of a balance between the electrostatic and chemical potential components of the electrochemical potential of the system. This covers the region between the constant charge distribution and the constant potential boundary conditions. When the electrostatic potential field around a particle is altered in the presence of another particle, an applied field, or a wall, the amount of charge on the surface of the particle will change until the electrochemical potential is again balanced. Charge regulation models vary greatly is complexity. In the simplest case, it could incorporate a limited number of charging sites into the constant potential boundary condition. In one case, a nonlinearity in charging is considered where both the surface potential and the amount of charge of the surface change together [60, 61]. This coupling could be due to the charging event changing the chemical potential in the adjacentl solution.

The boundary condition behavior has a large impact on colloidal behavior. As the surface charge keeps many colloidal solutions stabilized, large variations can result in coagulation. The surface charge variations are evident in oxide systems where the surface charge ranges form negative to positive with pH variations. A simplified view of oxide particles in aqueous solutions at various pHs (shown in Figure 2-2). At either extreme of the pH range the particle surface is fully charged. Thus, a small change in the electrochemical potential does not change the surface condition because all available sites are charged. Alternatively, in the region near the isoelectric point (IEP), a change in either the chemical potential (through pH) or the electrostatic potential (through an applied field) would shift the amount of charge on the surface of the particle. In this case, a shift toward a higher activity for the hydrogen ions in the solution will drive more hydrogen to the surface, making the particle more positively charged and vice versa. A change in the local potential field is compensated by charging or discharging of the surface, allowing a constant surface potential to be maintained. In reality, the charging behavior is much more complex. Typically, the pH extremes have are not constant.

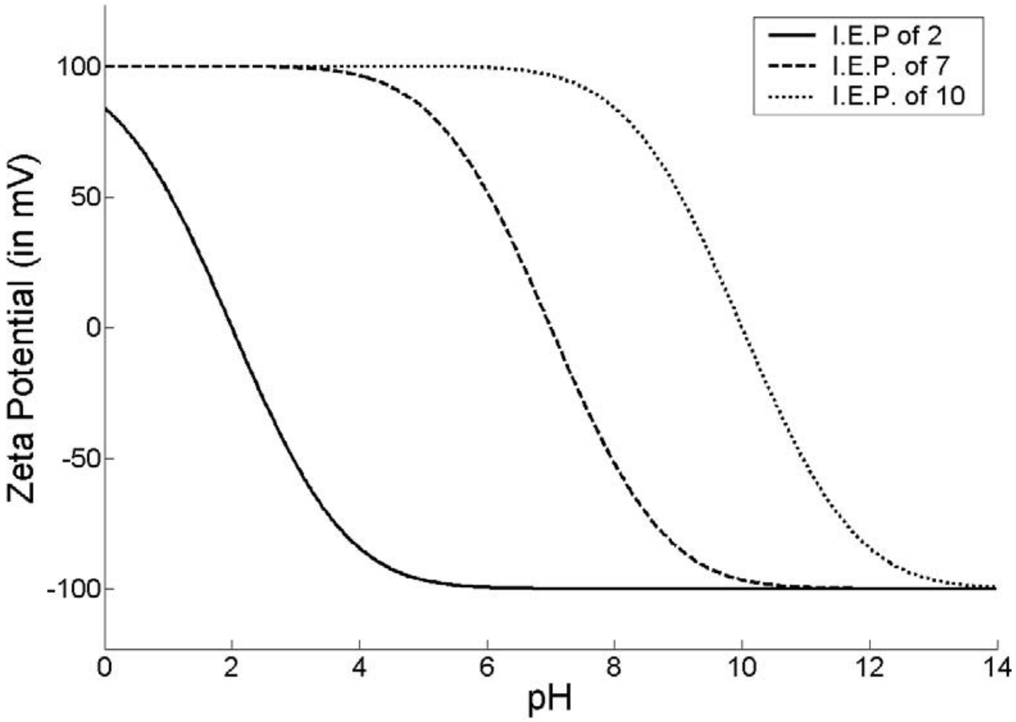

Figure 2.2: A simplified view of the zeta potential of three sample oxides is shown. At the pH extremes, the zeta potential approaches a constant value due to a limit on the number of available charging sites. In the intermediate regime, the zeta potential varies from positive to negative crossing the iso-electric point (IEP) where the net charge is zero.

The boundary condition choice is very important in trying to accurately model colloidal behavior. For an isolated particle, the constant surface potential and constant surface charge boundary conditions are identical. The variations occur when colloidal particles begin to interact. For identical particles, the choice of boundary conditions has some effect on the results, but the physical behavior is similar under both cases: the colloidal interactions are repulsive. However, considering the approach of two identical particles with a constant charge boundary condition, the electrostatic potential at the contact point would be close to twice the surface potential of the isolated particle. This makes the constant charge boundary condition result in potentials that are more highly repulsive than the constant potential boundary condition. Charge regulation models fall somewhere in between the two cases and generally depend on the approach velocity of the two particles [61].

For dissimilar particles, the choice becomes more significant. In the case of a constant potential boundary condition, dissimilar particles have an infinite energy at contact. Because the constant potential boundary condition model has no limitation on the number of charging sites, dissimilarly charge particles will continue to charge at the contact point due to the infinite electric field (fixed potential difference with a zero separation distance). Further charging of one surface will cause further charging of the other and will continue indefinitely as both surfaces will charge infinitely. If both particles have the same sign of charge, this result does not significantly alter the behavior of a suspension, as it will simply prevent the particles from coming into contact. However, for a system with dissimilar signs of surface charge, an infinite attraction occurs at contact, causing the surfaces to be permanently stuck together under this model. This model requires an infinite density of charging sites at the point of contact in order to hold the surface potentials on both surfaces constant. In practice, the physical situation of having an infinite number of charging sites is incorrect. Also, the constant potential boundary condition leads to $N^2$ image charges for an N-body system, making pair-wise summations inaccurate. This prevents accurate modeling of the kinetics of the system within a reasonable amount of simulation time.

The constant charge boundary condition does not have a divergent charge build up at contact. Positively and negatively charged particles would be electrostatically separable after a contact event. However, unlike the constant potential boundary condition, the constant charge boundary condition no longer screens the core of the particle from seeing any potential. The result is that the electrical potential is altered by the core of the particle. In the event that the core is identical in properties to the solution, the problem becomes easily solvable. However, for other more physical cores, the solution becomes very complex and first had an analytical solution published in 1994 [62]. These corrections are required in classical electrostatics as well. The resulting expression is a series of infinite summations for the case of two interacting particles. However, the Ohshima's assumption of the solvent surrounding a particle pair makes the potentials use in a many-bodied dense colloidal system questionable.

## 2.5.2 Solutions to the Poisson-Boltzmann Equation

An exact analytical solution to the full nonlinear Poisson-Boltzmann equation is only possible for specific geometries. There are several common approximations that are applied to reduce the complexity of the expression and broaden the cases where an analytical solution is possible. These approximations will be discussed in detail.

In general, while a colloidal suspension does not have an equal number of positive and negative ions in solution, in many cases the additional ions resulting from the charging of particles are insignificant. Also, while many types of salts may be present in small quantities, it is convenient to treat only the majority salt. This reduces Equation 2.24 to two exponentials. For most systems the ions in solution have the same magnitude of charge (a symmetric salt). With this approximation, the right-hand side of Equation 2.24 reduces to a hyperbolic sine.

$$\nabla^2 \psi = \frac{2 z_i e_c c_i^*}{\varepsilon_0 \varepsilon_r} \sinh\left( \frac{z_i e_c \psi}{kT} \right) \tag{2.25}$$

This nonlinear expression has an analytical solution for very few cases. For dissimilar spheres, the potential fields cannot be described analytically, but instead require a numerical solution. In many colloidal systems, it is possible to gain further insight by making a low surface potential approximation. The Taylor expansion of the hyperbolic sine is given in Equation 2.26.

$$\sinh(x) = x + \frac{x^3}{3!} + \frac{x^5}{5!} + \cdots \tag{2.26}$$

If the argument is much greater than one sixth of the cube of the argument, then terms of higher order than the first term are insignificant. Solving the argument for the surface potential where this occurs gives a limiting value of $\psi$<63.3 mV for z=1. The approximation is generally accepted to be valid for surface potentials less than 25mV. This is known as the Debye-Hückel approximation. The low surface potential requirement in its strictest sense limits the applicability of the linear solution to very few physical systems. However, this approximation can still be used to approximate the physical picture in many other cases as it is a first-order approximation. To illustrate, the hyperbolic sine describes the electrostatic screening in the system. The higher order terms increase the amount of screening for large surface potentials causing the potential to fall off more quickly than would be predicted by the linear equation. In many cases, within a short distance of the surface the potential field has fallen below 25 mV, making the linearized equation a fairly accurate description of the suspension, especially at distances far from the surface of the particle. In this case, a modified surface potential can be applied so that the far field interactions match between the linear and nonlinear cases.

$$\nabla^2 \psi = \left( \frac{2 z_i^{\,2} e_c^{\,2} c_i^*}{\varepsilon_0 \varepsilon_r kT} \right) \psi = \kappa^2 \psi \tag{2.27}$$

The Debye parameter (κ) is introduced into the linearized Poisson-Boltzmann equation as it captures all relevant system variables other than the boundary conditions. In its linearized form, the Poisson-Boltzmann Equation is a common second-order linear differential equation known as the Helmholtz equation, which is appears in models of many physical systems. In considering the fixed charges on the particle surfaces, a charge density term is added to give Equation 2.28.

$$\nabla^2 \psi = \kappa^2 \psi + \frac{\rho_s(x, y, z)}{\varepsilon_0 \varepsilon_r} \tag{2.28}$$

By integrating the Green's function of this equation over an arbitrary surface, the potential field can be obtained for any linear system. A simple numerical form of these integral methods can be applied where a series of point sources are chosen inside of the particle and an equal number of test points are chosen outside or at the surface where the value of the surface potential is known. A set of linear equations is now obtained.

$$\begin{bmatrix} G(x_{t,1} - x_1) & \cdots & G(x_{t,1} - x_n) \\ \vdots & \ddots & \vdots \\ G(x_{t,n} - x_1) & \cdots & G(x_{t,n} - x_n) \end{bmatrix} \begin{bmatrix} A_1 \\ \vdots \\ A_n \end{bmatrix} = \begin{bmatrix} \psi_1 \\ \vdots \\ \psi_n \end{bmatrix} \tag{2.29}$$

These equations are solved for the magnitudes of the point sources ($A_n$). These point sources can now be used to give a computationally inexpensive description of a complex physical system. The error in this method can be reduced by adding more point sources.

For certain shapes of particles, where the chosen coordinate system has single-variable surfaces that correspond to the constant potential plane, a much simpler treatment can be used. These special cases include spheres, cylinders, ellipsoids, and infinite planes. In these cases, one Green's function can be used to describe the potential in the whole region outside of the particle. For a spherical coordinate system, the Green's function for the Helmholtz equation is given by Equation 2.30.

$$G(\boldsymbol{R}-\boldsymbol{R}') = \frac{1}{\varepsilon_0 \varepsilon_r} \frac{\exp(-\kappa|\boldsymbol{R}-\boldsymbol{R}'|)}{|\boldsymbol{R}-\boldsymbol{R}'|} \tag{2.30}$$

By considering an isolated particle with a potential of $\psi_s$ at a radius $R_s$, one point charge at the center of the particle can be used to represent it in order to solve for the potential field of the particle outside of the surface at $R_s$. The surface where the potential is evaluated is generally very close to the particle surface. As is discussed in more detail later, it should actually be the interface between the double layers, which is generally within a few nanometers of the particle surface. When the surface where the potential is evaluated is very close to the particle surface relative to the decay length of the potential ($1/\kappa$), the value of $R_s$ is approximately the particle radius, $a_1$.

$$\psi = a\psi_s \exp(\kappa a) \frac{\exp(-\kappa r)}{r} \tag{2.31}$$

While this assumption will be used for the remainder of this section, in practice it can be relaxed to take into account double layer theory as is described in more detailed later.

This solution satisfies the boundary conditions imposed on the system outside of the particle and must therefore be the only solution by the Uniqueness Theorem [63]. Although this case treats a fixed surface potential, the solution for a constant spherically-symmetric surface charge distribution is identical for an isolated particle. This solution can also be applied to a suspension of many particles with constant charge boundary conditions. The total potential of the system is a simple pair-wise summation of the potentials of single particles in isolation.

Another first-order approximation assumes that the potential field of one particle is not significantly affected by the core of the other particle. In this case, the interaction energy is given by the product of the point charge representation of one particle and the potential field of the other. The magnitude of the effective point charge is given by the following expression.

$$q_{point} = 4\pi\varepsilon_0\varepsilon_r a\psi_s \exp(\kappa a) \tag{2.32}$$

Equation 2.32 is called the linear superposition approximation (LSA) [62, 64, 65].

$$U_{12} = q_1 q_2 \frac{\exp(-\kappa r)}{r} = \frac{\lfloor 4\pi\varepsilon_0\varepsilon_r a_1 \psi_{s,1} \exp(\kappa a_1) \rfloor \lfloor 4\pi\varepsilon_0\varepsilon_r a_2 \psi_{s,2} \exp(\kappa a_2) \rfloor}{4\pi\varepsilon_0\varepsilon_r} \frac{\exp(-\kappa r)}{r}$$

$$= 4\pi\varepsilon_0\varepsilon_r a_1 a_2 \psi_{s,1} \psi_{s,2} \exp(\kappa(a_1 + a_2)) \frac{\exp(-\kappa r)}{r} \tag{2.33}$$

Another form of the LSA model is cast in terms of the surface charges. The surface charge is related to the surface potential by the Poisson equation boundary conditions (Equation 2.35). As the dielectric constant may be different on both sides of the boundary, the form of the Poisson equation must allow for an inhomogeneous permittivity (Equation 2.34).

$$\nabla(\varepsilon \nabla \psi) = -\rho_s(x, y, z) \tag{2.34}$$

$$\left( \varepsilon_{out} \frac{\partial \psi}{\partial n_{out}} - \varepsilon_{in} \frac{\partial \psi}{\partial n_{in}} \right) = \frac{q_{surf}}{4\pi a^2} \tag{2.35}$$

As the potential field inside of an isolated particle is constant, the derivative is zero.

$$\frac{\psi_s (1 + \kappa a)}{a} = -\frac{q_{surf}}{4\pi a^2 \varepsilon_{out}} \tag{2.36}$$

$$q_{surf} = 4\pi\varepsilon_{out} a \psi_s (1 + \kappa a) \tag{2.37}$$

Substituting into the LSA approximation gives the potential in terms of the particle's surface charge.

$$U_{12} \cong \frac{1}{4\pi\varepsilon_0\varepsilon_r} \frac{q_{surf,1}}{(1 + \kappa a_1)} \frac{q_{surf,2}}{(1 + \kappa a_2)} \exp(\kappa(a_1 + a_2)) \frac{\exp(-\kappa r)}{r} \tag{2.38}$$

Equations 2.33 and 2.38 are widely used to describe colloidal behavior and in many situations match quite well with experiment despite the approximations used in their derivation. More complete solutions can be calculated through numerical methods.

The interaction potential in Equation 2.33 or 2.38 is called a Yukawa-type potential, or a shielded-electrostatic potential. It is commonly used to describe colloidal interactions [66-81]. As the Debye parameter goes to zero with a reduction in shielding ions, classical electrostatics are recovered. While many times unnecessary, Equation 2.33 can be approximated as Equation 2.39 in systems with large ionic strengths.

$$U_{12} = 4\pi\varepsilon_0\varepsilon_r a_1 a_2 \psi_{s,1} \psi_{s,2} \exp(\kappa(a_1 + a_2)) \exp(-\kappa r) \tag{2.39}$$

For ion-penetrable spheres, Equation 2.33 is slightly modified to account for the fact that the potential field inside the sphere is no longer constant. This field can be calculated by solving Equation 2.27 inside the sphere under the boundary conditions that the derivative is zero at the center of the sphere and the value matches the surface potential at the surface of the sphere. The solution is given by a summation of an exponentially increasing and an exponentially decreasing Yukawa potential.

$$\psi_{inside} = a\psi_s \frac{\exp(-\kappa r) - \exp(-\kappa r)}{\left(\exp(-\kappa a) - \exp(\kappa a)\right) r} \tag{2.40}$$

Outside of the particle, the potential is still expressed by Equation 2.33. The relation between surface potential and surface charge is found using the potential fields inside and outside of the particle, as in Equation 2.35.

$$q_{surf} = \frac{8\pi\varepsilon_{out} a^2 \kappa}{1 - \exp(-2\kappa a)} \psi_s \tag{2.41}$$

Another important case of the linearized Poisson-Boltzmann equation is that of a flat plate. In this case, the Green's function is given by Equation 2.42.

$$G(\mathbf{x} - \mathbf{x}') = \frac{1}{4\pi\varepsilon_0\varepsilon_r} \exp\left(-\kappa\left|\mathbf{x} - \mathbf{x}'\right|\right) \tag{2.42}$$

By setting the boundary condition of the plate's surface potential at x=0, the potential field of the flat plate is obtained.

$$\psi(x) = \psi_s \exp(-\kappa x) \tag{2.43}$$

Assuming the particle does not significantly alter the potential field of the plate, the interaction of a spherical particle with that plate can be obtained by multiplying by the charge on the particle, resulting in Equation 2.44.

$$U_{12}(x) = 4\pi\varepsilon_0\varepsilon_r a_{particle} \psi_{s,particle} \psi_{s,wall} \exp(\kappa a_{particle}) \exp(-\kappa x) \tag{2.44}$$

An identical solution could have been obtained by treating one sphere as having an infinite radius in the sphere-sphere interaction equation (Equation 2.33).

### 2.5.3 HHF Theory and Other Potentials

For dissimilar particle interactions, another treatment introduced by Hogg, Healy, and Feurstenau (HHF) (Equation 2.43) is widely used in the literature [82]. HHF theory was an extension of the work on dissimilar colloidal interactions by Derjaguin [83], and Devereux and de Bruyn [84]. It is obtained by considering two dissimilarly charged plates with constant surface potentials. The result for the constant potential surfaces is then treated with the Derjaguin approximation [85] to give the interaction of two dissimilar spheres.

$$U_{HHF} = \frac{\varepsilon_r \varepsilon_0}{4} \frac{a_1 a_2}{a_1 + a_2} \left[ 2\psi_{S1}\psi_{S2} \ln\left\{ \frac{1 + e^{-\kappa H_0}}{1 - e^{-\kappa H_0}} \right\} + \left\{ \psi_{S1}^2 + \psi_{S2}^2 \right\} \ln\left\{ 1 - e^{-2\kappa H_0} \right\} \right] \qquad (2.45)$$

While almost all heterocoagulation studies in the literature use HHF theory to describe the results, it should not be universally applied. Hogg, et al., cite work from Verway and Overbeek [86] that limit the applicability of the Derjaguin approximation to values of κ*a*>10, which corresponds to a high ionic strength. As would be expected for a constant potential assumption, HHF theory diverges in energy at particle contact for spheres with dissimilar signs of charge. The redispersal of a heterocoagulated system would be impossible under this model. While a cutoff radius could be applied as was done above for Hamaker theory, such an approximation has not been pursued for HHF theory.

A similar formulation to that of Hogg, Healy, and Feurstenau was introduced by Weise and Healy (Equation 2.46) for the treatment of a constant charge distribution boundary condition [87]. While this approximation is not as widely used, it does overcome one limitation of the HHF model. Instead of diverging to an infinite attraction at contact, the Weise-Healy model diverges to an infinite repulsive energy at contact for spheres with dissimilar signs of charge. The potential has a minimum at a finite separation distance from the surface. The theory of Weise and Healy is also limited to the treatment of solution with high ionic strength.

$$U_{WH} = \frac{\varepsilon_r \varepsilon_0}{4} \frac{a_1 a_2}{a_1 + a_2} \left[ 2\psi_{S1}\psi_{S2} \ln\left\{ \frac{1 + e^{-\kappa H_0}}{1 - e^{-\kappa H_0}} \right\} - \left\{ \psi_{S1}^2 + \psi_{S2}^2 \right\} \ln\left\{ 1 - e^{-2\kappa H_0} \right\} \right] \qquad (2.46)$$

While HHF theory is widely used due to its simple analytical form, more exact expressions of the interaction of dissimilar spheres continue to be sought out in the literature. An overview of the progress in heterocoagulation theory was published by Islam [88]. One formulation, introduced by Ohshima, overcomes the Derjaguin approximation by utilizing an expansion of the particle potentials in terms of Bessel function and Legendre polynomials [62, 64, 65]. This formulation results in an infinite summation of what are termed “image potentials”, in analogy to the image charge construct that is used to study constant potential surfaces in classical electrostatics. While the Ohshima formulation may give the exact pair interaction for two isolated particles, it's applicability as a pair potential in studying dense colloidal systems has not been examined. Oshima notes that the LSA potential derived above is the first term of his expansion and is completely accurately for ion-penetrable spheres (where the inside of the particle appears similar in dielectric constant and screening to the solution outside of the sphere). Any example of an ion-penetrable sphere would be a biological cell where the dominant salt ions in the solution can flow freely through the cell membrane

## 2.5.4 Double Layer Theory and the Zeta Potential

The Gouy-Chapman [58, 59]model assumes infinitesimally small ions around a smooth, non-absorbing surface. In order to correct for these approximations, a double layer model has been implemented. The two layers consist of a diffuse layer, termed the Gouy-Chapman layer, and an inner layer termed the compact double layer, which was first proposed by Stern and is called the Stern layer [89].

In the compact double layer, a salt ion of a finite size can only approach a particle surface to within its own radius. This creates a region of charge depletion from the particle surface to the center of the salt ion, assuming that the ion's charge is on average localized at its center. Note that due to the finite size of the solvent molecules, this region is also depleted of solvent molecules and so does not have the macroscopic dielectric constant of the solvent. The Poisson equation is used to solve for the potential in this region resulting in a capacitor-like behavior where the potential field falls off linearly. Charge adsorbed in the compact double layer region is treated in a similar manner. The solution for this region is again a capacitor-like behavior. The edge of the compact double layer denotes the separation between the material that moves with the particle and that which moves freely around the particle. The diffuse double layer is the region beyond the compact layer, where ions are free to move and thus the Poisson-Boltzmann equation describes the interactions.

The zeta potential is a name given to the apparent potential of a particle, which is determined by all of the charge that moves with the particle in addition to the charge on the particle surface. The zeta potential is define as the electrostatic potential at the surface between the compact and diffuse layers. A more detailed explanation of zeta potential theory is given in Hiemenz and Rajagopalan [28].

The zeta potential can be determined indirectly through many approaches that measure the colloidal particles mobility. Electrophoresis is one method for measuring the zeta potential. When an electric field is applied to a particle, there is a resulting force that moves the particle proportional to its apparent electrical potential. Using a force balance, the apparent potential ($\zeta$) can then be determined by measuring the terminal velocity of the particle, which is proportional to the electrophoretic mobility ($\mu$) and the applied electric field.

$$F = 0 = -\beta v + Eq \tag{2.47}$$

$$v = \frac{Eq}{\beta} = E\mu \tag{2.48}$$

The mobility is related to the zeta potential through a variety of models. The two most common, due to their simplicity, are the Hückel model [90] (for $\kappa a$<<1) and the Smoluchowski model [91] (for $\kappa a$>>1).

In the Hückel model, the charge on the particle is assumed to be identical to that which would be present via classical electrostatic. It is therefore not κ dependant.

$$v = \frac{Eq}{\beta} = \frac{E}{6\pi a\eta}\left(4\pi\varepsilon_0\varepsilon_r\zeta a\right) = \frac{2E\varepsilon_0\varepsilon_r\zeta}{3\eta} \tag{2.49}$$

$$\zeta = \frac{3\eta v}{2E\varepsilon_0\varepsilon_r} \tag{2.50}$$

The Smoluchowski equation applies at the opposite extreme. It treats the particle as a flat plate and considers the force on the solution. The viscous force on a volume element with surface area *A* of the suspension above the particle is balanced against the electrostatic force on the charges in the diffuse double layer in that volume element. The viscous term is obtained from the Stokes equation and the electrostatic term is derived from the Poisson equation.

$$F = \eta A \frac{d^2 v}{dx^2} dx + EA\varepsilon \frac{d^2\psi}{dx^2} dx \tag{2.51}$$

Assuming only the electrical potential and the velocity vary, the first integration gives a simple expression

$$\eta \frac{dv}{dx} = -E\varepsilon \frac{d\psi}{dx} + C \,. \tag{2.52}$$

The zeta potential can be found from this equation by applying the appropriate boundary conditions. The velocity must be zero at the interface between the two portions of the double layer, the potential must be zero at an infinite distance and $\zeta$ at the interface, and both derivates must be zero at an infinite distance. The resulting solution gives a simple expression for the zeta potential

$$\zeta = \frac{\eta v}{E\varepsilon_0 \varepsilon_r} \,. \tag{2.53}$$

Comparing the zeta potentials from the two cases, it can be seen that they differ by only a slight difference in the proportionality constant despite the vast differences in approximations. The proportionality constant in the intermediate regime was treated by Henry [92]. The treatment of the intermediate region is substantially more complex, but results in the Hückel and Smoluchowski equations in its limit. Despite the added complexity, the Henry equation is still limited to only applying at small zeta potential values. A nonlinear treatment has been presented that relates the zeta potential to the mobility at all values of $\kappa a$ [93]. The resulting proportionality constant is no longer a smoothly varying, monotonic function, but is instead dependant on the surface potential present. This formulation should generally be used for values of $\kappa a$ approximately equal to one.

## 2.6 Consideration of Multiple Forces

The theory of Derjaguin, Landau, [94] Verway, and Overbeek [86] (DLVO) was the first to combine the van der Waals contribution and the electrostatic contribution in an attempt to understand colloidal behavior. The resulting theory has been instrumental in the modern understanding of colloidal interactions. For a single component colloidal system, an energy barrier to the deep van der Waals minimum at contact results from the electrostatic interactions. If sufficient screening is present to lower that barrier below a few kT, rapid homocoagulation will occur.

Similarly, introduction of further forces, such as steric or solvation forces, can reduce or effectively remove the deep van der Waals minimum. For example, steric forces introduced through surfactant addition can be used to stabilize otherwise rapidly heterocoagulating systems. Furthermore, external energy can be added through such means as ultrasonication, vortexing, or shearing. This energy can, in many cases, restore coagulated particles to a suspended state if the Hamaker minimum is not too deep.

DLVO theory has been disputed recently in efforts to explain long-range attractive forces seen experimentally between like-charged particles [95]. However, these interactions may be accounted for under Poisson-Boltzmann theory by considering the ions that enter solution during particle charging. One can imagine that these ions, when in a significant number relative to other ions from salts in the system, could act as a charge-glue binding two particles together. As the ion distribution is effectively a probability distribution around the particles, in the case of no salt ions, this distribution should behave similarly to that between two hydrogen atoms, where an electron probability distribution with a peak between the two nuclei is the most favorable state. While this study is beyond the scope of this thesis, future work will be conducted in an effort to prove this hypothesis. The interaction of two colloidal particles will be evaluated under the non-linear Poisson-Boltzmann equation, where the number of ions present range from being predominately counterions of surface charges (expected to be attractive) to salt ions in solution (expected to be repulsive, matching Poisson-Boltzmann theory).

# Chapter 3: Colloidal Forces in Ionic Colloidal Crystals

In an ionic colloidal crystal system, electrostatic forces are essential to the system stability. The colloidal system should be engineered to minimize the impact of other forces. Also, in modeling ICC behavior, special attention must be paid to the boundary conditions and approximations used in developing the electrostatic model. .

## 3.1 Competing Colloidal Forces

Electrostatic forces are among the strongest and longest range forces in colloidal interactions. In the far field, these forces typically dominate colloidal behavior. However, when particles are near one another, it is possible for other forces, such as Hamaker forces, to become more significant. In ICCs, these forces should be mitigated in order to prevent the particle binding energy from becoming significantly larger than that predicted by electrostatic interactions alone. If binding energy is altered by short range forces, interactions with particles beyond the nearest neighbor become far less significant to the overall system energy. Because these longer range electrostatic interactions are important for ICC ordering, any decrease in their contribution will decrease the stability of ICCs.

Because Hamaker forces tend to be the strongest of the short range interactions, these forces in particular should be minimized, made repulsive, or screened in order to stabilize ICCs. As discussed in Chapter 2, Hamaker forces can be either minimized or made repulsive through careful materials selection and consideration of their dielectric response functions. The materials available for ICCs are restricted to commercially available monodisperse particles, which are mainly composed of silica or polystyrene. Figure 3.1 shows the dielectric response functions for polystyrene and silica along with several common solvents. In order for the Hamaker force to be repulsive between these two materials, the dielectric response function of the solvent must lie in between their dielectric response functions. Because the two materials have very similar dielectric response functions, very few solvents have one that is intermediate. Furthermore, the solvent in the ICC system must be polar in order to allow a surface charge to develop on the colloids. With this added constraint, no solvent choices remain that would create a repulsive interaction. The chemical similarity between polystyrene and many solvents reduces the magnitude of the Hamaker constants in these systems. The interaction of polystyrene and silica in water was calculated to be 6.7 zJ from available literature data [96-98] using Equation 2.4. Ethanol data [99] was used to approximate the interaction in 2-propanol to be 7.3 zJ. The dielectric response functions for the four materials are shown in Figure 3.1.

Although the Hamaker interaction between silica and polystyrene is small, it can be further reduced through the use of other short range forces, such as steric forces. The strength of Hamaker interactions falls off rapidly with particle separation, allowing other short range forces to screen these interactions. Steric forces can be introduced through surfactant addition to prevent particles from approaching close enough for Hamaker interactions to become significant.

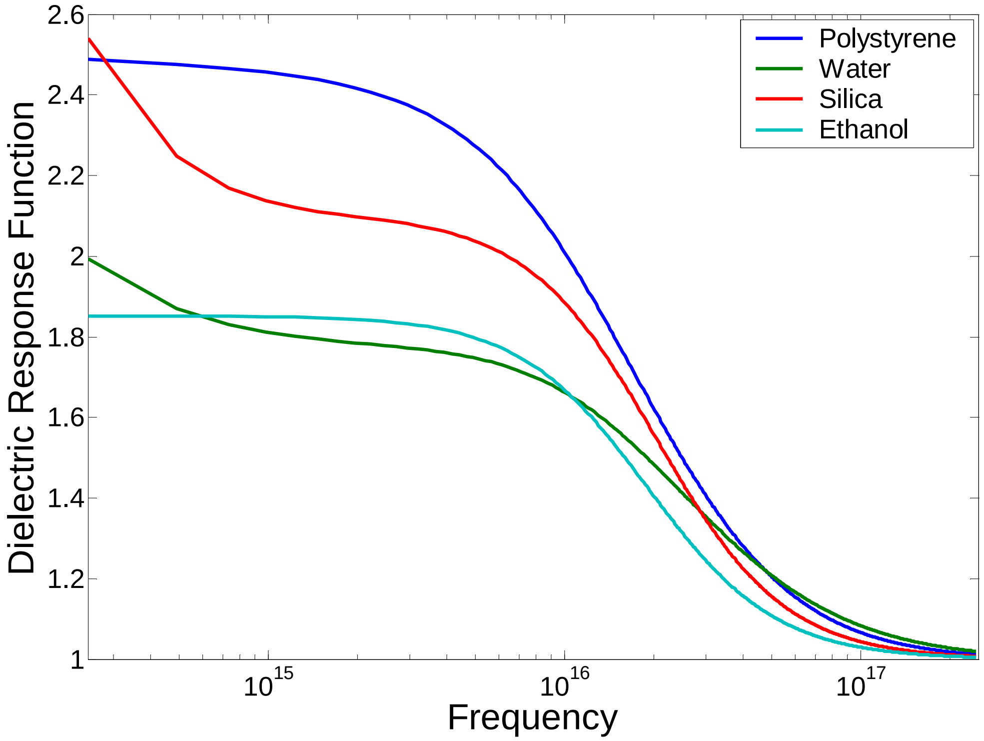

Figure 3.1: The dielectric response functions are shown for four candidate materials. The similarity of the polystyrene and silica data make it difficult to find a solvent that falls between them. Ethanol (used to approximate 2-propanol) and water are shown for comparison.

## 3.2 Appropriate Boundary Conditions for ICCs

Ionic colloidal crystals require the close approach of dissimilar colloids. As was discussed in Section 2.5.1, constant surface potential boundary conditions result in an infinite interaction energy for dissimilar particles in contact. Furthermore, colloids that normally (i.e. in isolation) have uncharged surface sites will be driven towards surface charge saturation when in close vicinity with a large number of dissimilarly charged particles. Therefore, once equilibrated, the particles in the system will behave with a constant surface charge distribution boundary condition, even if in isolation the particles do not have a saturated surface charge.

As discussed later, a short range repulsion may result from constant charge boundary conditions, as illustrated by the Ohshima or Wiese-Healy potentials. If this repulsion exists in a dense colloidal suspension and not just in pair interactions, it may be used to minimize the effect of short range forces without surfactant additions. For reasons discussed in Chapter 4, high $\kappa a$ values are undesirable for ICC formation, and therefore the Wiese-Healy potential would be inappropriate for the study of ICC formation. Alternatively, the Ohshima potential remains a strong candidate for the study of ICCs since it is valid for even low values of $\kappa a$.

However, for a preliminary study on ICC formation, the LSA potential is a more appropriate choice. While this model does not consider the effect of the dielectric medium in the center of the spheres, it is the only form that can be added pair-wise without the violation of any of the assumptions taken during its formulation. A further discussion of the choice of the LSA model and its implications are found in Chapter 8, which is devoted to comparing the actual energy of an ICC calculated numerically with that derived from potential models. While the LSA results will not be exact, they are still useful in identifying property trends in ICCs.

# Chapter 4: Ionic Colloidal Crystals: A First Order Approach

Colloidal behavior is widely modeled to first-order with the Yukawa-type potential (Equation 2.33). In this formulation, it is assumed that one sphere does not affect the potential field resulting from a second sphere. This approximation is exact in the case of spheres with dielectric properties and internal ion concentrations identical to that of the solution. Such colloids have been termed ion-penetrable spheres or "soft" spheres by Ohshima [62, 64, 65]. However, even for the case of non-ion-penetrable spheres, the analytical simplicity of the Yukawa potential formulation allows a first-order determination of where ionic colloidal crystallization should be possible in terms of two dimensionless parameters. While this description is not exact, it gives guidelines for tailoring experiments. The behavior of attractive-Yukawa fluids has been modeled [100-102], however, to our knowledge, either single component systems were treated with attractive Yukawa interactions or binary systems were examined without looking at the crystallization of these liquids. A more complete formulation can be applied to further narrow the experimental parameter space once specific potential systems have been identified.

## 4.1 Madelung Summation

In studying classical ionic materials, a preliminary understanding of the stability conditions for crystallization is gained by comparing the electrostatic energy of a crystal to that of an isolated dipole. The electrostatic interaction between each unique lattice site within the unit cell and all of the other atoms in the crystal is calculated and summed. This summation, called the Madelung summation, usually consists of terms corresponding to each set of nearest neighbors.

$$U_0 = \sum_j \left( N_j \frac{q_0 q_j}{4\pi\varepsilon_0\varepsilon_r r_j} \right) \tag{4.1}$$

The crystal energy is then normalized with respect to one nearest-neighbor interaction. This formulation allows the energies of a variety of different crystal structures to be compared in order to determine which is the most energetically stable.

To further illustrate this method, the calculation of the Madelung summation for the rocksalt structure is shown in Equations 4.2 and 4.3. In this structure, the anions and cations are each arranged in two interwoven close-packed lattices. The number of nearest-neighbors in each set and their corresponding distance from the central atom can be calculated to give the crystal energy as shown in Equation 4.2.

$$U_0 = -6\frac{e_c^2}{4\pi\varepsilon_0\varepsilon_r(a_1+a_2)} + 12\frac{e_c^2}{4\pi\varepsilon_0\varepsilon_r\sqrt{2}(a_1+a_2)} - 8\frac{e_c^2}{4\pi\varepsilon_0\varepsilon_r\sqrt{3}(a_1+a_2)} + \cdots \tag{4.2}$$

Normalizing to the isolated dipole energy, the Madelung constant can be obtained as shown in Equation 4.3.

$$M_{SUM} = 6 - 12\frac{1}{\sqrt{2}} + 8\frac{1}{\sqrt{3}} - 6\frac{1}{2} + \cdots \tag{4.3}$$

This summation, as it stands, converges poorly. Figure 4.1 illustrates the lack of convergence of the Madelung summation with each additional nearest-neighbor term.

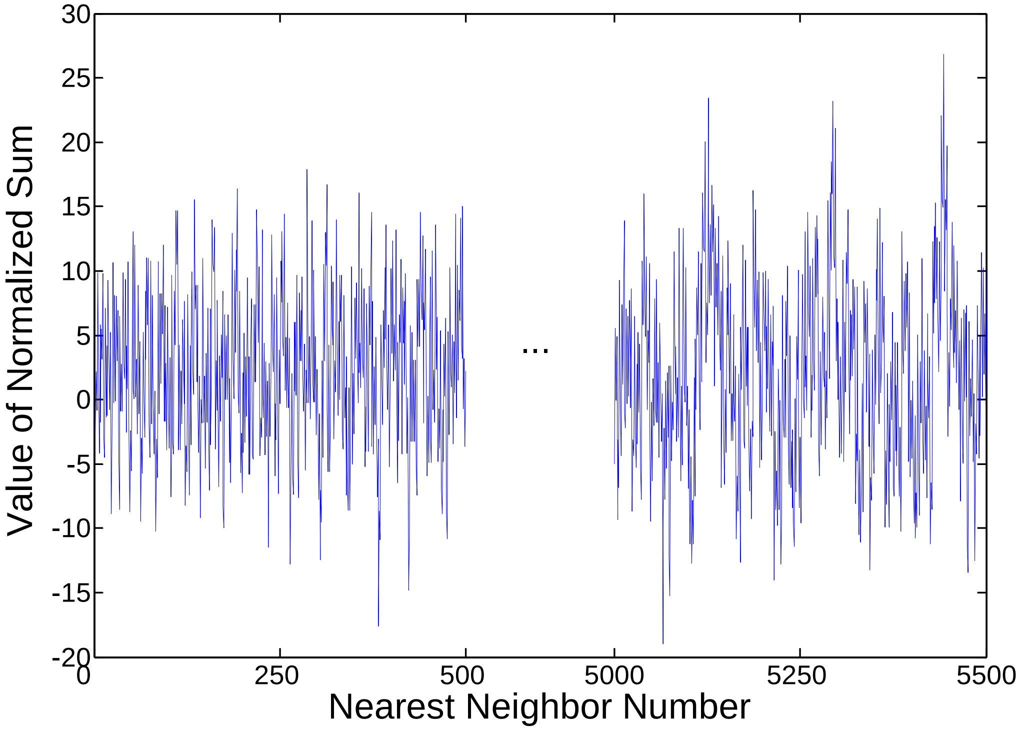

Figure 4.1: The Madelung sum in traditional ionic materials converges poorly. Illustrated above, the summation across the first 500 terms and the summation across the 500 terms starting at the 5000th nearest neighbor are both oscillating similarly with no sign of convergence.

For an ionic colloidal crystal, we perform a similar treatment using the Yukawa type potential. Equation 4.4 gives the resulting summation.

$$U_0 = \sum_j \left( N_j \frac{Q_0 Q_j \exp\left(-\kappa r_j\right)}{r_j} \right) \tag{4.4}$$

Here the *Q* term is not simply an amount of charge, but the representative point charge that matches the isolated particle's surface potential. For clarity, this representative charge is presented again in Equation 4.5.

$$Q_i = 4\pi\varepsilon_0\varepsilon_r a_i \psi_i \exp\left(\kappa a_i\right) \tag{4.5}$$

The Madelung summation for one site of the ICC rocksalt structure can now be found.

$$U_1 = \frac{1}{4\pi\varepsilon_0\varepsilon_r}\left(6\frac{Q_1Q_2\exp\left(-\kappa\left[a_1+a_2\right]\right)}{\left(a_1+a_2\right)}+12\frac{Q_1Q_1\exp\left(-\kappa\sqrt{2}\left[a_1+a_2\right]\right)}{\sqrt{2}\left(a_1+a_2\right)}+\cdots\right) \tag{4.6}$$

This summation can be normalized with regard to the isolated bond strength to give the Madelung sum for a rocksalt ICC.

$$M_{SUM} = 6+12\frac{Q_1}{Q_2}\frac{\exp\left(-\kappa\left[\sqrt{2}-1\right]\left[a_1+a_2\right]\right)}{\sqrt{2}}+8\frac{\exp\left(-\kappa\left[\sqrt{3}-1\right]\left[a_1+a_2\right]\right)}{\sqrt{3}}\cdots \tag{4.7}$$

## 4.1.1 Two Dimensionless Parameters

The resulting Madelung sum is no longer a constant, but is dependant on two dimensionless parameters. The first is a relative screening length that compares the exponential decay of the Yukawa potential to the size of the colloidal particle. The second is the ratio of representative charges. This parameter results due to the removal of the constraint that the anion and cation sites for the ICC rocksalt structure contain the same charge (i.e. the lattice sites can be asymmetric). These two dimensionless parameters are shown below.

$$\Lambda = \kappa\left(a_1+a_2\right) \tag{4.8}$$

$$Q = -\frac{a_1\psi_1\exp\left(\kappa a_1\right)}{a_2\psi_2\exp\left(\kappa a_2\right)} \tag{4.9}$$

Here *Q* is arbitrarily defined to be the ratio of the point charge representation of the larger particle to that of the smaller particle. This choice assures that *Q* is always increasing with Λ.

With the shielded electrostatic potential, the Madelung summation above converges rapidly for even moderate values of Λ. As can be seen in Figure 4.2, for a Λ value of 1, the summation is fully converged within a few hundred nearest neighbors. This value of Λ corresponds to two ~350 nm particles in ultrahigh purity water.

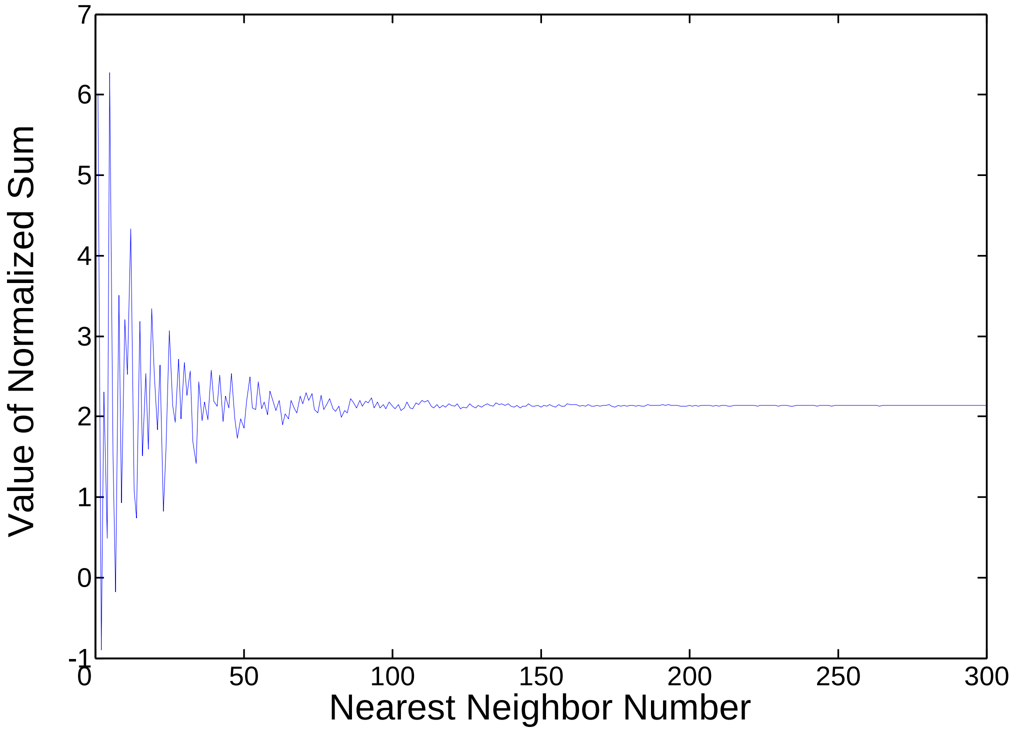

Figure 4.2: In an ionic colloidal crystal, even a small amount of screening leads to a rapidly converged summation. Shown here is the summation for ICC rocksalt with a value of Λ equal to 1.

When there is charge asymmetry, for example having a charge ratio greater than one in a rocksalt structure, the anion and cation sites are no longer identical in energy. Due to this, the resultant Madelung summation must be the average of all nonidentical lattice sites. For the rocksalt structure, this gives Equation 4.10.

$$M_{SUM} = 6 - 12\left(\frac{1}{2}\right)\left(Q + \frac{1}{Q}\right)\frac{\exp\left(\Lambda\left[1-\sqrt{2}\right]\right)}{\sqrt{2}} + 8\frac{\exp\left(\Lambda\left[1-\sqrt{3}\right]\right)}{\sqrt{3}}\cdots \tag{4.10}$$

This summation can now be taken over the entire parameter space of $Q$ and Λ to give the stability region of the crystal relative to isolated dipoles.

For crystal structures with an unequal number of each atom, such as the fluorite structure, the convention of normalizing to the single dipole strength is chosen. While the dipole is not charge neutral for anything except AB structures, a consistent normalization allows an accurate comparison of the relative energies of each structure.

### 4.1.2 Madelung Sums for Various Structures

Figures 4.3 through 4.8 show the resultant Madelung summation versus these dimensionless parameters for a variety of crystal structures. Note that at large Λ values (large screening ratios), the Madelung sum limits to the number of nearest neighbors as very little next nearest neighbor repulsion contributes to the sum. As all repulsion is screened out, charge asymmetry has a small affect on crystalline stability in this region. At smaller screening ratios, the Madelung summation limits to the classical value, but asymmetry of charge comes with a high energy cost, causing a large region of the phase space to be unstable. As is mentioned previously, the Madelung summations for AB structures are symmetric about a charge ratio of one because structures with reciprocal charge ratio values are identical except the site containing the higher charge particle switches.

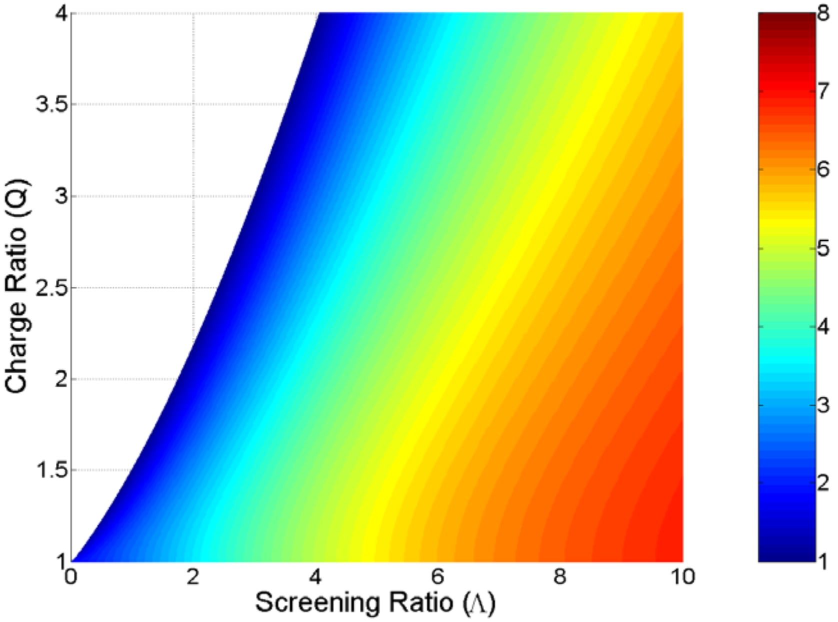

Figure 4.3: The Madelung summation is plotted for an ICC cesium chloride structure. Note the Madelung sum is limiting toward the number of nearest neighbors for the structure (8 neighbors) as Λ becomes large. This limit makes the cesium chloride structure the most stable of the 1:1 structures for a large portion of the Q-Λ parameter space. Lower nearest-neighbor structures become more stable at low screening ratios where Q deviates from 1 because these structures allow a greater separation of the higher charged species. For all 1:1 structures, the Madelung sum is reciprocally symmetric about Q=1. Regions where the Madelung summation is less than one are shown in white.

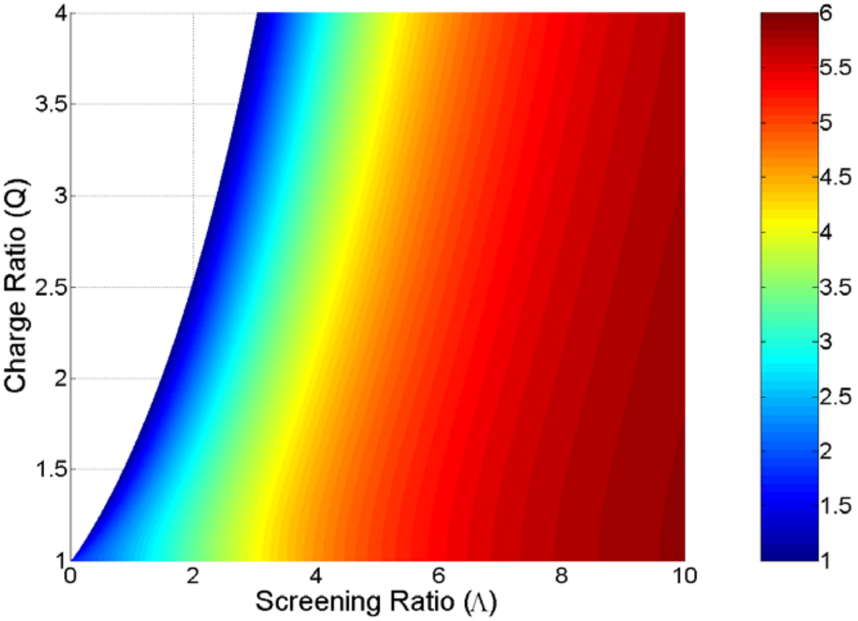

Figure 4.4: The Madelung summation for an ICC rocksalt structure is shown. The Madelung sum again limits to the number of nearest neighbors, which is only 6 for this structure.

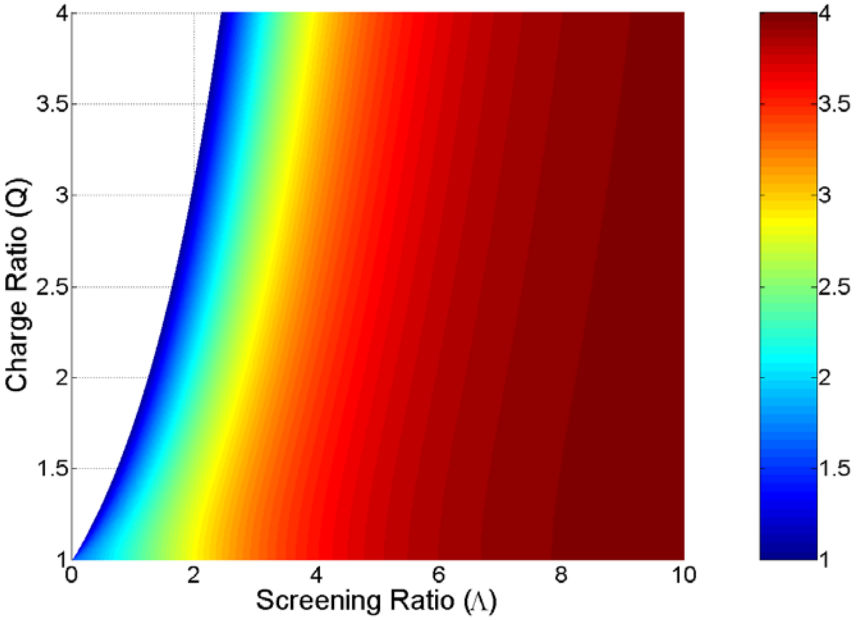

Figure 4.5: The Madelung summation for an ICC zincblende structure is plotted.

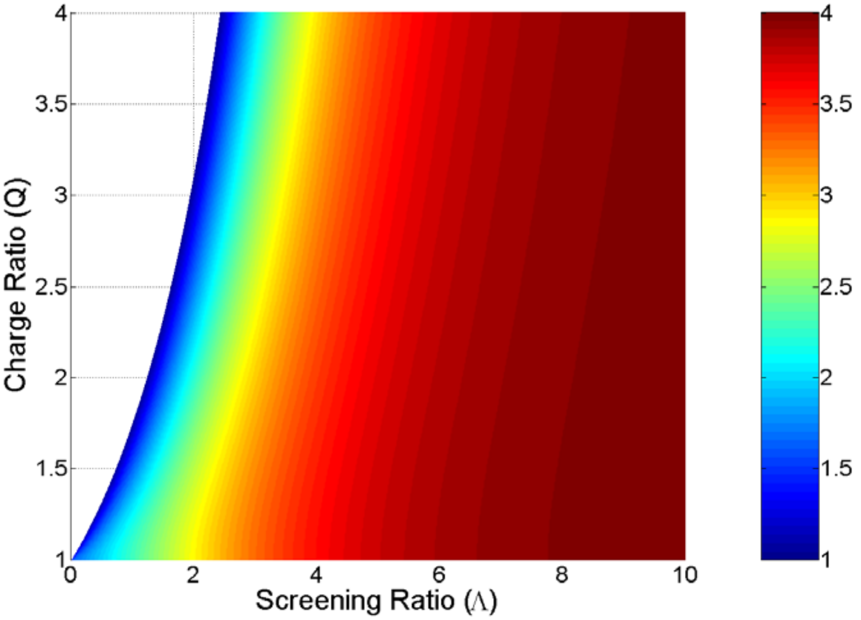

Figure 4.6: The Madelung summation for an ICC wurtzite structure is shown. Note the similarity to the zincblende summation. The wurtzite structure is slightly more stable than zincblende across the entire phase space. This structure has the greatest tolerance for charge asymmetry, but due to the low number of nearest neighbors, other structures dominate most of the Q-Λ parameter space.

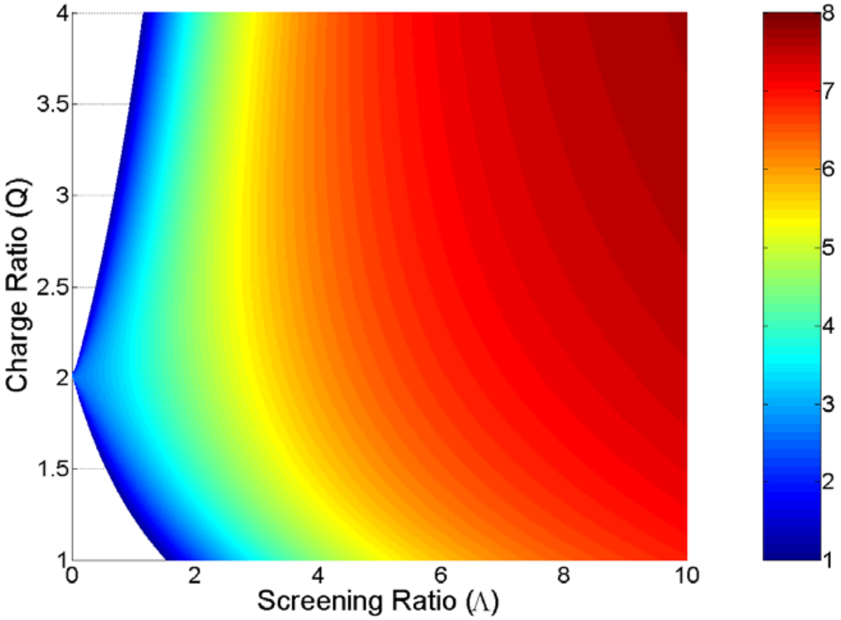

Figure 4.7: The Madelung summation is plotted for an ICC fluorite structure. While this structure is not reciprocally symmetric about Q=1, an analogous structure with the larger atoms in the minority ($A_2B$ vs. $AB_2$) is possible having the same Madelung constant except at *Q*'=1/*Q*.

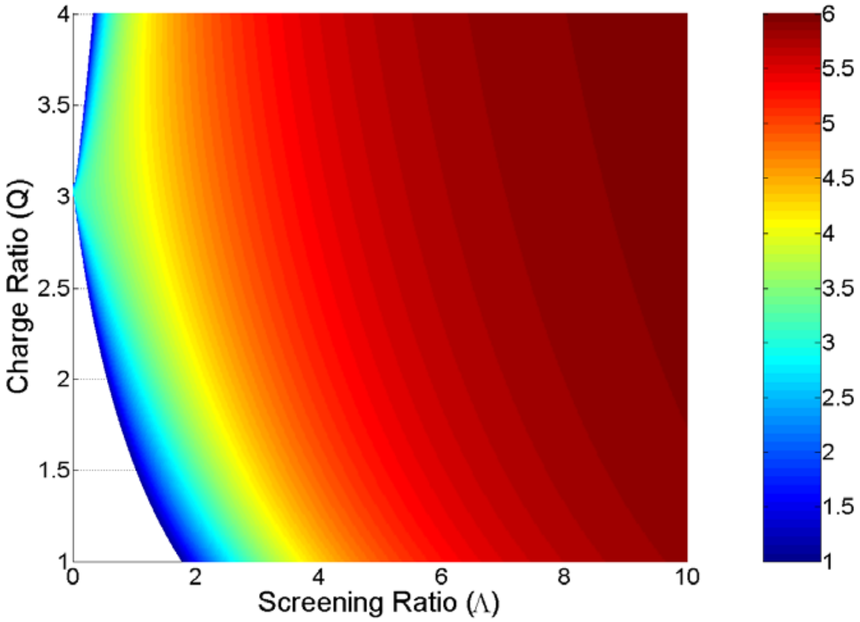

Figure 4.8: The Madelung summation for an ICC Ruthenium Oxide structure is plotted.

### 4.1.3 Impact of Ionic Strength on Crystallization

While it would appear that the ideal target region would be high ionic strengths as ICCs are stable across a wider parameter space in that regime, the electrostatic potential there is very short ranged. Heterocoagulation in this regime would be analogous to previous work done on utilizing complementary DNA strands that are attached to dissimilar particles to tailor attractive interactions between them [103]. In that study, the strength of the interaction could be tuned, allowing the formation of either colloidal glass or liquid structures, but ordering was not observed. This behavior is explained by the interaction force between particles.

Considering two particles, the maximum strength of the interaction between them is independent of the ionic strength and is given by Equation 4.11.

$$U_{\max} = 4\pi\varepsilon_0\varepsilon_r\psi_1\psi_2\frac{a_1a_2}{a_1+a_2} \tag{4.11}$$

However, the force required to move the two particles apart while in contact increases with ionic strength, as given in Equation 4.12.

$$F_{contact} = 4\pi\varepsilon_0\varepsilon_r\psi_1\psi_2 \frac{a_1 a_2}{a_1 + a_2}\left(\kappa + \frac{1}{a_1 + a_2}\right) \tag{4.12}$$

The contact force, or the slope of the potential well in which the particles sit, determines the mobility of the particles after a collision. If the potentials reach a long distance relative to the particle size, a small perturbation in the particle position does not cause a large change in the energy. However, a small perturbation in position at high ionic strengths causes a much larger change in the internal energy due to the higher slope of the potential. Thus, in order for there to be substantial mobility in these systems, a large temperature is required. The particle will not be able to move until the thermal energy is comparable to the entire well depth. At this point, the thermal energy would be very similar to that required for melting or even boiling. Stated another way, this lack of mobility causes the entropy of a high ionic strength system to be nearly zero until the thermal energy becomes comparable to the melting point. Because of this, a dense amorphous heterocoagulate will not have sufficient mobility to rearrange into a crystal until the temperature is very close to the melting point (i.e. the glass transition temperature is very close to the melting point). On the other hand, a lower ionic strength would result in a lower glass transition temperature and therefore a larger window in which crystallization could occur.

This analysis explains the experimental observations in traditional heterocoagulation at high ionic strengths and in DNA mediated particle interactions. In both cases, the potential interactions are very short range. For any movement to occur, the kinetic energy in the system needs to be similar to the entire interaction energy. Therefore, the energy needed for a small amount of rearrangement is similar to that required for a fluid-like state. The result is a rapid transition between a glass and a liquid with an almost non-existent range in which crystallization can occur.

## 4.2 ICC Phase Diagram: Comparison of Phases

Utilizing the formulation presented above, the Madelung summations of different crystal structures can be compared. The appropriate comparison depends on the number ratio of the particles present in the solution. Three simple cases will first be addressed in detail: vast excesses of either particle and a 1:1 mixture of both particles. For this analysis, the larger particle is defined as the A particle, and the smaller particle as the B particle.

When there is a vast excess of smaller particles, the most stable structure is simply the one that places the larger particles in the most energetically favorable environment, regardless of how many smaller particles surround each larger particle. This is because there is no energy associated with single small particles separated from the crystal in solution. In order to compare the relative stabilities of different structures for this case, the Madelung sum for each structure should be divided by the number of larger particles in the stoichiometric unit of that structure. This normalized Madelung summation corresponds to the energy gained per larger atom added. For example, in the case of the $A_2B$ structure, the Madelung sum must be divided by two, which means that the addition of a single A atom only contributes half the Madelung energy because only half a stoichiometric unit can be made. The highest normalized Madelung summation for all the structures is the lowest energy configuration for the system. Figure 4.9 illustrates the lowest energy structure over the entire phase space under this constraint. Note that for $Q$ values less than 1, the 1:1 structures are stable across a much broader range than for $Q$ values greater than 1.

A parallel case occurs when the there is a vast excess of the larger particle and a limitation on the number of smaller particles. In this case, the Madelung summation for each structure is divided by the number of smaller particles in the stoichiometric unit. The resulting stability fields are shown in Figure 4.10.

When the number of both particles is constrained, the problem becomes much more complex, with the possibility of the formation of multiple phases within the same system. However, another simple case exists. When the number ratio of particles is 1:1, the presence of a 1:2 number ratio phase would require some particles to remain unused. This will only occur if the creation of the 1:2 phase (either $AB_2$ or $A_2B$) has a higher normalized Madelung summation (in this case, divided by two for either structure) than the 1:1 phase. Specifically, the creation of a 1:2 phase requires that it be twice as favorable as two 1:1 phases because only half as many stiochiometric units can be made if a 1:2 phase is created. The resulting phase diagram is shown in Figure 4.11. Note that in this case, the 1:1 phase fields are stable across the broadest regime, as would be expected since no particles would be left unused in those phase regions. Also note that the resulting diagram is identical to the *Q* greater than one region of the A-limited phase diagram and the *Q* less than one region of the B-limited diagram.

These phase diagrams will also be altered by Pauling's rules [104]. In the above phase diagram, all possible types of site filling were allowed. However, by Pauling's rules, the minimum particle size that can fill certain types of sites is limited to the smallest particle that can completely fill the site without allowing the other particles to touch. Table 4.1 shows the site filling restrictions given by Pauling's rules. If these restrictions are applied in ionic colloidal crystals, the phase regions where various structures are stable can be broadened by tailoring the size ratio of the particles. For example, wurtzite can be stabilized across most of the phase fields by making the size ratio below 0.414. This is because under Pauling's rules, a larger atom can occupy a site, however a smaller atom cannot. For example, with a size ratio of 1:1, the zincblende structure is possible. However, with a size ratio of 0.5, the cesium chloride structure cannot form.

Table 4.1: The site filling criteria are shown as given by Pauling's rules. A larger atom can occupy a site generally filled by a smaller atom, but the opposite cannot occur. For example, a system with a size ratio near 1:1 can form all structures, while one with a size ratio of 0.5 cannot form any structures with cubic site filling.

| **Size Ratio Range Ideal (Possible)** | **Site Filling** | **AB Structure Type** |
|---|---|---|
| 1-0.7 (1-0.7) | Cubic | Cesium Chloride |
| 0.414-0.7 (1-0.414) | Octahedral | Rocksalt |
| 0.2-0.414 (1-0.2) | Tetrahedral | Zincblende, Wurtzite |

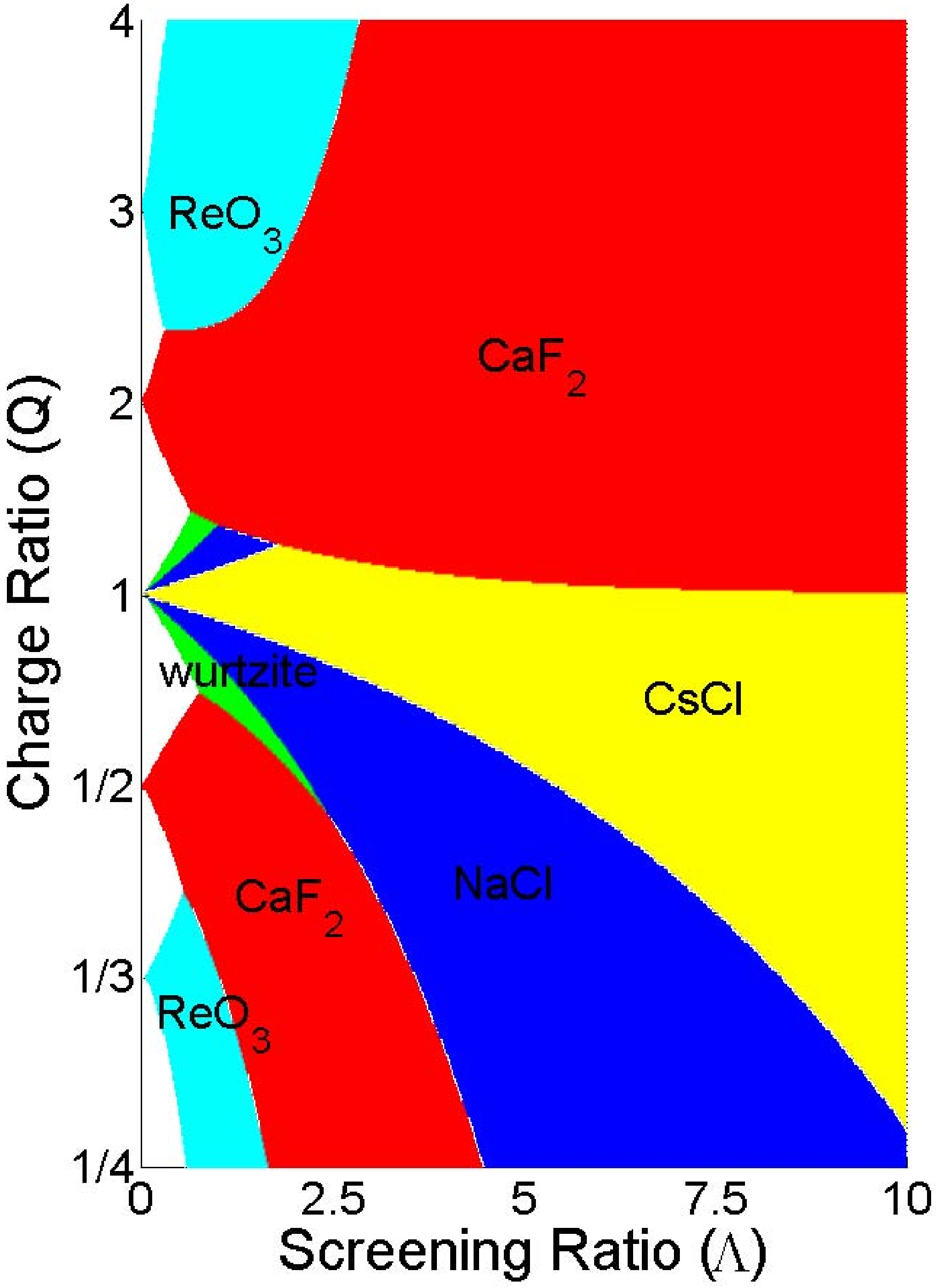

Figure 4.9: The phase fields of the structures considered in this study are shown under the constraint of a limited number of the larger particle. Charge ratio is defined in terms of the charge of the large particle over that of the smaller particle.

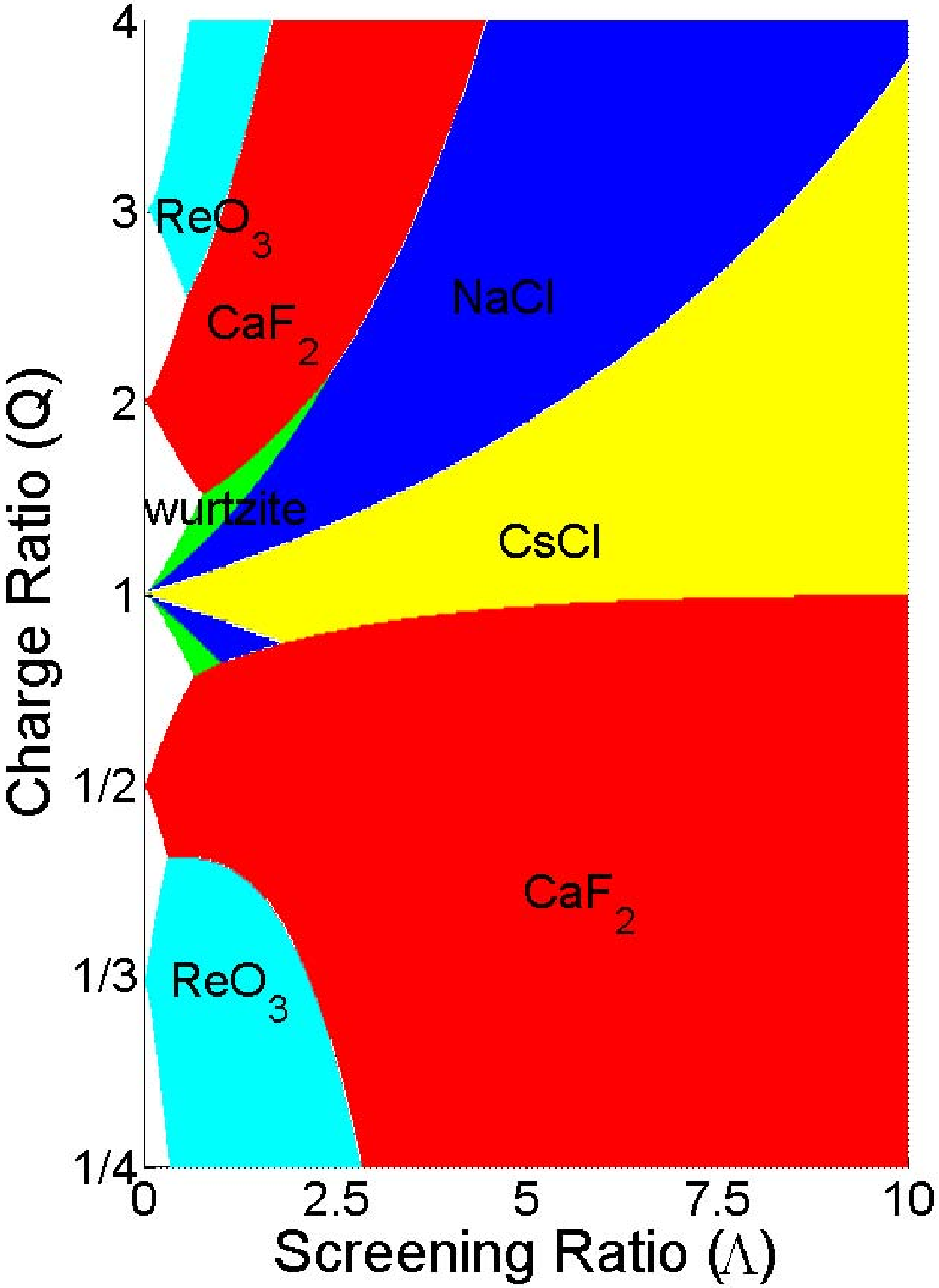

Figure 4.10: The phase fields of the structures considered in this study are shown under the constraint of a limited number of the smallest particle. Charge ratio is defined in terms of the charge on the large particle over that of the smaller particle. Note that this constraint gives a very similar result to that in Figure 4.9.

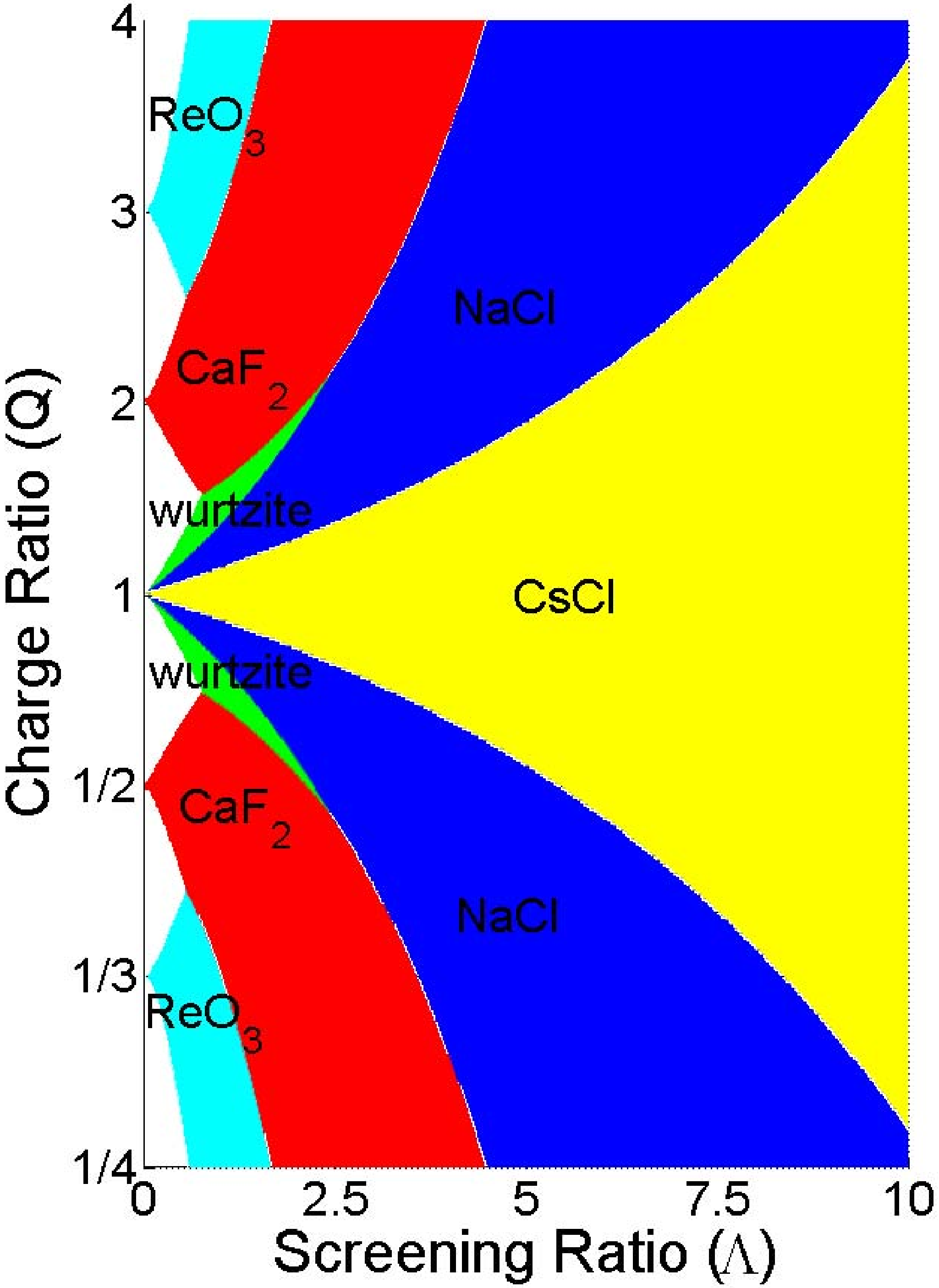

Figure 4.11: The phase fields are shown for the structures considered in this study under the constraint of a 1:1 number ratio of particles. This constraint gives the largest accessibility of the AB structures. Here the accessible structures are reciprocally symmetric about *Q* equals one.

While only six structures were considered in this study, many other structures could dominate a given parameter space. For example, with a charge ratio of $Q$=1.5, an $A_2B_3$ structure could be stable over those considered here. Likewise, charged vacancies could also compensate any deviation in charge ratio from the ideal case. However, even with the consideration of more $A_xB_y$ structures where $x \neq y \neq 1$, the 1:1 number ratio diagram should still show large regions of AB structure stability because these structures utilize all of the available particles.

## 4.3 Effect of Specific Particle Systems

For further insight into ionic colloidal crystal behavior, the dimensionless parameters under this formulation can be solved with respect to one another. The resulting equation gives the constrained phase space accessible to a system of fixed surface potentials and sizes.

$$Q(\Lambda) = -\frac{a_1\psi_1}{a_2\psi_2}\exp\left(\Lambda\frac{a_1 - a_2}{a_1 + a_2}\right) \tag{4.13}$$

$$Q(\Lambda) = -R_{Size}R_{\psi}\exp\left(\Lambda\frac{R_{Size} - 1}{R_{Size} + 1}\right) \tag{4.14}$$

Two new dimensionless parameters emerge that characterize the properties of a specific system of particles: the size ratio ($R_{Size}$) and the surface potential ratio ($R_{\psi}$). These ratios are also defined in terms of the value of the largest particle over that of the smaller particle. Note that this definition causes this size ratio to be the inverse of that used in the Pauling's rules description above.

Equation 4.14 reduces to the classical electrostatic charge ratio when $\Lambda$ equals zero. As the amount of screening increases, the magnitude of the point charge representation of the larger particle increases exponentially. The more dissimilarity in the particle sizes, the more quickly the charge ratio changes.

Figure 4.12 shows plots of Equation 4.14 on the 1:1 number ratio phase diagram for several $R_{Size}$ and $R_{\psi}$ values. Note that the function is always increasing with increasing $\Lambda$ as the point charge representation of the larger particle is increasing most rapidly. Once the size ratio and surface potential ratio are set, the only variable left in the system is the ionic strength of the solution. Increasing the ionic strength moves the system parameters down the curve (i.e. to higher $Q$ and $\Lambda$ values). Therefore, the most stable structure for a given system can be altered by varying the ionic strength of the solution.

## 4.5 Effect of Polydispersity

While great improvements have been made in narrowing the dispersity of particle systems, some degree of polydispersity is still present. The dispersity in particle size is given by the coefficient of variation (CV), which is defined as the standard deviation of the average particle size normalized to the particle size. While a few percent polydispersity seems insignificant, this can have a large impact on the phase stability for an ionic colloidal crystal. Figure 4.13 illustrates the particle system curves for a single polydisperse system with an ideal size ratio of two and a surface potential ratio of one half. The black regions represent the polydispersity with the edge of the black regions corresponding to one standard deviation above and below the average particle size for each type. The implications of polydispersity can be more significant if the size ratio falls near a change in site filling as given by Pauling's Rules. In this case, two different types of site filling may compete in the system, which could result in a barrier to crystallization due to competing equilibrium phases. While ideally a system would have no polydispersity, I have chosen to limit the dispersity of the test systems to 3% in order to minimize any hindrance of crystallization from polydispersity while still allowing a range of systems to be available for testing.

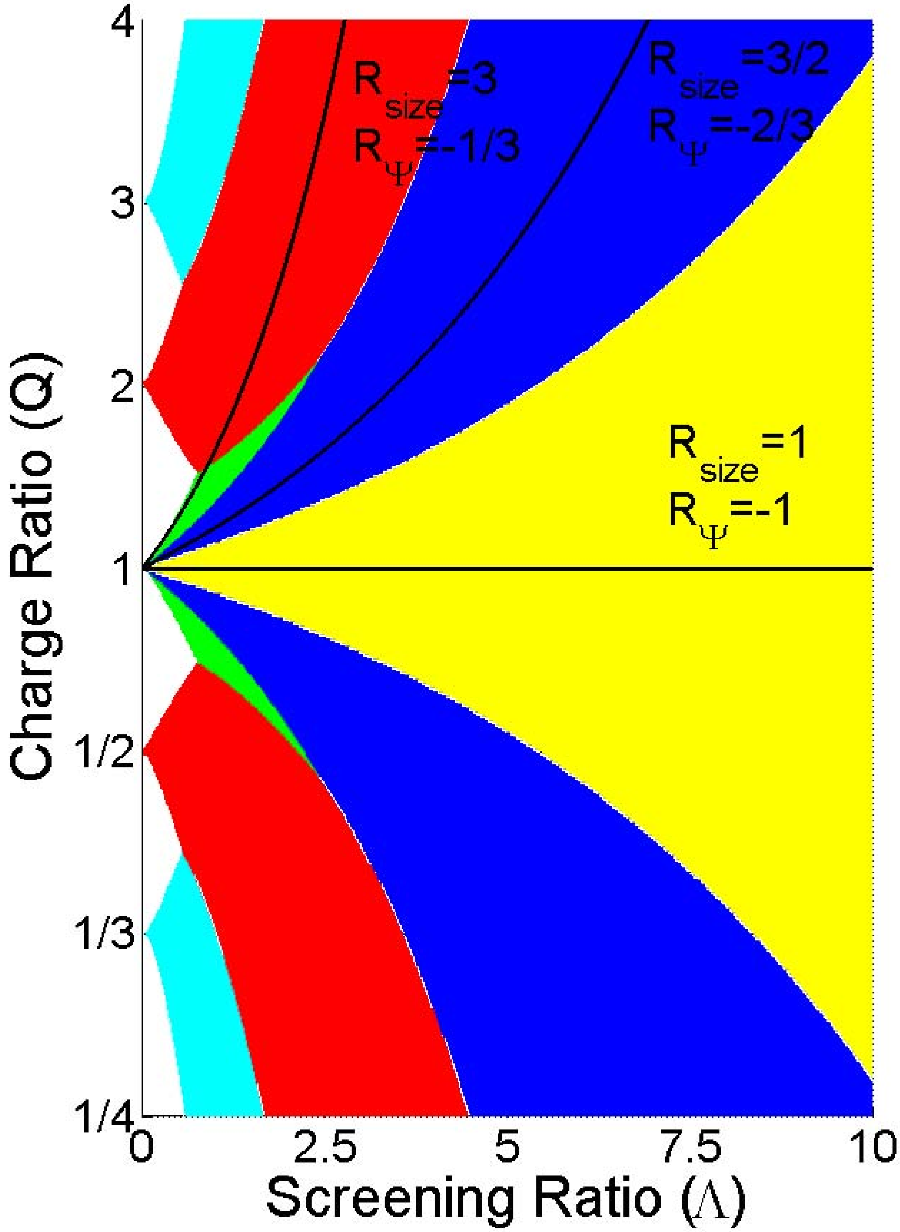

Figure 4.12: Particle system curves for specific particle systems are plotted over the ICC phase diagram. $R_{size}$ and $R_\Psi$ are chosen to fix the $\Lambda$=0 charge ratio at 1. The curvature of the function is solely dependant on the size ratio of the particles. For size ratios very near one, the charge ratio stays nearly constant across a wide range of Λ. The only variable along these curves is the ionic strength of the suspension. Depending on the starting charge ratio, many phase fields may be crossed, possibly allowing for structural changes based on ionic strength.

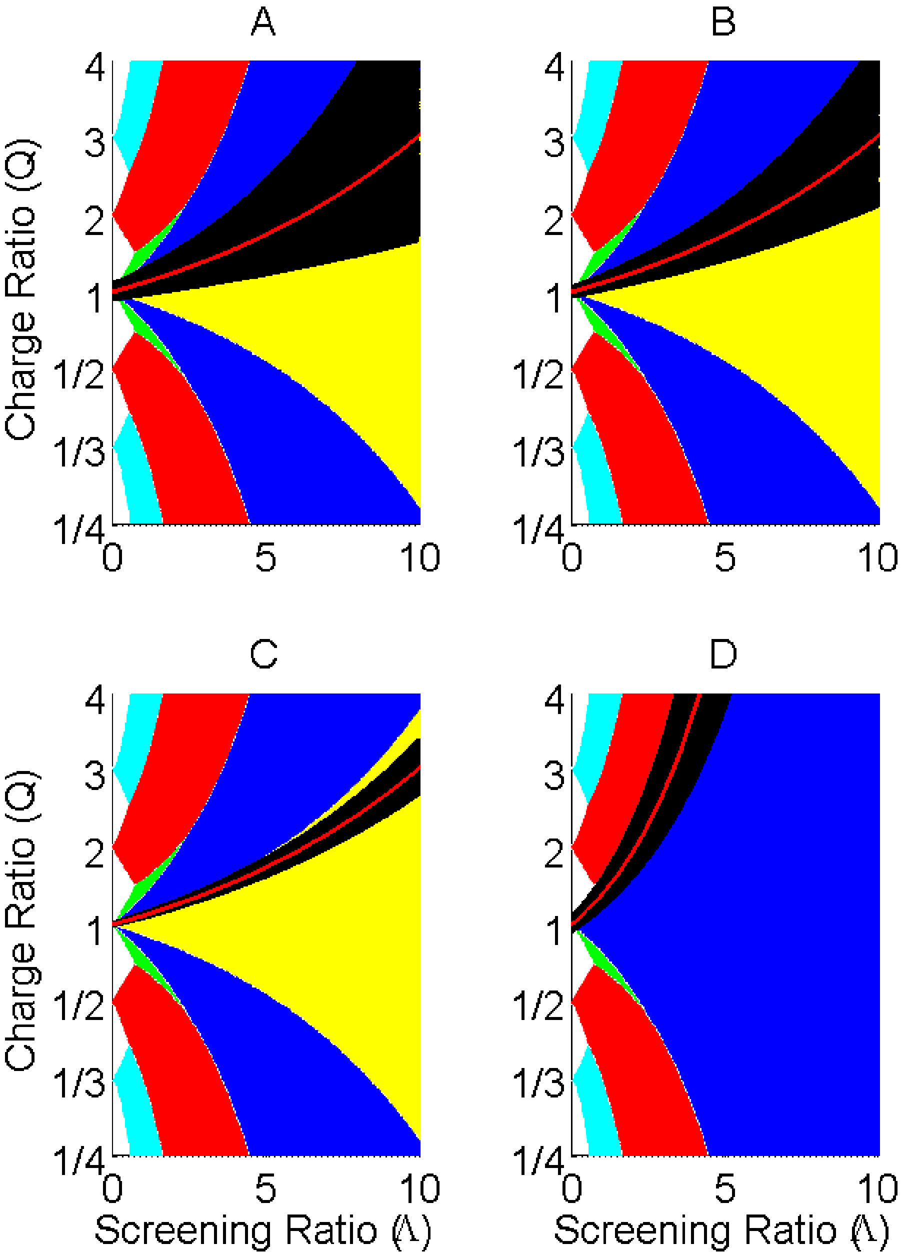

Figure 4.13: The effect of polydispersity in a variety of systems is shown. The red line shows Equation 4.14 for the ideal system, while the black regions indicate all combinations within one standard deviation of the ideal particle sizes. A-C show a system with $R_{size}$=5/4 and $R_{\Psi}$=4/5 and CV's of 5%, 3%, and 1% respectively. D shows a system with $R_{size}$=2 and $R_{\Psi}$=1/2 with a CV of 5%. The effect of dispersity is much larger in systems with size ratios near one. In A, B, and D, more than one phase is stable within one standard deviation of the ideal particle sizes. Dispersity can also result in a variety of site filling types under Pauling's rules, further complicating the phase behavior. In D, the cesium chloride phase field is eliminated by Pauling's rules.

## 4.6 Discussion of Results

The results presented in this chapter provide a framework to study ionic colloidal crystal formation. While the potentials are only first-order models, the charge ratio and screening ratio parameters give insight into the critical variables in a chosen system. The formation behavior of heterocoagualtes has not been previously tied to the charge ratio of the system. The charge ratio (which is slightly modified from Equation 4.9 in later chapters) will be shown to accurately predict colloidal phase behavior through the experiments presented in Chapter 9.

The screening ratio is also shown to be very important in crystal formation. The screening ratio must be kept small to enable sufficient mobility to allow reconfiguration from initial contact states. Without this reconfiguration, a system is unable to crystallize. This is supported by literature work where short-range interactions can only make either a liquid or glass-like state, but cannot rearrange into more complex structures. It is estimated that a $\Lambda$ value of below three is needed for significant mobility to be present in heterocoagulates below their melting points.

A further illustration of the importance of the range of the potential can be understood by considering three cases as shown in Figure 4.14. The first case is a high ionic strength solution with one particle stuck to the surface of the aggregate. The second is a low ionic strength solution. The final is that of an isolated dipole pair. If the potential is very short ranged, as indicated by the green circle in the leftmost drawing, the interaction holding the particle on the surface is equivalent to the interaction between the dipole pair members at a similar ionic strength. In this case, the energy barrier to move the particle from one surface site to another is very similar to that required to split the dipole pair. This effective temperature required is therefore similar to the plasma temperature required to ionize the whole structure. In this case, the system will have no mobility. However, in the case of the system with the longer potential reach, repulsive interactions also contribute to the energy of the particle on the surface. Here a much lower energy is required to have reconfiguration. The Madelung summation approach gives a means to determine the reach of the potential and shows the necessity for low ionic strengths or small particle sizes.

Beyond the need for low ionic strengths, this simple thought experiment also illustrates the necessity of mitigating other short-range attractive forces, such as van der Waals forces, through the addition of surfactants. Clearly a van der Waals dominated system will have little mobility and will be unable to restructure into an ordered array from the its initial hit and stick position.

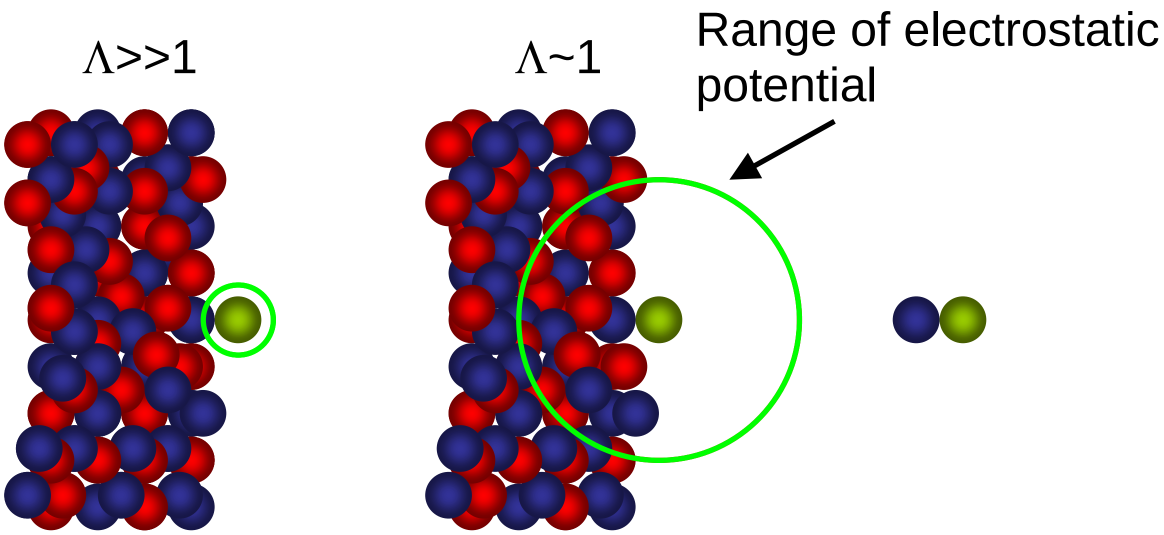

**Figure 4.14: Three cases are shown for an illustration of the importance of short range potentials. In the first case (left), interactions are dictated by only the nearest neighbor due to the short range of the potentials. The energy for reconfiguration is then very similar to that for the dipole pair (right). This energy will make a colloidal gas or plasma. However, the low ionic strength case (middle) has a much lower reconfiguration energy due to the similar particle repulsion. This thought experiment illustrates why systems dominated by van der Waals forces or DNA bridging generally either have no mobility or are fully dispersed with little reconfiguration.**

# Chapter 5: Preliminary ICC Experiments

In Chapter 4, preliminary analysis of the stability of ICCs placed constraints on the system parameters. Both a solvent and particles that adhere to these constraints must be identified for the candidate experimental system. Even though the results in Chapter 4 are first-order estimated, some of the parameters are already highly constrained from this analysis and it is unlikely that a higher order analysis would soften these constraints. Silica and polystyrene functionalized with amidine in the solvent 2-propanol was identified as a preliminary ICC candidate system.

## 5.1 Solvent Selection

The solvent is essential for forming surface charges on the particles as well as for moderating electrostatic interactions between the particles. In order for strong surface charges to develop, a polar solvent is necessary. Even with this constraint, the possible solvent list is still quite large, containing water, most alcohols, acetonitrile, and acetone, among others. Because the choice of positive particles is limited to polystyrene particles, as is discussed in the next section, many more solvents are eliminated because they dissolve polystyrene. The remaining list is significantly shortened, containing only alcohols and water.

To choose between alcohols and water, the ionic strengths of these solvents must be considered since the results of Chapter 4 indicate that a low ionic strength is necessary to stabilize ICCs. Water can be purified nearly completely, and 2-propanol is available in an ultrahigh purity semiconductor grade. The conductivity of ultrahigh purity water is known to be 18.2 MΩ-cm, but the exact value of the 2-propanol conductivity is difficult to determine due to a lack of conductivity standards beyond 0.5 MΩ-cm. A YSI 3200 series conductivity meter with a cell constant of 0.1/cm probe was used to measure this conductivity. A three-point calibration was first done with Traceable One-Shot conductivity standards at 0.175, 0.104, and 0.010 MΩ-cm. Although these conductivity standards are far below the estimated conductivity of the 2-propanol, they were the closest conductivity standards that could be obtained. Using this meter, the conductivity of 2-propanol was determined to be upwards of 500 MΩ-cm.

The starting conductivities of the candidate solvents must be converted to ionic strengths in order to be useful for ICC calculations. The work of Wu and Berezansky [105] gives the limiting equivalent conductivities, which relates the conductivity to the concentration of ions, for several different ions in both alcohols and water. This quantity can be used to relate the measured conductivity to the ionic strength.

$$\Lambda^0 = 1000\left(cm^3 / L\right)\frac{K}{c} \tag{5.1}$$

For $H^+$ ions in water, the equivalent conductivity is approximately 426 $S \cdot cm^2$/equiv. This value is estimated from the conductivity of HCl in water, which is approximately three times greater than that of NaCl or KCl due to the high mobility of the $H^+$ ion. For *n*-propanol, the equivalent conductivity of HCl is only 30 $S \cdot cm^2$/equiv. From these values, the ionic strength of the ultrahigh purity water is found to be $1.3\times10^{-7}$ mol/L, which is very close the actual value of $2\times10^{-7}$ mol/L. Alternatively, the ionic strength of the ultrahigh purity 2-propanol, which was estimated with the equivalent conductivity of *n*-propanol, is found to be $6.7 \cdot 10^{-8}$ mol/L.

While the ionic strength of the 2-propanol is lower than that of the water, the important value for ICC stability is the Debye parameter, which also depends on the solvent dielectric constant.

$$\kappa = \left( \frac{2 z_i^{\,2} e_c^{\,2} c_i^{*}}{\varepsilon_0 \varepsilon_r kT} \right)^{1/2} \tag{5.2}$$

There is a factor of four between the dielectric constants of water (78.6) and 2-propanol (20). The Debye parameter at 300K is evaluated to be $1.46 \times 10^{6}$ m$^{-1}$ for the water and $1.68 \times 10^{6}$ m$^{-1}$ for the 2-propanol. Despite the higher purity of the 2-propanol, the two solvents screen electrostatic forces very similarly.

Other factors must be considered in the solvent choice, including the drying behavior, the stability on exposure to the environment, and the effect of solvent parameters on the strength of interactions. The drying front of water on most substrates exerts large forces and therefore will tend to pull particles away from their settled positions. On the other hand, 2-propanol wets many substrates much better, preventing a strong drying front from sweeping through the system. This drying behavior allows samples to be dried with little movement of the particles from the state in which they settled from solution.

Additionally, water readily absorbs carbon dioxide from the atmosphere, making it essential to limit exposure to air. For 2-propanol, the main contaminant is water, also requiring a limited exposure to air. Either solvent should therefore be used in a controlled environment. However, 2-propanol does have the advantage that the ultrahigh purity form can be purchased and is stable in bottled form for over one year, while bottled water can only be purchased at a purity of approximately 1 MΩ-cm, which increases the Debye parameter to $12.3 \times 10^{6}$ m$^{-1}$. Any ultrahigh purity water used must therefore be produced on site by expensive water purification equipment immediately before use.

Finally, the electrostatic interactions as given in Equation 2.33 scale with the dielectric constant. As heterocoagulation is often considered to be irreversible, weakening electrostatic interactions (i.e. bond strengths) are believed to improve the probability of successful ICC formation due to improved kinetics. This hypothesis is further discussed in Chapter 6.

Therefore, in consideration of these factors, ultra-high purity (Class 1) 2-propanol was chosen as the solvent for the experimental system. The 2-propanol used was obtained from General Chemical Corporation (through Hubbard-Hall). Because the purity of 2-propanol is affected by exposure to air, it was used under an Argon environment in a glove box. The conductivity of the solvent was measured using the above mentioned meter immediately upon pouring and subsequently over several hours. The results are shown in Figure 5.1. The conductivity falls logarithmically with time, but is still above 150 MΩ-cm after several hours.

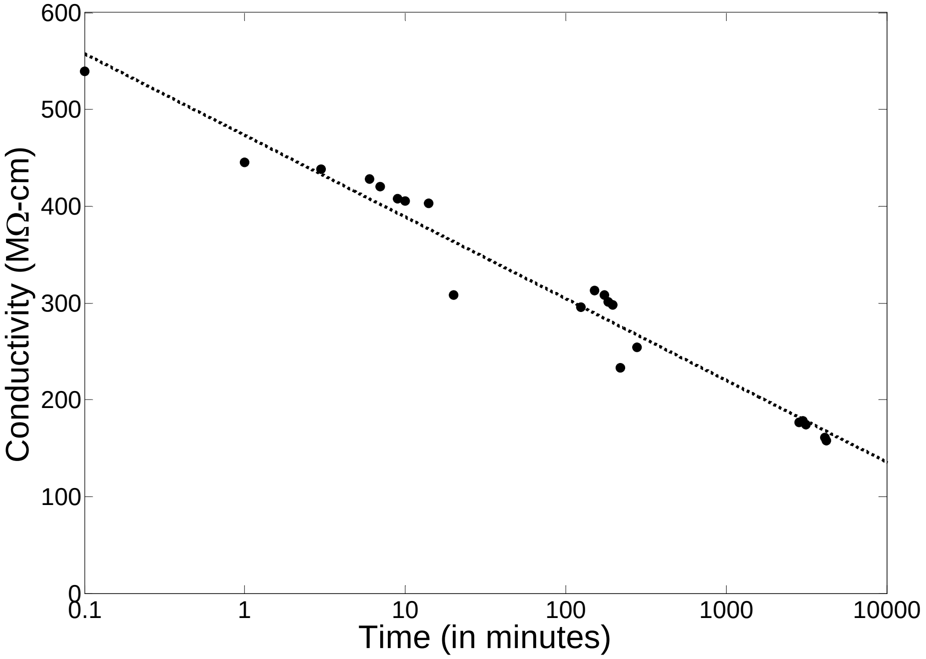

Figure 5.1: The conductivity of 2-propanol in the Argon environment in which it will be used is measured over several hours. The conductivity decreases logarithmically over time, but only falls to 158 MΩ-cm after almost 2 hours. This trend shows that it is still important to limit the time the 2-propanol is exposed to the Argon environment, but an order of magnitude increase in ionic strength is only achieved after about 24 hours of exposure.

## 5.2 Particle Selection

While many factors impact particle selection, the largest constraint is that the particles must have two dissimilar signs of surface charge. Among commercially available particles, there are only a few choices for positively charged particles. Polystyrene particles functionalized with amidine or quaternary amine carry a strong positive surface charge. However, the low effectiveness of amidine and amine as polymer initiators increases the dispersity of these particle for small particle sizes. Many more selections exist for negatively charged particles, including silica and polystyrene functionalized with sulfate groups. Due to the difficulty in distinguishing similar size particles, a size ratio of approximately two was targeted, which should form the rocksalt structure at a charge ratio of one. From Equation 3.12, a size ratio of two requires the magnitude of the surface potentials to be more than a factor of two different in order to achieve a charge ratio around one.

The zeta potentials of many different particles were measured in order to identify a system that satisfies the above constraints on the surface potentials. A Brookhaven Instruments Zeta-PALS system was used to measure particle mobilities, and the Huckel model was used to convert these values to zeta potentials. This method is discussed in Chapter 2. Before conducting the measurements, the instrument was tested using a standard provided by the manufacturer. Between five and ten measurements of 50 acquisitions each were conducted and averaged for each particle sample to reduce error. Additionally, this was done several times for many samples to verify the reproducibility of the results. Due to the high viscosity of 2-propanol (2.04 cP), the response of the particles to the applied electric field is much smaller than that in water, making accurate measurements difficult. This is sometimes reflected by a large difference in zeta potential between two samples of the same type of particle. Table 5.1 shows several systems that were measured and the resulting zeta potentials.

Table 5.1: Zeta potential results for several different particle types and sizes in 2-propanol. The large variability from trial to trial is due to the low mobility of particles in 2-propanol. Zeta potentials are all calculated with the Huckel model. Particles were either obtained from IDC Latex or Duke Scientific, or produced via the Stober method [106].

| Source | Size (microns) | Material | Functionalization | Trial | Mobility | Standard Error | Zeta Potential |
|---|---|---|---|---|---|---|---|
| IDC | 0.76 | PS | Amidine | 1 | 0.62 | 0.02 | 99.65 |
| IDC | 0.76 | PS | Amidine | 2 | 0.48 | 0.02 | 76.81 |
| IDC | 0.37 | PS | Amidine | 1 | 0.73 | 0.08 | 117.84 |
| IDC | 0.37 | PS | Amidine | 2 | 0.62 | 0.20 | 100.18 |
| IDC | 0.21 | PS | Amidine | 1 | 0.55 | 0.05 | 87.80 |
| IDC | 0.21 | PS | Amidine | 2 | 0.63 | 0.04 | 102.14 |
| IDC | 0.096 | PS | Sulfate | 1 | -0.48 | 0.05 | -78.62 |
| IDC | 0.096 | PS | Sulfate | 2 | -0.34 | 0.02 | -55.27 |
| IDC | 0.11 | PS | Sulfate | 1 | -0.63 | 0.01 | -101.96 |
| IDC | 0.14 | PS | Sulfate | 1 | -0.54 | 0.02 | -87.04 |
| IDC | 0.19 | PS | Sulfate | 1 | -0.66 | 0.01 | -107.12 |
| IDC | 0.18 | PS | CML | 1 | -0.35 | 0.11 | -55.53 |
| IDC | 0.5 | PS | Chloromethyl | 1 | -0.37 | 0.02 | -59.49 |
| IDC | 0.47 | PS | Carb/Sulf | 1 | -0.63 | 0.04 | -101.40 |
| IDC | 0.31 | PS | Amine | 1 | -0.34 | 0.03 | -54.31 |
| Duke Sci | 1.48 | Silica | | 1 | -0.23 | 0.01 | -36.99 |
| Duke Sci | 1.48 | Silica | | 2 | -0.20 | 0.03 | -32.49 |
| Duke Sci | 0.5 | Silica | | 1 | -0.05 | 0.02 | -8.54 |
| Stober | | Silica | | 1 | -0.55 | 0.02 | -88.44 |

These particles were obtained from various sources. There are several companies that manufacture particles. IDC Latex has a wide variety of polystyrene spheres with many sizes and functionalizations. Duke Scientific carries monodisperse silica and polystyrene, but has a narrow selection. Bangs Laboratories also carries particles, but have little selection of highly monodisperse particles (<5% dispersity). It is also possible to fabricate monodisperse spheres instead of buying commercially available ones, but this path was avoided for preliminary studies as it can be very difficult and time-consuming. One batch of Stober silica were the only particles fabricated for these studies.

The purchased particles come suspended in water. To resuspend them in 2-propanol, vacuum filtration was used to remove the residual water. The remaining particles were then harvested and redispersed using ultrasonication and vortexing. For large polystyrene particles and all silica particles, this resuspension method was very effective. However, small polystyrene particle (<500 nm) could not be fully redispersed in this manner.

From the results in Chapter 4, a monodisperse system is necessary to prevent the competition of multiple phases. Figure 5.2 shows a system with a dispersity of 5% for one particle and 8% for the other. This system shows significant size variations, making it difficult to distinguish particle types. Thus, dispersities smaller than 5% are necessary. In choosing the particle system, the largest difficulty was in finding highly monodisperse positively charged particles. The smallest system tested that satisfied the monodispersity constraint was the 760 nm polystyrene functionalized with amidine (CV of 2%). The 1560 nm silica from Duke Scientific was chosen as a low surface potential, monodisperse (CV of 3%) negative particle. This system satisfies the size and surface potential ratio constraints mentioned previously. Figure 5.3 shows the first-order phase regions predicted by the Madelung sum method for this system.

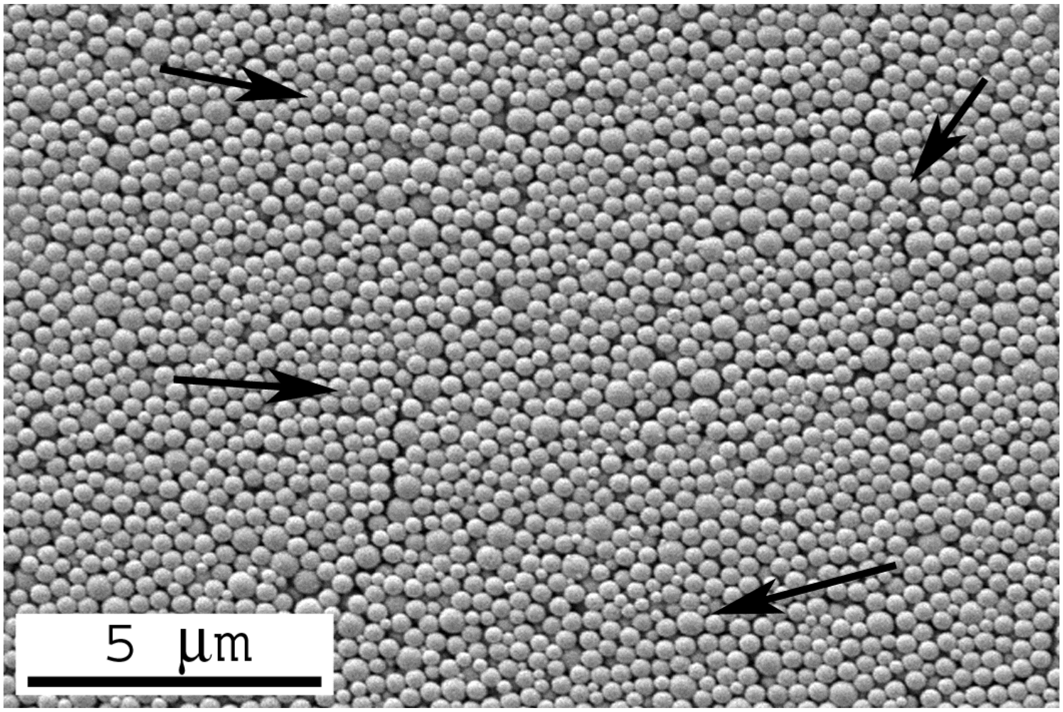

Figure 5.2: This system is composed of 0.37 μm polystyrene functionalized with amidine from IDC Latex (5% CV) and 0.49 μm silica from Duke Scientific (8% CV). The large dispersity results in a system that appears to have a continuous distribution of particle sizes, four of which are indictated in the figure. This large dispersity makes it difficult to identify the particles and frustrates order.

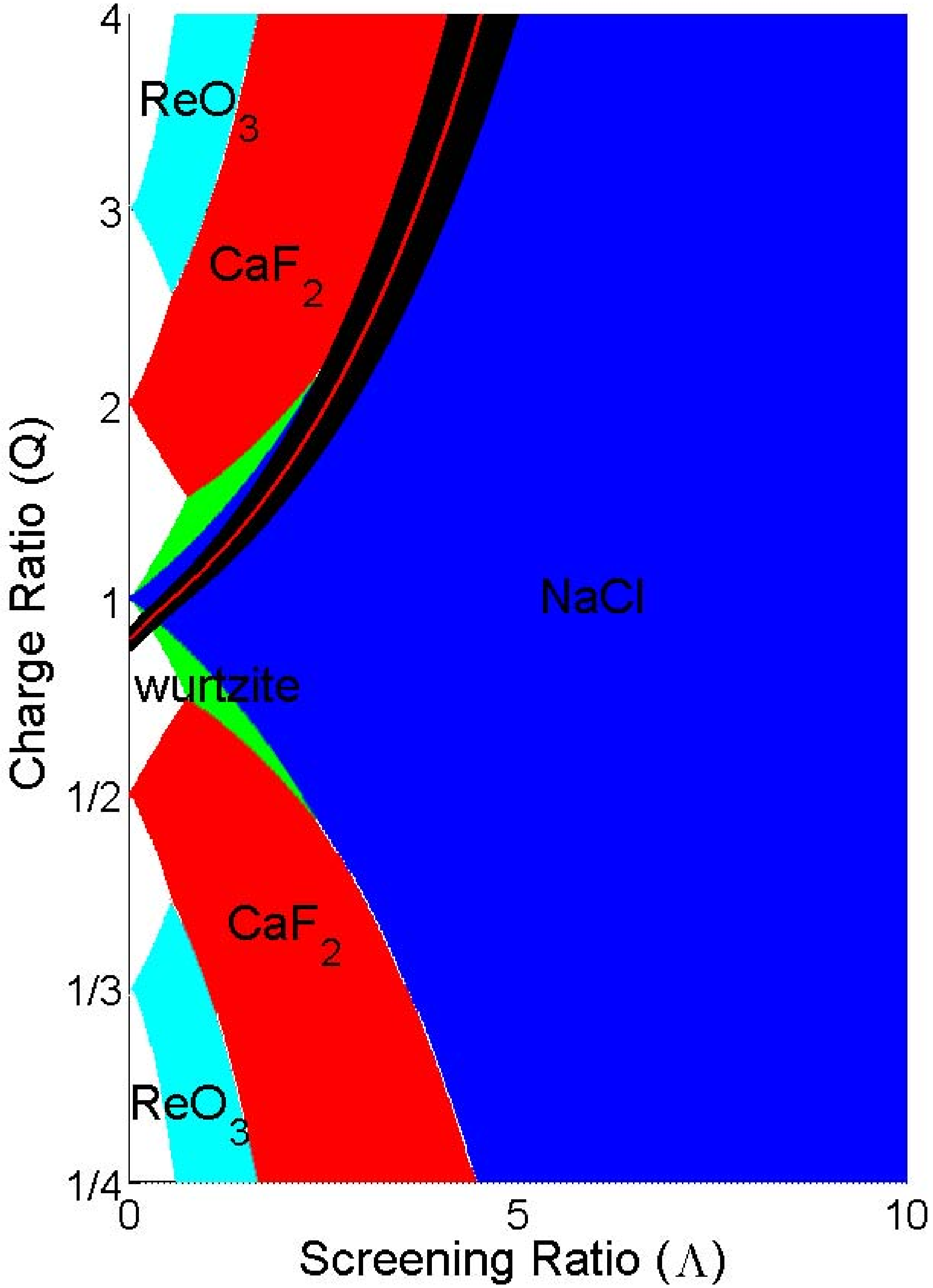

Figure 5.3: The effect of dispersity for the selected preliminary system is shown on the phase fields calculated in Chapter 4. The particles are 1.58 μm silica (-39 mV) and 0.76 μm polystyrene functionalized with amidine (+88 mV).

## 5.3 Particle Concentration Measurements

After the identification of a system and the transfer into 2-propanol, the number concentration of particles in the test solutions must be identified in order to control number ratio and to allow accurate number ratios to be obtained. To do this, a known quantity of solution, usually diluted by 10:1 from the concentrates to allow for more accurate volume measurement, was placed in a weighing dish and dried. The weighing dish was weighed ten times on a Mettler Toledo AG285 precision balance (0.00001g accuracy) both before introducing the solution and after drying. From the residue mass and the particle size, the number concentration of particles in the solution could be readily determined. Because the large particle solutions settle over time, they must be vortexed to assure homogeneity before transfer to the weighing dish. These measurements were performed at least once on each solution before mixing with other particles.

## 5.4 Mixing Experiments

Mixing experiments with various concentrations and number ratios were conducted under a wide variety of conditions, including free settling in a Petri dish, ultrasonication, drying in vials, centrifugation in vials, freeze-drying, salt concentration variations, and settling on single-component seed-crystals. While small ordered regions were observed under several conditions, the highest density of nuclei resulted from free settling of mixtures in Petri dishes.

Although the number ratio in initial samples was not carefully controlled, small amounts of ordering were still observed as is shown in Figure 5.4. These samples were produced from mixing controlled volumes of silica and polystyrene particles. Through careful control and tailoring of the number ratio, the observed size of ordered regions increased. The largest ordered regions were observed with 5mL of a 1:1 number ratio mixed and settled in a Petri dish. The volume fraction of particles in the solution was approximately 1%. Regions from this sample are shown in Figure 5.5.

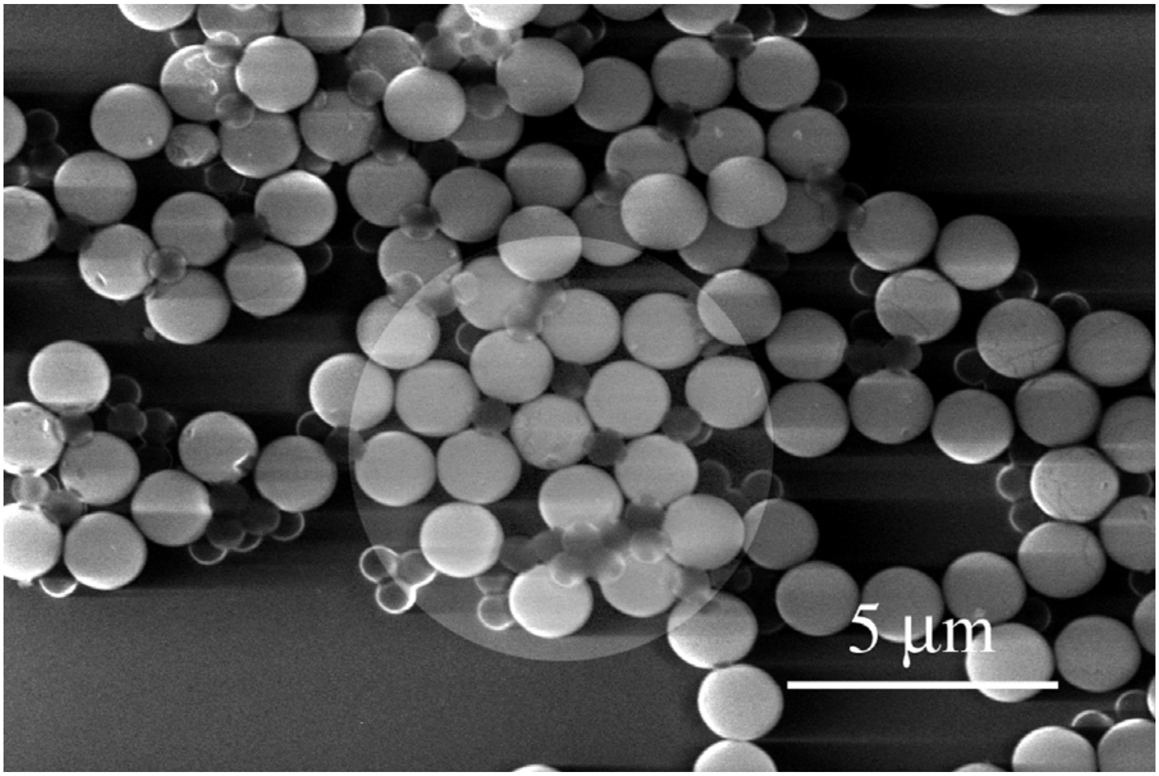

Figure 5.4: A micrograph of the first small region of ordering observed via environmental scanning electron microscopy is shown. Improvements were later made in imaging the particles, but the presence of incipient ordering is still visible.

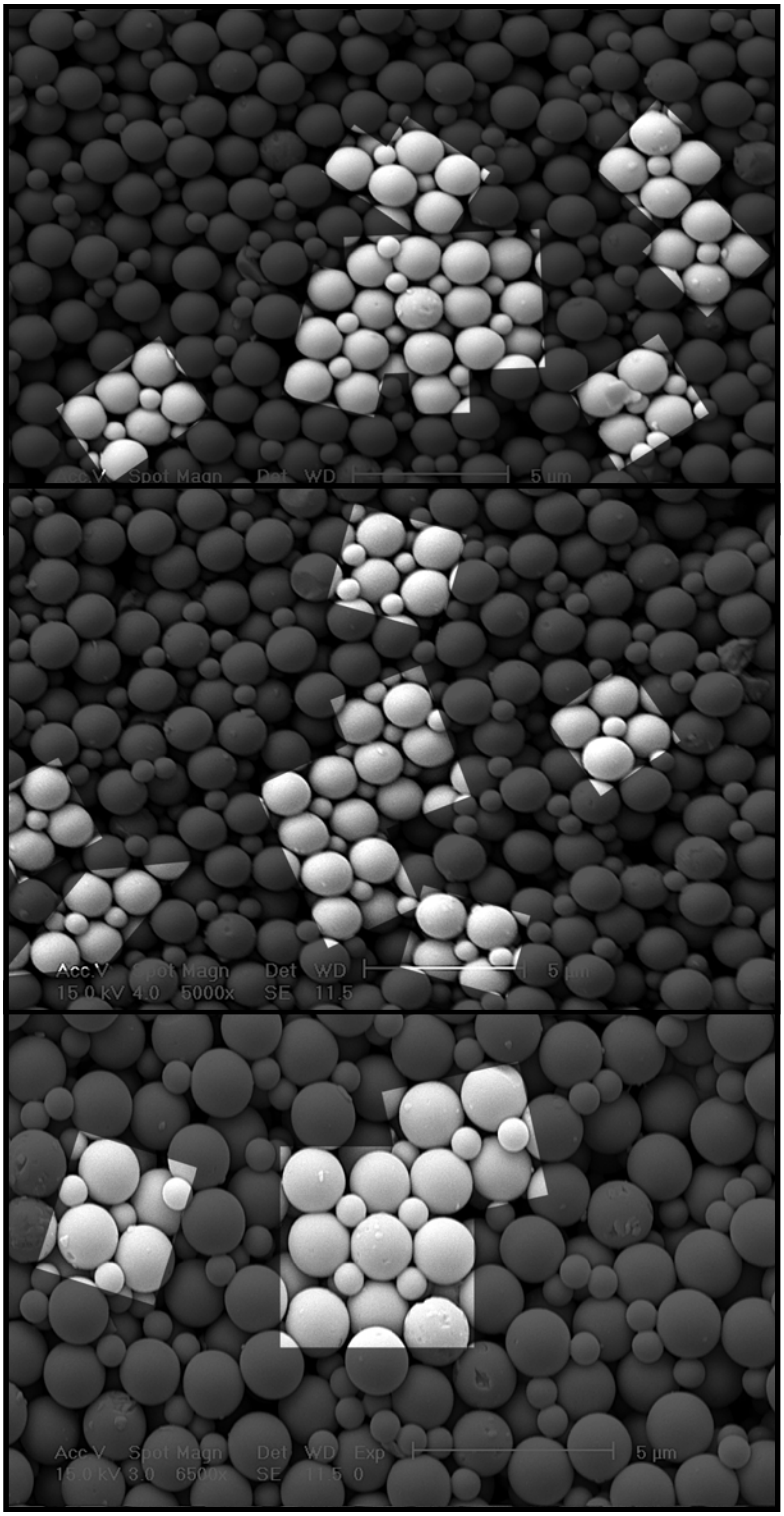

Figure 5.5: Several regions demonstrating order in a sample of silica (1.58 μm) and polystyrene functionalized with amidine (0.76 μm) settled and dried in a Petri dish. Regions demonstrating order were easier to find in these samples, where the number ratio of particles was tailored to be near 1:1.

Many methods were used in an effort to improve crystalline order. Ultrasonication was employed in an attempt to increase the particle mobility. Small ordered regions were still present in ultrasonicated samples, but there were no signs of growth. Centrifugation was used to increase forces on heterocoagulates in an attempt to collapse any gel-like structures that might exist before drying. Again, large ordered regions were not observed. The increased forces ranged from 5 to 40 g.

Control samples were produced with large salt concentrations. However, despite large $\Lambda$ values, nuclei were still observed. The charge ratio in these sample was larger than 1000. Finding ordered regions under these conditions is inconsistent with ICC formation under any published interaction potential for heterocoagulation. However, as will be shown in Chapter 8, this can be understood and explained in the context of complete electrostatic energy calculations where the charge ratio is shown to be constant for high ionic strengths.

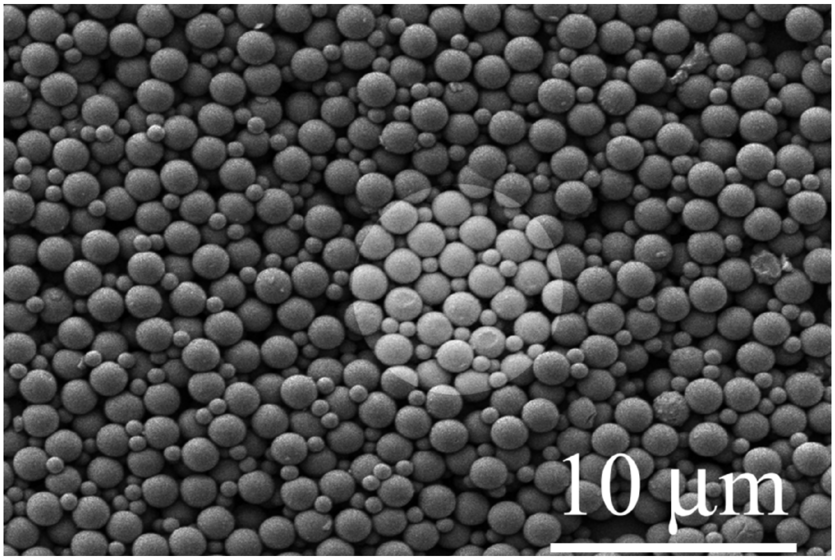

Figure 5.6: Small ordered regions were also observed in high salt suspensions (2-propanol saturated with NaCl). This would not be expected under the theory of Chapter 4, but can be explained through the complete electrostatic calculations of Chapter 8.

## 5.5 Discussion of Experimental Results

While some local ordering was present in this test system, only small regions were observed. Although the thermodynamic evaluation of the system would suggest crystallization should occur, the kinetics have not been considered. If the system is substantially undercooled or the Λ value is too high, a metastable glassy state will result even if crystallization is favored. These results demonstrate a need to further understand the kinetics and to tailor systems such that crystallization is possible both thermodynamically and kinetically at room temperature.

While random settling is always a possible explanation for such an observance, it should be remembered that this is an attractive electrostatic system where bonds in the solution are expected to form very rapidly. While it can be rightfully argued that small regions of 4 or 5 particles may occur by random settling, large regions of 20-30 particles are not easily dismissed. Under classical heterocoagulation models, the system would form a low density diffusion-limited aggregation structure. Higher density structures that are observed here imply that the system is exhibiting some mobility, although this may be limited to the initial organization of dipoles and not the dense state. Once settled the system is exhibiting little mobility as evidenced by the lack of growth of crystalline regions.

# Chapter 6: Brownian Dynamics Simulations of ICCs

A colloidal system is composed of three major components: the colloids, the salt ions, and the solvent in which they are dispersed. Practically, simulating a system large enough to accurately reproduce heterocoagulation behavior requires the salt ions and solvent to be treated as a continuum through Poisson Boltzmann theory. This is because the number of colloids is small relative to the number of salt ions and solvent molecules, and the mobilities of the salt ions and the solvent molecules are much larger than that of the colloidal particles. Once this approximation is made, two major simulation approaches are available: particle dynamics and Monte Carlo methods. As one would expect, both methods are useful in different circumstances. In this thesis, both approaches were used to study ICC formation. This chapter will focus on the particle dynamics simulations, while the Monte Carlo results will be presented in the next chapter. The next section will give a brief introduction to the concepts relevant to both Brownian Dynamics and Monte Carlo.

## 6.1 Simulating Colloidal Suspensions

A variety of approaches are available to model the behavior colloidal suspensions [107]. Two of the most popular are Brownian dynamics simulations and Monte Carlo methods. While Brownian dynamics is applicable for many suspension densities, basic Monte Carlo methods work well only for dense colloidal suspension. For dilute suspension, cluster Monte Carlo methods have been developed.

With either particle dynamics or Monte Carlo simulations, the appropriate thermodynamic ensemble must be determined. An ensemble is defined by the system parameters that are held constant during the equilibration of the system. Several ensembles will be discussed: microcanonical, canonical, grand canonical, and isothermal-isobaric. Although more ensembles exist, these are the most frequently used and relevant ensembles for colloidal systems.

The microcanonical ensemble (*NVE*) is the ensemble where the number of particles (*N*), the system volume (*V*), and the total energy (*E*) are held constant. For a colloidal system, the simulation space contains a vast number of solvent molecules and salt ions in addition to the atoms in the colloids themselves. As will be explained later, the computational expense of modeling each individual solvent molecule is usually avoided with little error by treating it as a viscous medium (imposing Stokesian drag), which also imparts random fluctuations on the particles (Brownian motion) and alters electrical potentials according to the Poisson-Boltzmann equation. This treatment would be impractical with a microcanonical ensemble as the total energy of the modeled system (just the colloidal spheres) is not conserved, as energy is constantly transferred back and forth from the particles to solvent.

The canonical ensemble (*NVT*) is a treatment where the temperature (*T*) of the system is held constant, along with the number of particles and the volume. This ensemble is more representative of the conditions present in a real experimental system.

In fact, the Helmholtz free energy (free energy at constant temperature and volume) is easily obtained with a canonical ensemble treatment. Therefore, this ensemble is one of the most relevant to modeling colloidal materials. It is also among the easiest to implement.

The grand canonical ensemble ($\mu VT$) holds the chemical potential ($\mu$) of the system constant, along with the volume and temperature. This ensemble requires the creation and destruction of particles in order to maintain a constant chemical potential. Thus, this ensemble is difficult to implement for dense colloidal suspensions because these systems have few interparticle spaces big enough to support another particle.

The final ensemble discussed here is the isothermal-isobaric ensemble (*NPT*), which is similar to the canonical ensemble except the pressure is held constant instead of the volume. To implement this ensemble, a mechanism must be created to allow volume changes. While this is can be easily achieved in Monte Carlo methods, it has not to our knowledge been implemented for Brownian dynamics. One advantage of this ensemble is that a periodic system can be easily treated without imposing an artificial fixed volume on the system. Furthermore, this ensemble allows the simulated system to achieve its equilibrium density under a given applied pressure. The Gibbs free energy can also be obtained from this ensemble.

## 6.2 *NPT* versus *NVT*

For ionic colloidal crystals, the *NPT* and *NVT* ensembles are the most easily implemented. Brownian dynamics simulations were conducted under the *NVT* ensemble, while Monte Carlo simulations were conducted with both ensembles. For an attractive colloidal system, it is necessary to treat the *NVT* ensemble with non-periodic, hard-wall boundary conditions. As electrostatically attractive systems gain significant energy upon densification, periodic boundary conditions would lead to negative pressures for those colloidal systems, i.e. the internal energy increases with a decrease in volume. The boundaries prevent the crystal from densifying, leading to an artificially higher internal energy. As the pressure is defined as the negative partial derivate of the internal energy with respect to volume, the pressure is negative as densification would lower the system energy.

Conversely, the *NPT* ensemble can be used with either periodic or hard-wall boundary conditions. However, in this thesis, periodic boundary conditions were generally used with this ensemble in order to obtain bulk properties, such as the coefficient of thermal expansion of an ICC.

Because the *NPT* ensemble requires the application of a constant pressure, the use of this ensemble raises the question: What is the pressure exerted on a colloidal system? First, consider the pressure exerted by other colloidal particles on a crystal or dense colloidal liquid that has formed from the suspension. This pressure is linearly proportional to the momentum transfer upon the collision of the particles with the system, as well as the collision rate and the number of particles. The collision rate is considered to be proportional to the velocity of the particles.

$$P \propto Npv = Nmv^2 \tag{6.1}$$

From statistical mechanics, the kinetic energy of the particles is known to be equal to 1.5kT in three dimensions. Thus, the pressure is found to be independent of the mass of the particle.

$$P \propto 3NkT \tag{6.2}$$

This is consistent with the ideal gas law, where the pressure is given by Equation 6.3.

$$P = \frac{NkT}{V} \tag{6.3}$$

Treating the colloidal particles as an ideal gas, the pressure can be determined using the above equation. This can be rewritten in terms of the volume percent and the particle sizes.

$$P = \frac{\%_{volume}}{\frac{4}{3}\pi a^3} kT \tag{6.4}$$

Clearly, the size of the particles has a very large impact on the pressure, with the pressure decreasing rapidly with increasing particle size. Yet, even for very small particles of 100 nm in diameter in a one volume percent solution, which would be among the smallest experimental systems, the pressure is only 0.08 Pascal. For a similar system of 1 micron particles, the pressure is negligible at $8\times10^{-5}$ Pascal. Clearly, the pressure exerted by the residual colloidal suspension is very small. As the colloidal particles are surrounded by the solvent, it only exerts a hydrostatic pressure on individual particles and not one that would push two particles closer together or affect their interactions in any significant way. Therefore, the solvent pressure is ignored.

As the residual number of particles in suspension is not generally known, the pressure is also unknown. However, the pressure can be estimated from the initial volume percent of particles in suspension. For a given system, the energy required to expand against this estimated pressure can be compared to the electrostatic energy loss for a volume expansion. Any expansion is not of the solvent, but only the particle system, as the solvent flows freely between the particles. Also, for the same reason, the expansion is not performed against the solvent, but only the colloidal particles still in suspension. Therefore, for all but high volume fraction colloidal systems, the particle systems *P*d*V* work is found to be insignificant relative to other energy changes in the system, making it possible to set the pressure in the simulations equal to zero with little loss of accuracy.

## 6.3 Particle Dynamics

In traditional dynamics simulations, the equations of motion for a colloidal particle are solved numerically by discretization. At any instant in time, the acceleration of a particle can be directly determined from the forces acting on it through Newton's First Law of Motion. The particle's position at any time can then be determined by integrating the acceleration twice. Generally, this integration cannot be performed without the choice of a discrete time step. While many integration schemes can be imagined, one of the simplest schemes is the Verlet algorithm[108], which results in the following governing equation.

$$a_i(t)=\frac{\sum_{j\neq i} F_{ij}}{m_i}=\frac{d^2 r_i(t)}{dt^2}\cong\frac{r_i(t+\Delta t)-2r_i(t)+r_i(t-\Delta t)}{\Delta t^2} \tag{6.5}$$

$$r_i(t+\Delta t)=\frac{\sum_{j\neq i} F_{ij}}{m_i}\Delta t^2+2r_i(t)-r_i(t-\Delta t) \tag{6.6}$$

In this simple algorithm, the force is assumed to be constant over the entire time step. To reduce the effects of such approximations, higher order schemes such as the Gear Prediction-Corrector algorithm [109] can be used. These schemes involve following higher order derivatives of the position to better integrate the equations of motion. For ICCs, the electrostatic interaction energy comes in the form of a potential well. The difficultly with these schemes arises in ensuring that energy is conserved during the integration of the potential well. Ideally, a particle set to motion in a potential well will simply oscillate back at forth without losing energy. However, different integration schemes will tend to either lose or gain energy. It is practically impossible to perfectly conserve energy.

### 6.3.1 Simplified Particle Dynamics

Three types of forces are present in a colloidal system: particle-particle interactions and other body forces, hydrodynamic forces, and Brownian forces. This leads to equations of motion that are initially more complex than those in atomic system simulations.

$$m_i \ddot{x}_i = \sum_{j \neq i} F_{ij} + F_{Hydrodynamic} + F_{Brownian} \tag{6.7}$$

Brownian forces are generally considered to be independent of the hydrodynamic and particle-particle interactions, allowing them to be uncoupled. Thus, this initial formulation will only include simple drag forces (a subset of hydrodynamic forces) and particle-particle interactions.

When the solvent is treated as a continuum, the hydrodynamic term in Equation 6.7 is given by the drag force acting upon a particle moving through the solvent.

$$m_i \ddot{x}(t) = m_i \frac{dv_i(t)}{dt} = \sum_{j \neq i} F_{ij} - \beta v_i(t) \tag{6.8}$$

Since the particle-particle forces are independent of velocity, this differential equation can be solved to give the velocity of the particle for a given time step.

$$v_i(t) = v_{o,i} \exp\left(-\frac{\beta}{m} t\right) + \frac{\sum_{j \neq i} F_{ij}}{\beta} \left[1 - \exp\left(-\frac{\beta}{m} t\right)\right] \tag{6.9}$$

As the time step becomes large relative to *m/β,* Equation 6.9 reduces to the terminal velocity of the particle. If the time required to reach terminal velocity is small relative to the time step of the simulation, the particle can be treated as if it was traveling at its terminal velocity for the entire time step. Figure 6.1 demonstrates the rate at which particles modeled by Equation 6.9 approach the terminal velocity. In colloidal dynamics simulations, time steps are often much greater than *m/β*, incurring little error with this assumption.

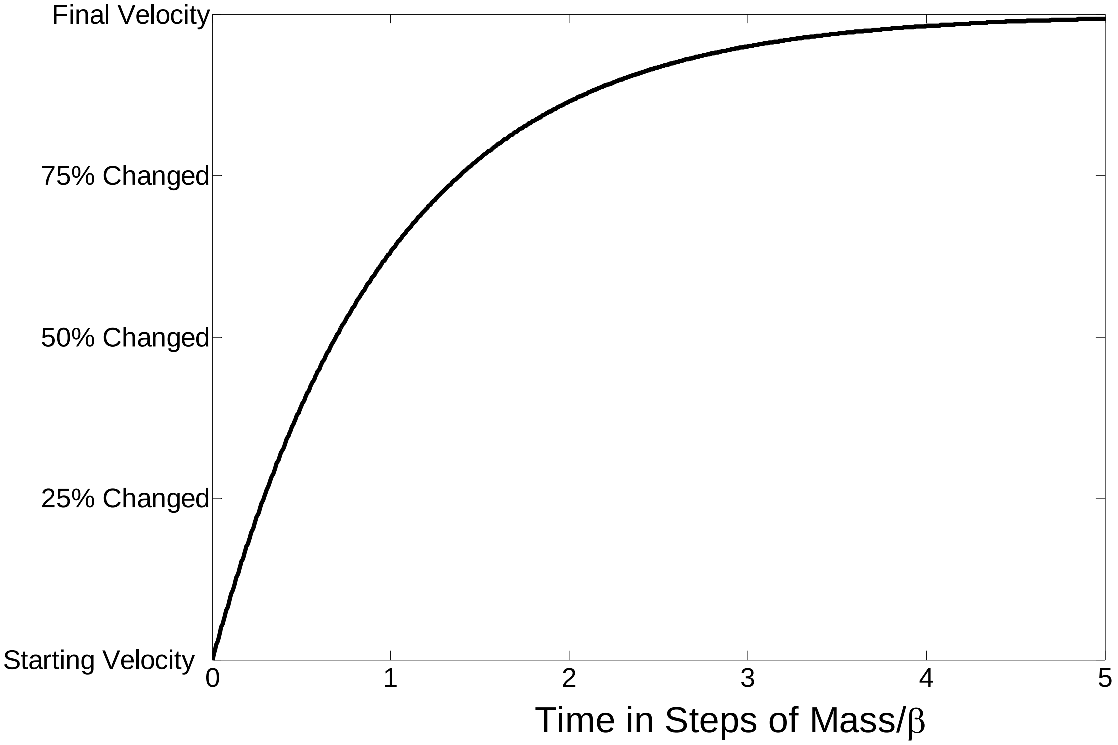

Figure 6.1: The time required for the velocity to reach a terminal value is shown. For time steps much large than *m/β*, a particle can be assumed to be at the terminal velocity dictated by the applied force (*F/β*) for the entire time step with little error.

Through this assumption, the motion of the colloidal particles reduces to a first-order differential equation (Equation 6.10). This simplification leads to a differential equation that is numerically stable under all time steps, allowing a large time step to be used. As a result, simulations that use this assumption run many orders of magnitude faster. The simplified equations of motion are shown below.

$$m_i\ddot{x}(t) = 0 = \sum_{j\neq i} F_{ij} - \beta_i v_i(t) \tag{6.10}$$

$$v_i(t) = \frac{\sum_{j\neq i} F_{ij}}{\beta_i} = \frac{dx(t)}{dt} \cong \frac{x(t+\Delta t) - x(t)}{\Delta t} \tag{6.11}$$

$$x(t+\Delta t)=\frac{\sum_{j\neq i}F_{ij}}{\beta_i}\Delta t+x(t) \tag{6.12}$$

The Brownian term's contribution to particle displacement must be considered as well. From Chapter 2, particles undergoing Brownian motion experience a zero average displacement but a finite RMS displacement given by Equation 6.14.

$$\langle r_{Br}(t)\rangle=0 \tag{6.13}$$

$$\langle r_{Br}^2\rangle=\sqrt{6Dt}=\sqrt{6\frac{kT}{\beta}t} \tag{6.14}$$

Thus, for a single time step, the RMS displacement is given by Equation 6.14 with *t* equal to Δ*t*. An appropriately scaled Gaussian distribution satisfies these constraints as well as being the solution to the diffusion equation in Chapter 2.

Therefore, instead of treating a Brownian force, a random displacement satisfying Equation 6.14 can be added to the final particle position from Equation 6.12. The combined result is a displacement due to the damped particle-particle interactions combined with a Gaussian displacement due to the Brownian motion.

$$r(t+\Delta t)=\frac{\sum_{j\neq i}F_{ij}}{\beta_i}\Delta t+r(t)+\langle A\rangle\sqrt{\frac{6kT\Delta t}{\beta}} \tag{6.15}$$

Here *A* is a Gaussian deviate sampled using an appropriate random number generation scheme [110].

## 6.3.2 Full Solution for a Constant Force

At this point, the validity of the approximation uncoupling the Brownian and force terms is further evaluated. The full solution to Equation 6.7 can be calculated without uncoupling the Brownian contribution. The Brownian driving force that should be substituted into the equation is given by the chemical driving force derived in Section 2.2.4. Again assuming that terminal velocity has been reached, Equation 6.7 becomes Equation 6.16.

$$kT\frac{\nabla c_i}{c_i}-\beta v+\sum_{j\neq i}F_{ij}=0 \tag{6.16}$$

This equation can be solved for the RMS displacement of the particle using the same approach presented in Section 2.2.4. First, the terminal velocity is determined.

$$v = \frac{kT}{\beta}\frac{\nabla c_i}{c_i} - \frac{\sum_{j \neq i} F_{ij}}{\beta} \tag{6.17}$$

The flux of particles due to this velocity can be compared to the flux from Fick's First Law of Diffusion to yield the diffusivity of the particles.

$$J = \frac{kT}{\beta}\nabla c_i - \frac{\sum_{j \neq i} F_{ij} c_i}{\beta} \tag{6.18}$$

$$\frac{kT}{\beta}\nabla c_i - \frac{\sum_{j \neq i} F_{ij} c_i}{\beta} = -D\nabla c_i \tag{6.19}$$

$$D = \frac{kT}{\beta} - \frac{\sum_{j \neq i} F_{ij} c_i}{\beta \nabla c_i} \tag{6.20}$$

Substituting the new diffusivity, which is now dependant on concentration, into Fick's Second Law, the solution for the concentration profile of the particles is obtained.

$$\frac{\partial c_i}{\partial t} = \nabla\left(\left[\frac{kT}{\beta} - \frac{\sum_{j \neq i} F_{ij} c_i}{\beta \nabla c_i}\right]\nabla c_i\right) = \frac{kT}{\beta}\nabla^2 c_i - \nabla\frac{\sum_{j \neq i} F_{ij} c_i}{\beta} \tag{6.21}$$

If the particle-particle interaction is constant, the solution of this differential equation is a shifted Gaussian distribution.

$$c_i = \frac{c_0}{8(\pi D t)^{3/2}}\exp\left(\frac{1}{4Dt}\left[r - \frac{\sum_{j \neq i} F_{ij}}{\beta}t\right]^2\right) \tag{6.22}$$

A random sampling from this distribution is easily performed by sampling from an unshifted, normalized Gaussian, multiplying by the standard deviation, and shifting the results according to the applied force. This algorithm is identical to that presented in Equation 6.15. Thus, this result shows that uncoupling the Brownian contribution yields an exact result for a constant particle-particle force. The only assumption in the above derivation is that the particle is at its terminal velocity for the entire time step.

### 6.3.3 Full Solution for a Non-Constant Force

While Equation 6.7 is solvable for a constant particle-particle force, this situation will rarely be encountered in a simulation. Using the formulation of Schulten and Kosztin [111], the error incurred by using the above results for a constant force while having a non-constant force can be found. The results of this formulation reveal that the error can be kept below a certain value by limiting the time-step.

If the force is approximated as constant, the error in the potential after one time step is given by Equation 6.23.

$$U_{error} = U(r) + \frac{\partial U}{\partial r}\Delta r - U(r + \Delta r) \tag{6.23}$$

Solving for *Δr*, the maximum displacement allowable given a constraint on the error can be obtained for certain functional forms. Generally, this maximum displacement is dependant on the initial position in the potential and should be evaluated for a representative potential function for the system being tested.

For the simulation of ICCs, a parabolic well can be fit to most interaction potentials locally, allowing the maximum time step to be determined for that well. Equation 6.24 evaluates Equation 6.23 for a parabolic well.

$$U_{error} = \left(Ar^2 + Br + C\right) + \left(2Ar + B\right)\Delta r - \left(A(r + \Delta r)^2 + B(r + \Delta r) + C\right) = -A\Delta r^2 \tag{6.24}$$

Thus, the error in the energy for a parabolic potential is solely dependant on the step size and not the position within the well. Given a maximum desired error in energy, the maximum allowable displacement is simply the square root of the maximum error over the curvature of the well.

The limiting displacement is reached via a response to the forces in the system, as well as through Brownian motion. From Equation 6.22, the displacement for a constant force is a shifted, scaled Gaussian in the direction of the applied force. Therefore, the largest displacement permissible for a given time step would be a Brownian displacement in the same direction as the applied force. This maximum displacement will be within 3σ (i.e. <*A*> equals 3) from the center of the Gaussian. Solving Equation 6.15 for Δt, the time step that corresponds to this displacement is obtained. As movement is being considered along only one axis (the direction of the force), $2kT\Delta t$ is used instead of the $6kT\Delta t$ for three-dimensions.

$$\Delta t_{\max} = \frac{\beta}{F^2}\left(F\Delta x_{\max} + 9kT\left[1 \pm \sqrt{1 + \frac{2F}{9kT}\Delta x_{\max}}\right]\right) \tag{6.25}$$

The smallest, positive real value of $\Delta t_{\max}$ gives the largest allowable time step. When the force limits to zero, the solution of Equation 6.15 instead collapses to a single value.

$$\Delta t_{\max} = \frac{1}{18}\frac{\Delta x^2 \beta}{kT} \tag{6.26}$$

Note that for a parabolic well, if the maximum allowable error is set in terms of kT, Equation 6.26 becomes independent of temperature.

$$\Delta t_{\max} = \frac{1}{18}\left(\frac{U_{error}}{kT}\right)\frac{\beta}{A} \tag{6.27}$$

Thus, at the minimum of a parabolic well, the maximum time step is a constant value at any temperature. This does not hold at other positions in the well, where the maximum allowable time step will always be lower. However, it does serve as a rough guide in selecting an initial time step, especially when the movement due to the force is small relative to the Brownian motion, as is often the case.

## 6.3.4 Time-Step Considerations

While it is important to choose a time step that does not result in significant energetic errors, there are other considerations that are also important. In choosing the time step for a simulation, the diffusivity of a particle relative to the particle size must be considered. A random move that is too large and causes substantial overlap of two particles or the overcoming of barriers that would otherwise be insurmountable will result in anomalous data. The time required for a particle to diffuse a distance equal to a given percentage of the particle's radius can be found using diffusion theory.

$$t = \frac{(\%_a a)^2}{\langle A\rangle^2 6D} = \frac{(\%_a a)^2 \beta}{\langle A\rangle^2 6kT} = \frac{\pi\eta a^3 \%_a^2}{\langle A\rangle^2 kT} \tag{6.28}$$

It is recommended that a value of at least three standard deviations (i.e. <*A*> equals 3) be used for this limiting value of the time step. Equation 6.28 would then correspond to the time it would take for only 0.05% of the particles to diffuse more than the set percentage of the particle's radius. This and the previous upper limit on the time step due to the error must be consistent with the lower limit required to accurately assume terminal velocity behavior ($\Delta t >> m/\beta$). Furthermore, a time step long enough to allow diffusion of several particle diameters over the course of the simulation must be selected in order to reach equilibrium.

### 6.3.5 Full Hydrodynamic Interactions

To gain a more accurate physical description of colloidal behavior, full hydrodynamic forces should be considered. These terms couple the motion of one particle with the motion of another, similarly to how two boats interact through their wakes. Therefore, higher order approaches are required to solve these interactions exactly. However, these corrections are small and should mainly impact only the kinetics of ICC formation. For the purposes of studying ICC thermodynamics, full hydrodynamics should not be necessary.

## 6.4 Brownian Dynamics on an ICC System

For all Brownian dynamics simulations of ICCs, the preliminary experimental system of silica (1.58 μm) and polystyrene functionalized with amidine (0.76 μm) mentioned in Section 5 was used as a model. Their simulated surface potentials ($\Psi_{SiO2}$=-23.7 mV and $\Psi_{PSA}$=114 mV) were tailored to give a $Q$ equal to 1 at a $\Lambda$ of 2.402, give a which corresponds to a system of these particles in high purity (n=1e-7 mol/L) 2-propanol (the solvent used in the experimental investigations). Other solvent properties were chosen to equal those corresponding to 2-propanol. Variations of these parameters for this system were also tested.

Using the method discussed above, the time step required to keep the numerical error below 1/20 kT was calculated for three cases: a particle contained in a crystal, a particle approaching a crystalline surface, and a particle moving parallel to a crystalline surface. Figure 6.2 illustrates these cases.

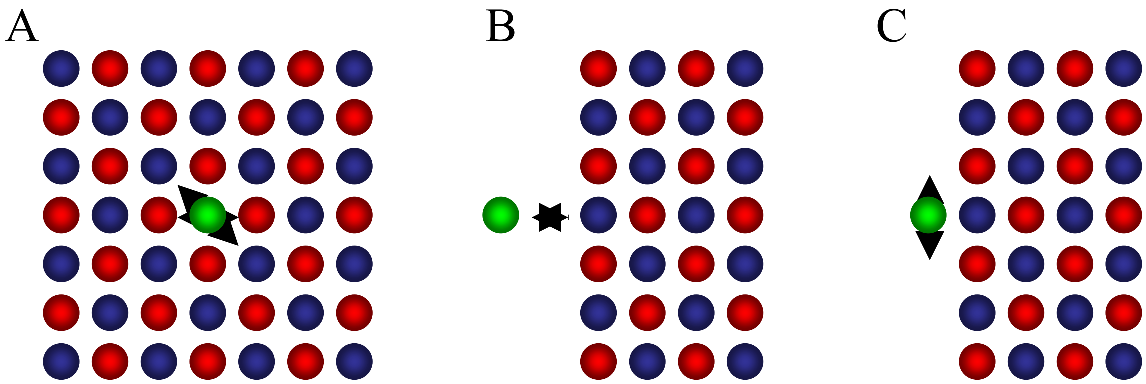

Figure 6.2: The maximum time step allowable was considered for three cases. Case A corresponds to a particle sitting inside a crystal; Case B to a particle approaching a surface; and Case C to a particle moving along a crystalline surface. All cases produced similar maximum time steps at all temperatures for a constraint of 1/20 kT maximum error in energy.

All three cases were tested with two lattice parameters for the same size of particles to verify that thermal expansion would not alter the results significantly. Yukawa-type potentials for each particle in the crystal were summed pair-wise to calculate the potential energy field around the test particle. It was found that locally the energy well for case A was symmetric about the ideal position, so the lattice direction did not significantly alter the critical time step.

Figure 6.3 illustrates the maximum time step calculated for case A at two temperatures and lattice parameters. Likewise, Figures 6.4 and 6.5 illustrate similar conditions for case B and case C. From these results, a preliminary upper bound on the time step was placed at 1e-5 seconds or lower.

While a time step below 1e-5 limits the error in the energy of the system to below 1/20 kT, the maximum movement of the particle must also be considered, as mentioned above. Equation 6.28 gives the limitation placed on the time step to prevent the particles from moving more than a given percentage of the particle's radius. Equation 6.29 evaluates equation 6.28 for the specific system being simulated and a 3σ particle move.

$$\Delta t = \frac{\pi \eta a^3}{\langle A \rangle^2 k} \frac{\%_a^2}{T} = 2.831 \frac{\%_a^2}{T} \tag{6.29}$$

This equation is used to create Figure 6.6. A time step of 8e-6 seconds was used for the full size particle simulations, which corresponds to a maximum 3σ move of approximately 10% of the small particle radius near the estimated melting temperature of 3500 K. Figure 6.7 shows the σ contours for Equation 6.29 evaluated at this time step.

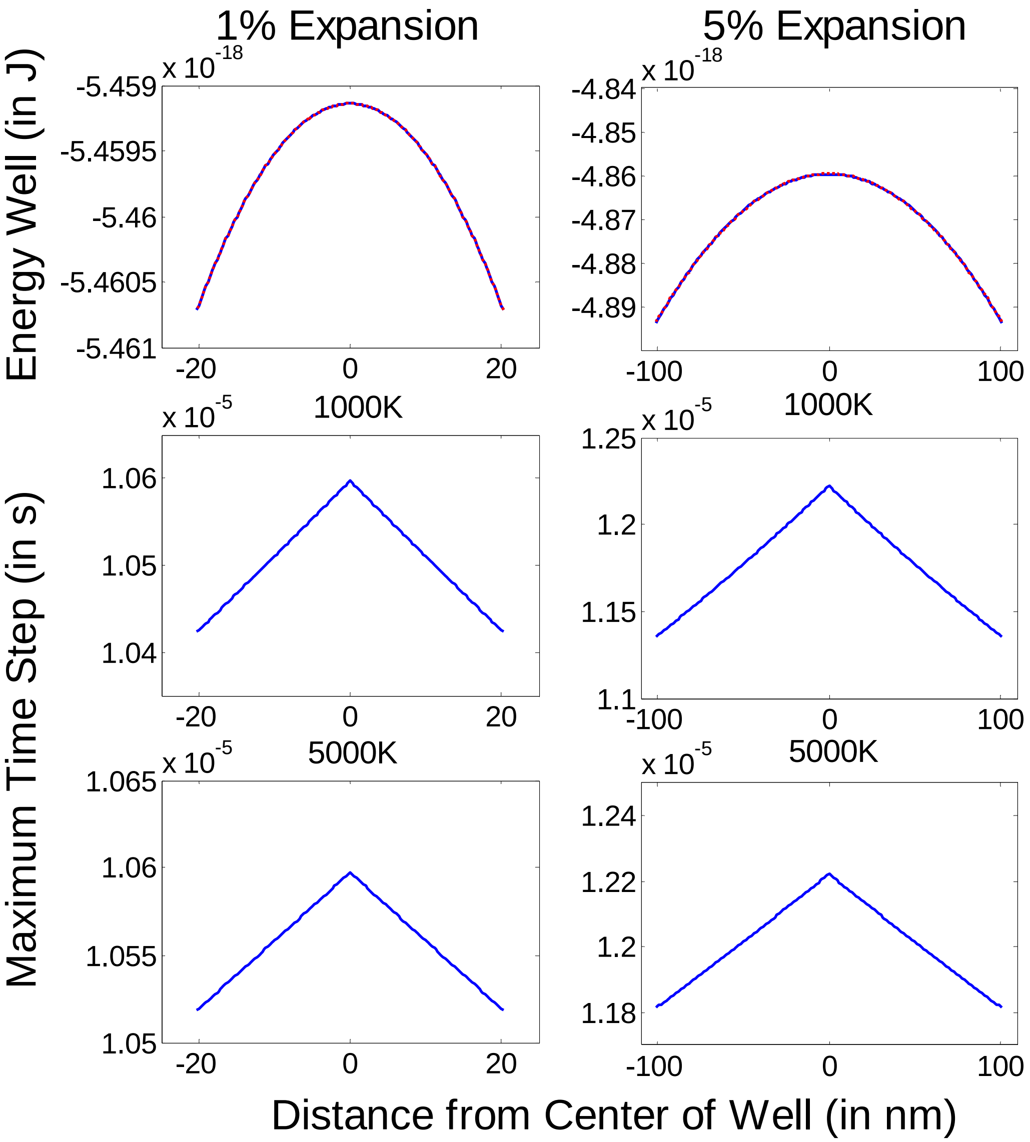

Figure 6.3: The maximum time step allowable for a 1/20 kT error is shown for 1000K and 5000K for a particle in the prototype system moving in a potential well within the crystal (case A). It was found that the potential well was similar in the <100>, <110> and <111> directions. The <111> direction is used here. The potential well is also expanded from being 101% of the particle diameter to 105% of the particle diameter. This accounts for any thermal expansion effects. Note that the critical time step changes by less than 10% with well slope in even the worst case. The temperatures were chosen to bracket the estimated melting temperature.

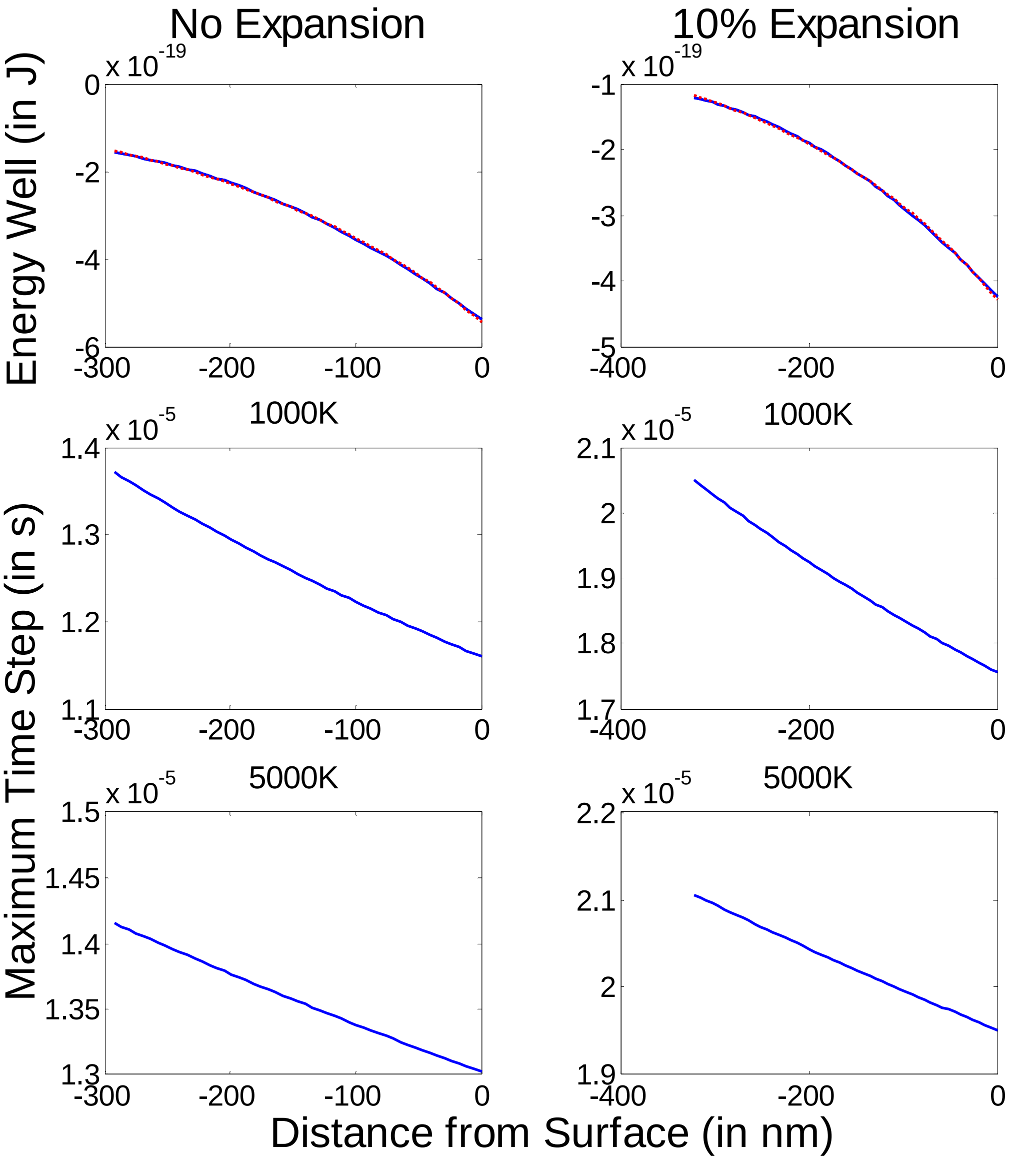

Figure 6.4: The maximum time steps for a particle in the prototype system approaching a crystalline surface from an isolated state (case B) are plotted. Note that the maximum time step is not that different from case A shown in Figure 6.3 despite the dissimilarities in the arrangement of particles. A perfect crystal with no thermal expansion and one with 10% expansion were both tested.

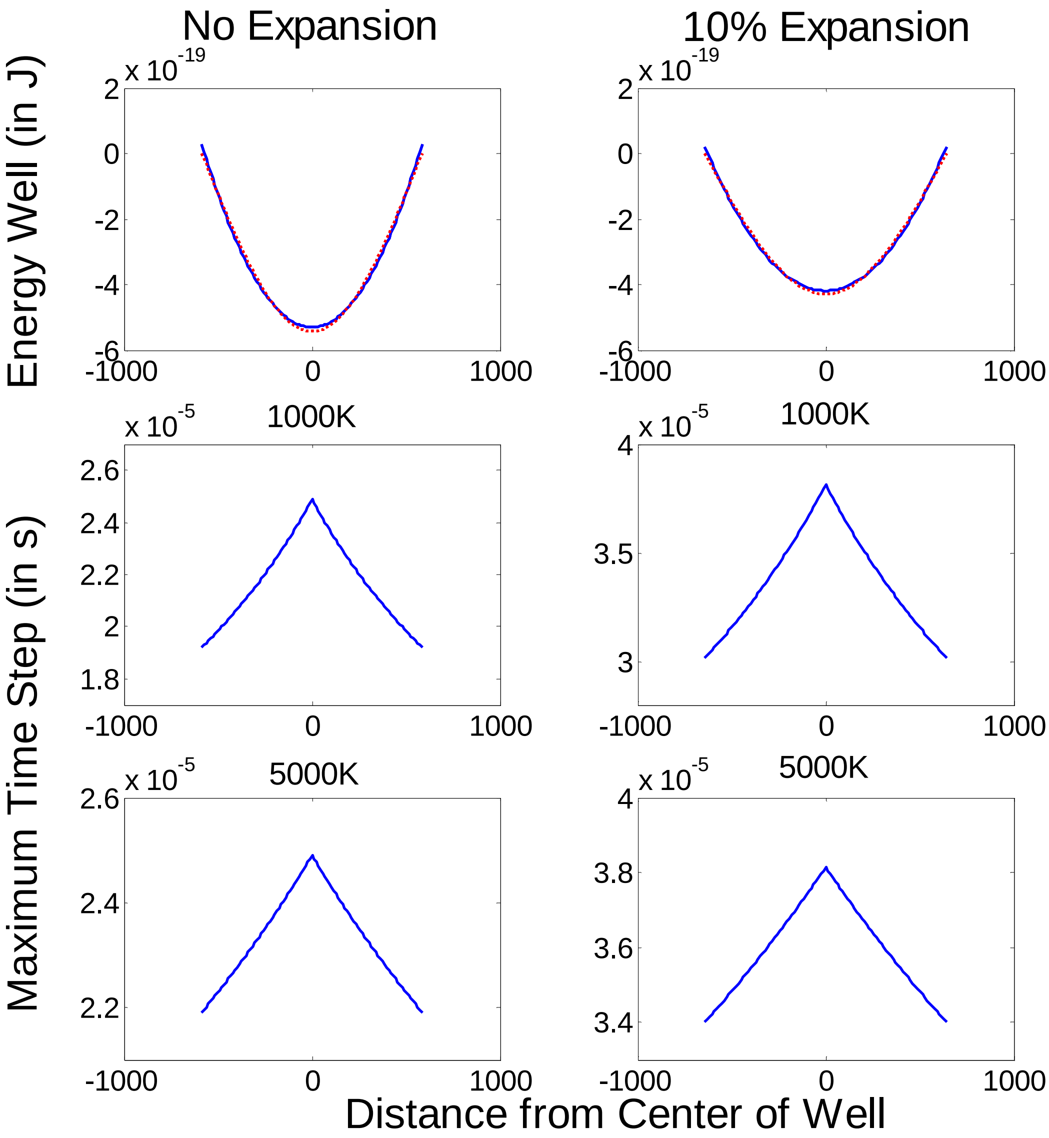

Figure 6.5: Maximum time steps are plotted for the case of a particle in the prototype system moving along a crystalline surface (case C). Again the time steps are very similar to those in Figures 6.3 and 6.4.

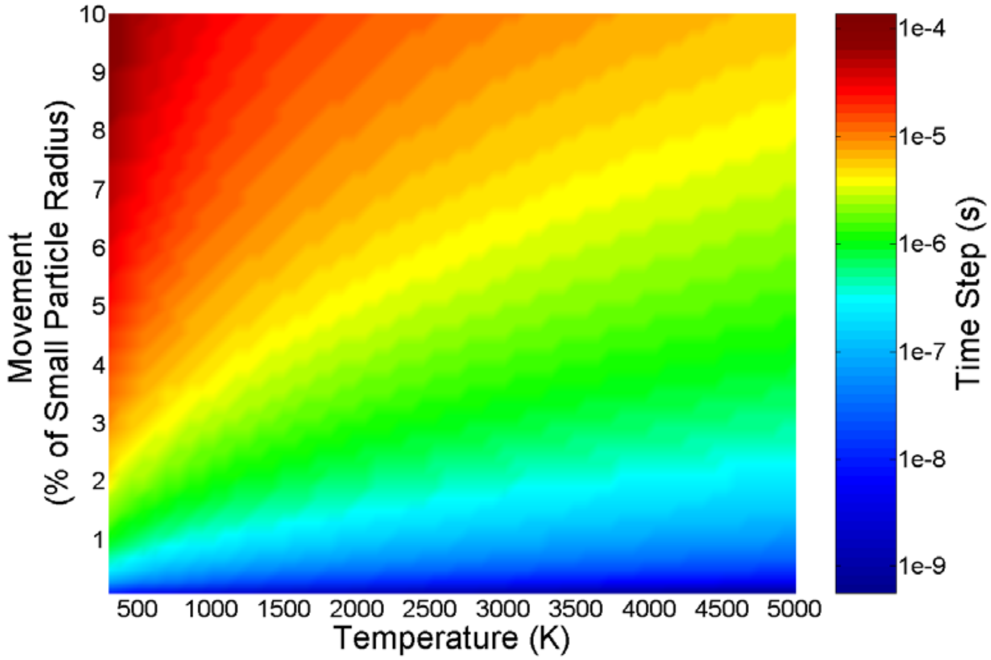

Figure 6.6: The maximum time step for a 3σ movement of the small particle in the test system is shown for a variety of temperatures and allowable maximum movements (relative to the particle size).

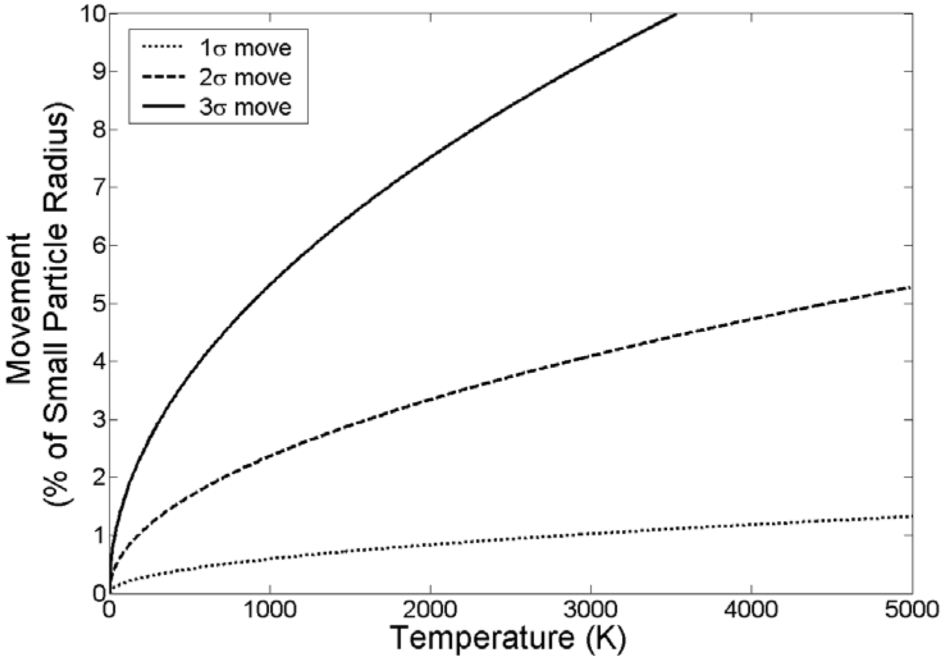

Figure 6.7: The maximum movements for one, two, and three standard deviations are shown versus temperature for an 8e-6 second time step.

With the selected time step of 8e-6, the larger particle would have an RMS displacement of approximately 2.7 diameters after 240,000 iterations at the estimated melting temperature. This number of iterations also allowed the RMS displacement to be approximately 1 at temperatures as low as 500 K.

It was hypothesized (as is explained below) that the melting temperature should scale with the average particle size. The time step for simulations of other particle sizes was therefore scaled as $a^2$ in order to keep the 3σ move at the melting point to approximately 10% of the particle radius.

## 6.5 Selection of Other Simulation Conditions

As is common with dynamics simulations, a cutoff radius was used, where the energy contribution of particles inside the radius was counted, while particles outside the radius were ignored. Neighbor lists were used to determine which particles have the potential to be inside the cutoff radius. The cutoff radius was placed where the interaction potential fell to 0.01kT at 3000 K. At this point, the potential was less than 1/3500 of its initial value. More information on cutoff radii and setting up neighbor lists can be found in Allen and Tildesley [112], which is an excellent reference for setting up any dynamics package.

In all the simulations, spheres interacted under the Yukawa pair-wise potential when not in contact. However, if particles were found to be overlapping, a force sufficient to move them apart twice their overlap was applied. This effectively simulates a rebound of each particle off of each other corresponding to the overlap distance.

## 6.6 Melting Behavior of Ionic Colloidal Crystals

Brownian dynamics simulation were conducted on several systems to determine the melting points of ICCs, as well as to learn about the nucleation behavior of these materials. Several factors must be considered when studying melting behavior through simulation in order to prevent anomalous results. These include kinetic effects on melting, such as nucleation of the crystalline or liquid phases, size effects due to limited simulation size, as well as numerical effects that can impact the results.

It is essential to separate kinetic effects from thermodynamic effects. If a temperature sweep were simulated on a crystalline system, changes in energy will be observed that are indicative of melting. However, these effects will be dependant on the temperature sweep rate due to the kinetic lag of the melting event. Furthermore, holding a crystalline system at the melting point would show little change in the state of the system. This is because there is no driving force for melting as the free energies of the liquid and crystalline phases are equal at the melting point. Melting behavior is therefore best observed with temperature holds further from the melting point.

Kinetic effects also contribute to the rarity of nucleation events (i.e. the crystalline phase from a liquid or the liquid phase from a crystalline surface). Nucleation of either phase is difficult to capture in dynamics simulations due to their low probability. These kinetic effects can be mitigated by starting with an initial condition that contains both the liquid and crystalline phases.

For reasons discussed in Section 6.3, periodic boundary conditions were not used in these simulations. Due to computational expense, systems of millions of particles, which could approximate bulk materials, are difficult to simulate. However, when the number of particles in a system becomes small, the system size has an effect on melting behavior. The suppression of melting point with finite system size, shown in Equation 6.30, is well studied for nanoparticle systems [113, 114]. Thus, in order to determine the bulk melting point, several systems of different sizes must be tested and either fit to Equation 6.30 or used to assure that the melting point is at its limiting value.

$$T_{melt,cluster} = T_{melt,bulk} \frac{r - C}{r} \tag{6.30}$$

There is a wide variety of numerical effects possible, but the largest effect can be due to the discretization of time. These effects can be mitigated through the selection of an appropriate time step as was discussed in Section 6.4.3 and 6.4.4.

## 6.6.1 Melting Simulation Setup

For Brownian dynamics studies of ICC melting, an *NVT* ensemble was chosen. The volume was selected to allow for melting of the initial condition, while still confining the particles and allowing them to return to the crystal within the simulation time if thermodynamically desirable. An initial condition of a perfect crystalline cluster was created in the center of the constant volume box where the particles occupied 33% of the volume. The temperature was raised to 14000 K to allow the crystal to melt. Melting was continued until only approximately 1/9 of the particles remained in the crystal. The resulting initial condition was then cooled to 5000K and annealed. Four system sizes were prepared in this way: 4096, 8000, 17576, and 32768 particles.

Simulations of the rocksalt structure were conducted for four particle size pairs with the four system sizes mentioned above. The particle sizes were varied as a percentage of the largest size pair of 1.58 μm and 0.76 μm, which were chosen to mimic the potential experimental system mentioned in Section 6.5. Salt concentrations were fixed to keep the screening ratio (Λ) constant at a value of 2.38, which is also believed to be close to the potential experimental system. For all simulations, the wall lengths were varied to maintain 33 volume percent of colloids. The time step was varied with particle size as was discussed in Section 6.4.4. This keeps the diffusivity at a constant value relative to the size of the particle and estimated melting temperature.

## 6.6.2 Bond-Angle Distribution Function

The bond-angle distribution function (BADF) [115, 116] was used to evaluate crystallinity in the simulation. The BADF compares the cosines of the bond-angles present in a perfect crystalline reference to those present within the simulation system. The bond-angle distribution is fit with Legendre polynomials, and the overlap between those coefficients and the coefficients of the perfect state is computed, giving a single value. For these simulations, a value between approximately 0.9 and 1.0 corresponded to a perfect crystalline state. Alternatively, the liquid state had values that ranged from approximately 0.6 to 0.8. Surface states between the liquid and solid were between 0.8 and 0.9.

During the tests, the initial conditions were held at various temperatures for one hundred thousand iterations. The changes in the size of the crystalline region were determined using the BADF, allowing the melting or crystallization rate at that temperature to be determined. These rates were then plotted with their corresponding temperatures, and the point of zero change was interpolated, giving the melting point for that system. Figure 6.8 illustrates the BADF values for a cross-section through the 32768 particle initial condition and the results after two temperature holds.

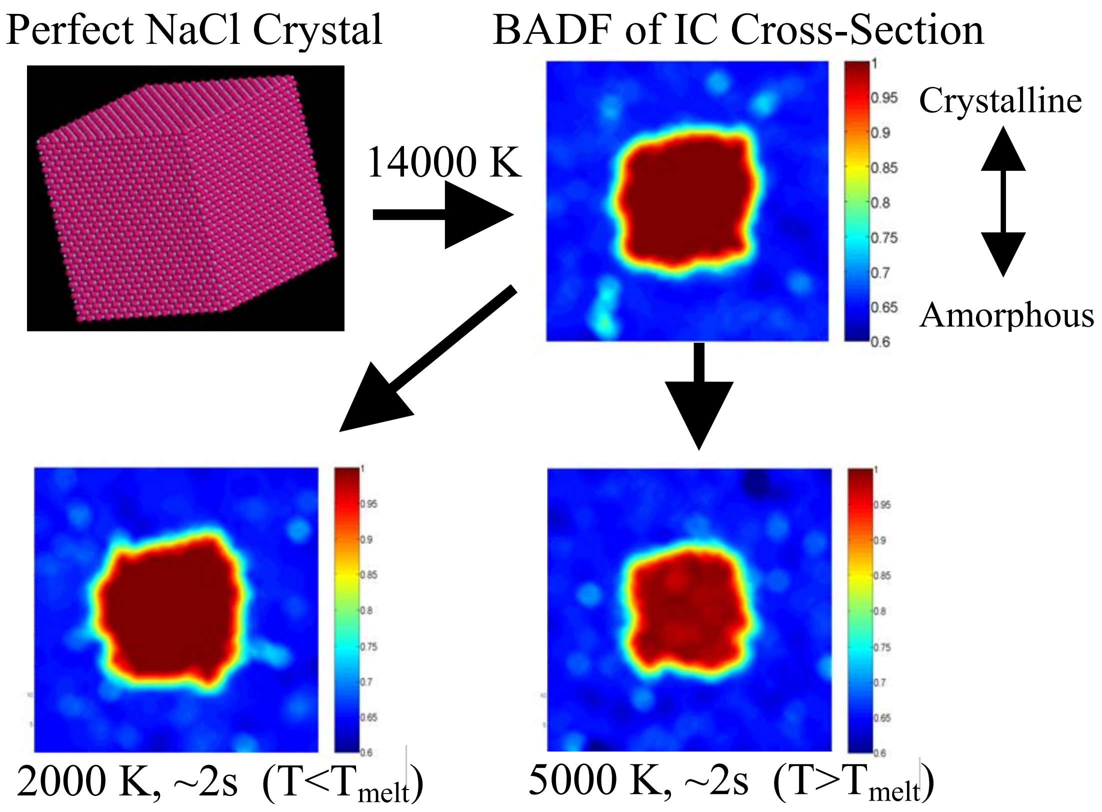

Figure 6.8: An example system is shown after melting at 14000 K and annealing. Melting was conducted until ~1/9 of the system remained crystalline. After melting, annealing was conducted at various temperature. Shown are two cases, with one above and one below the melting point.

### 6.6.3 Simulation Results

Every 2000 iterations, the percentage of particles in the crystal (determined by a BADF value between 0.9 and 1.0) was calculated. A plot of this crystalline percentage versus simulation time was fit with a linear function to determine whether the crystal was increasing or decreasing at that temperature. Figure 6.9 illustrates these results for all temperatures tested with the 32768 particle full-size (1.58 μm/0.76 μm) case. As the temperature increased, the rate of crystal growth decreased and eventually became negative. Where the rate is equal to zero, there is no driving force for melting or crystallization. This is the thermodynamic definition of the melting point [117].

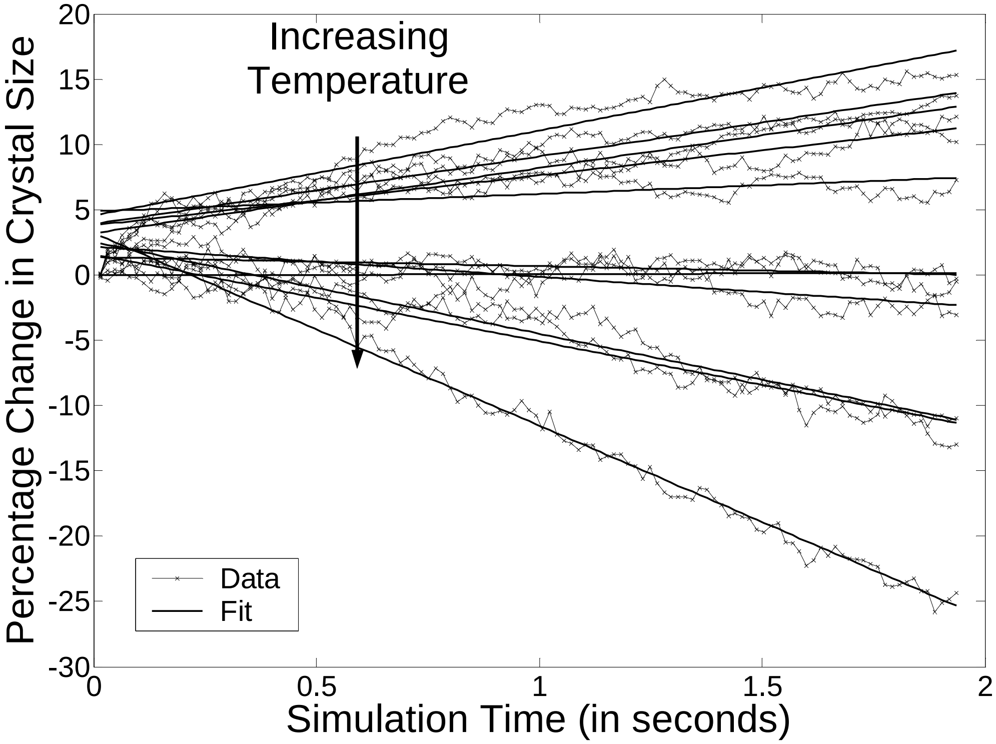

Figure 6.9: The percentage change in crystal size after constant temperature holds is plotted for a 32768-particle system of 1.58 μm silica and 0.76 μm polystyrene functionalized with amidine at a variety of temperatures. Note that as temperature increases, the crystal growth rate slows and then becomes negative. Where the slope is equal to zero, the system has no driving force to melt or grow. This is the melting point.

The slopes from the crystal growth fits were interpolated with a linear function to determine the intercept. Anomalous points occurred at high temperatures for the 4096 particle system due to complete melting of the crystal during the simulation time. These points decrease the slope of the fit artificially and were therefore removed before fitting. Figures 6.10 through 6.13 show the melting point determination for each simulation system.

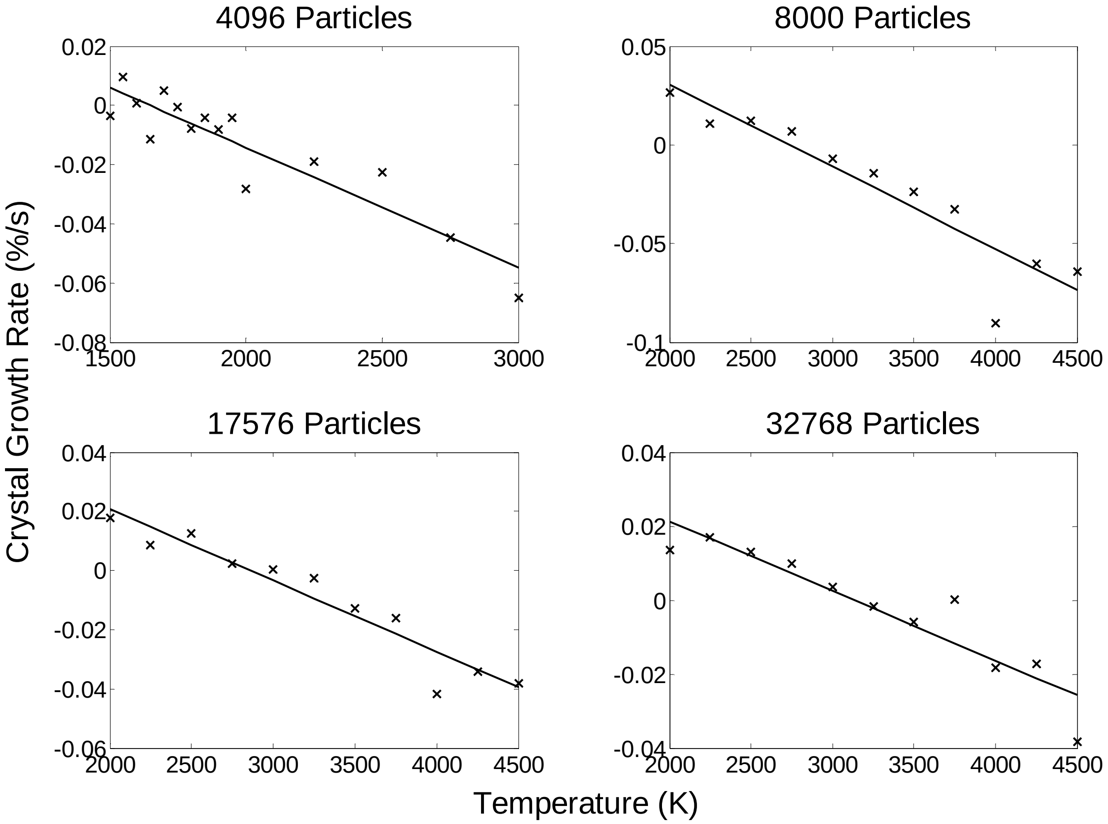

Figure 6.10: The crystal growth rate is plotted versus temperature for the 1.58 μm silica ($SiO_2$) and 0.76 μm polystyrene functionalized with amidine (PSA) system. The system size was varied from 4096 to 32768 particles. Only approximately 1/9 of these particles were present in the initial crystal. Note that the melting point increases with system size.

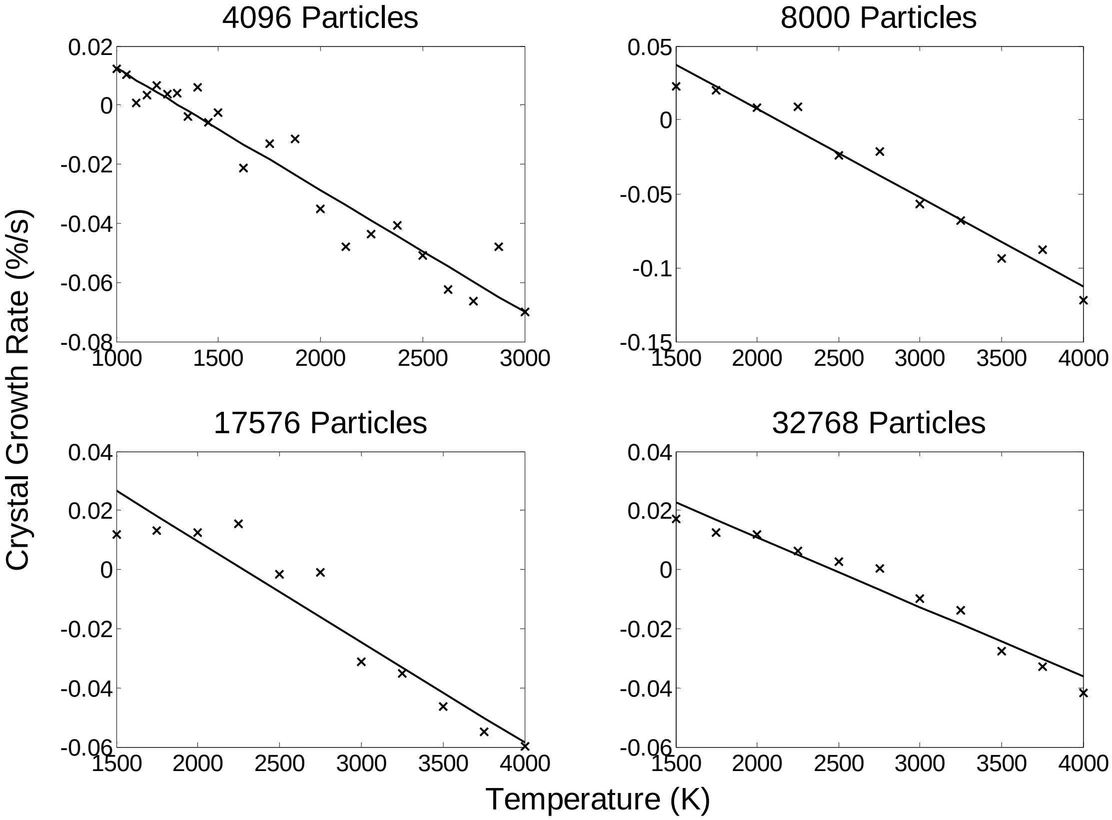

Figure 6.11: The crystal growth rate is plotted versus temperature for the 80% size system (1.264 μm $SiO_2$ and 0.608 μm PSA).

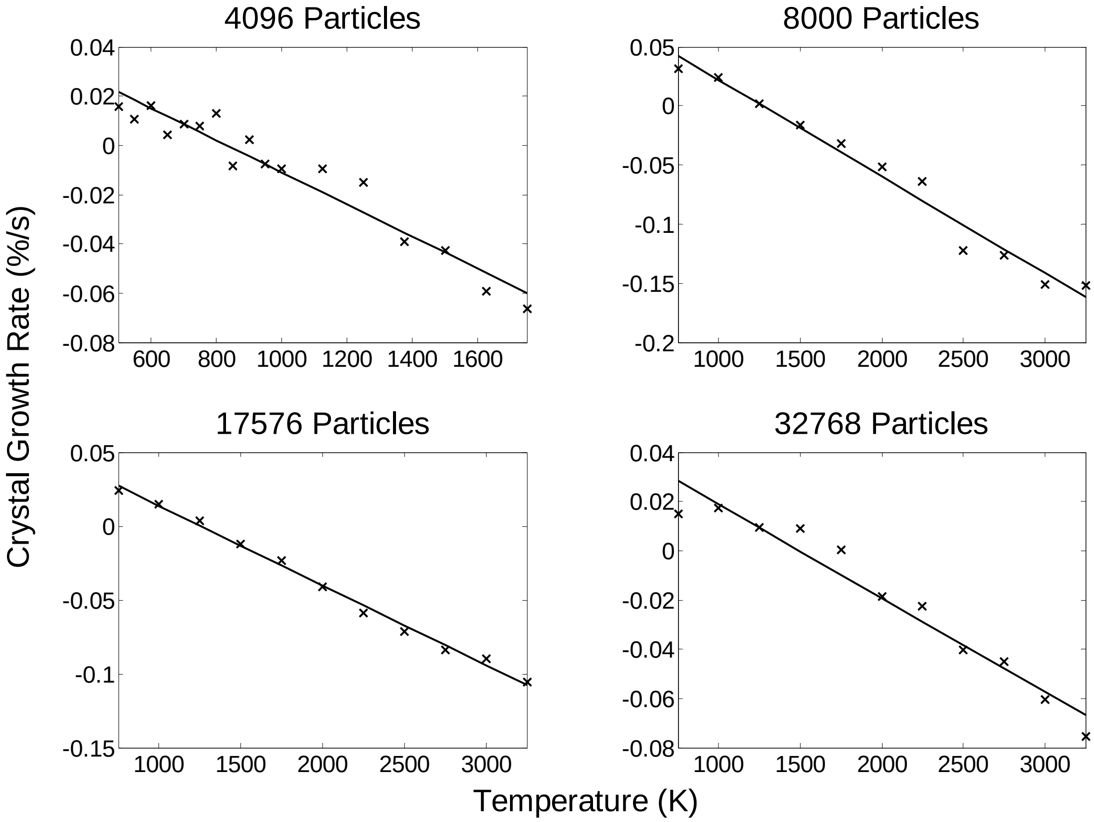

Figure 6.12: The crystal growth rate is plotted versus temperature for the 50% size system (0.79 μm $SiO_2$ and 0.38 μm PSA).

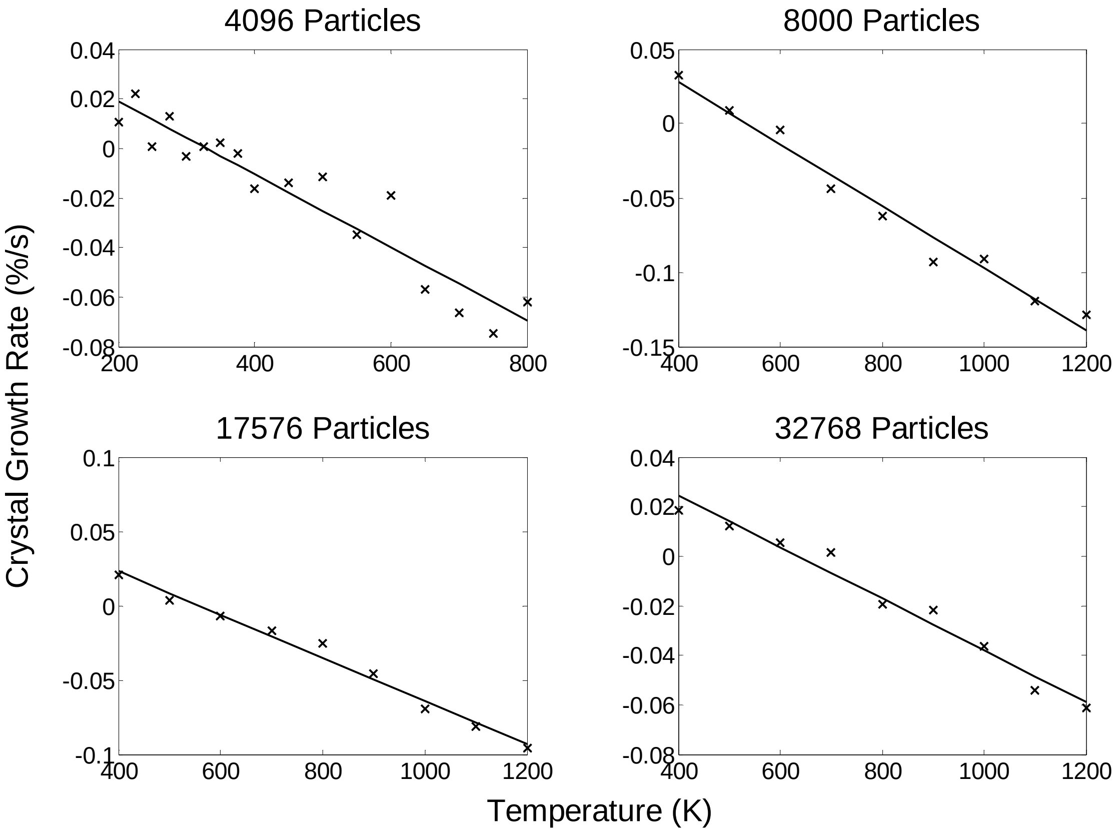

Figure 6.13: The crystal growth rate is plotted versus temperature for the 20% size system (0.316 μm $SiO_2$ and 0.152 μm PSA).

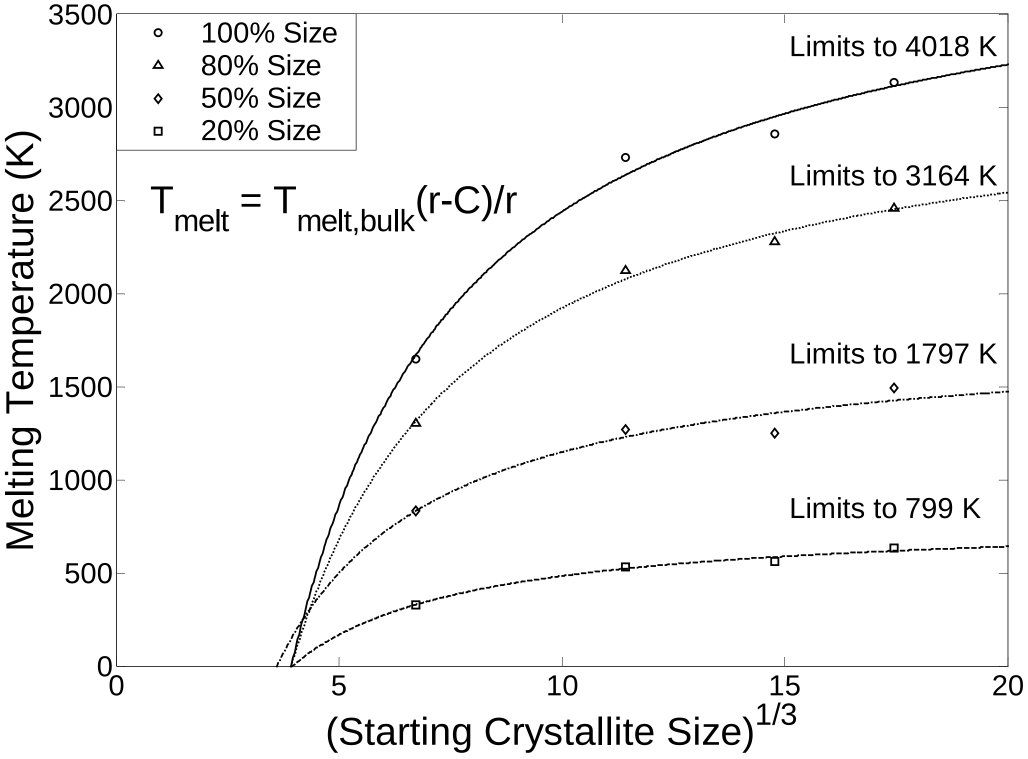

Figure 6.14: The fits of the simulation data to the Equation 5.28, which gives the dependence of melting point on crystallite size, are shown for the four particle size pairs tested. All four systems converge to the same 0 K critical nucleus radius and the bulk melting points scale roughly with particle size.

Figure 6.14 shows the melting point results for each system. These results are fit with Equation 6.30 to determine the bulk melting point and the critical nucleus radius at 0K, which is given by the constant *C*. Below this critical nucleus radius, no crystallite is stable at any temperature. *r* is defined as the cube root of the cluster size, which is the number of particles in the crystallite at the start of the simulation.

Figure 6.14 shows that the melting point scales linearly with a scaling of the particle sizes (i.e. if the particle sizes are both doubled, the melting point is also doubled). In Figure 6.15, the melting point is again plotted, with the data from Figure 6.14 rescaled by dividing by the particle sizes. The resulting data falls onto a master curve, which can also be fit with Equation 6.30. Likewise, the bulk melting points from Figure 6.14 can simply be plotted versus particle size and fit with a linear equation. Both cases give a similar bulk melting point for the full-size system of approximately 3900 K.

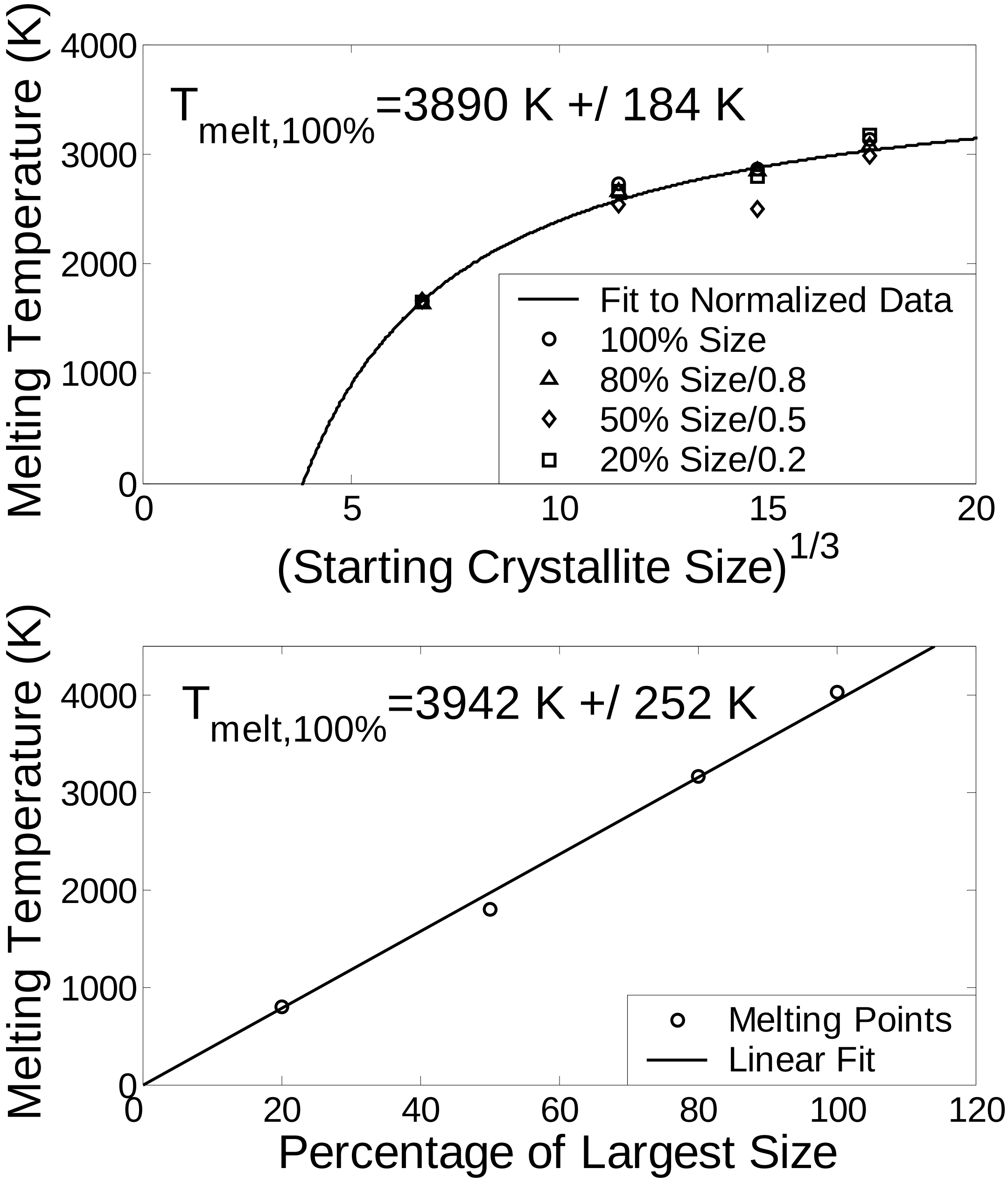

Figure 6.15: Two methods of determining the bulk melting point of the full-size system are shown. The first normalizes the data from Figure 6.14 by dividing by the particle size and refitting to Equation 6.30. The second shows a linear fit to the individual system bulk melting points versus the particle size. Both of these results can be used to evaluate the melting point of any ICC system. The melting point for the full-size system is found to be approximately 3900 K.

## 6.8 Discussion of Simulation Results

In the previous section, the melting point was shown to scale linearly with a scaling of the particle sizes. This result is consistent with a melting point that scales as the crystalline energy. The crystalline energy is defined as the Madelung sum multiplied by the individual bond strength.

$$T_{melt} \propto U_{crystal} = M_{sum} U_{bond} \tag{6.31}$$

$$U_{crystal} = M_{sum} 4\pi\varepsilon_0 \varepsilon_r \psi_{s,1} \psi_{s,2} \frac{a_1 a_2}{a_1 + a_2} \tag{6.32}$$

From Equation 6.32, it is clear that if the sizes of the particles are both scaled by some factor, then the crystalline energy also scales by that factor. For the Λ and *Q* values tested here, the Madelung sum of the rocksalt structure is determined to be 3.65 via the methods discussed in Chapter 4. The results of the previous section allow the constant of proportionality in Equation 6.31 to be obtained. This relationship can then be used to determine the melting point of other ICC systems.

$$T_{melt} = -6.91 \cdot 10^{20} \left( K/J \right) \cdot U_{crystal} = -6.91 \cdot 10^{20} \left( K/J \right) \cdot M_{sum} 4\pi\varepsilon_0 \varepsilon_r \psi_{s,1} \psi_{s,2} \frac{a_1 a_2}{a_1 + a_2} \tag{6.33}$$

The result in Equation 6.33 can be compared to similar coefficients for atomic ionic materials comparing lattice energies to melting points. While atomic ionic materials have other energetic terms beyond the Madelung energy, the correlation constants for ICCs at zero ionic strength should be similar. Table 6.1 shows several correlation constants for 1:1 ionic materials. The value of the constant is dependant on the free energy of the liquid structure relative to that of the crystal. The correlation constant between atomic systems and the ICCs simulated with Brownian dynamics is strikingly similar. This is actually surprising in the context of Chapter 4, where a change in melting behavior is expected with increasing ionic strength. The internal energy difference between the liquid and solid states might be similar, but the entropy of a colloidal liquid at high ionic strengths is expected to be much lower than the atomic liquid. Therefore, a much higher temperature would be required before the free energy of the two colloidal structures becomes comparable, resulting in a higher melting point.

Table 6.1: The lattice energy of various ionic systems is compared to its melting point. The calculated ICC conversion constant is very similar to that of the atomic case despite all of the approximations present in the Brownian dynamics.

| Material | Lattice Parameter (nm) | Structure | Madelung Sum | Electrostatic (kJ/mol) | Lattice Energy (kJ/mol) | Melting Point | Boiling Point | MP Conversion kJ/(mol-K) | BP Conversion kJ/(mol-K) |
|---|---|---|---|---|---|---|---|---|---|
| LiF | 0.201 | NaCl | 1.748 | 1208 | 1021 | 1121 | 1954 | 0.911 | 0.522 |
| LiCl | 0.257 | NaCl | 1.748 | 945 | 837 | 886 | 1633 | 0.944 | 0.512 |
| LiBr | 0.275 | NaCl | 1.748 | 883 | 791 | 820 | 1538 | 0.964 | 0.514 |
| LiI | 0.300 | NaCl | 1.748 | 810 | 736 | 742 | 1447 | 0.992 | 0.509 |
| NaF | 0.231 | NaCl | 1.748 | 1051 | 900 | 1269 | 1977 | 0.709 | 0.455 |
| NaCl | 0.281 | NaCl | 1.748 | 864 | 770 | 1074 | 1738 | 0.717 | 0.443 |
| NaBr | 0.298 | NaCl | 1.748 | 815 | 736 | 1028 | 1663 | 0.716 | 0.443 |
| NaI | 0.323 | NaCl | 1.748 | 752 | 686 | 933 | 1577 | 0.735 | 0.435 |
| KF | 0.266 | NaCl | 1.748 | 913 | 807 | 1133 | 1778 | 0.713 | 0.454 |
| KCl | 0.314 | NaCl | 1.748 | 773 | 703 | 1044 | 1710 | 0.673 | 0.411 |
| KBr | 0.329 | NaCl | 1.748 | 738 | 674 | 1007 | 1708 | 0.669 | 0.394 |
| KI | 0.353 | NaCl | 1.748 | 688 | 636 | 954 | 1618 | 0.667 | 0.393 |
| RbF | 0.282 | NaCl | 1.748 | 861 | 766 | 1106 | 1683 | 0.692 | 0.455 |
| RbCl | 0.327 | NaCl | 1.748 | 743 | 678 | 988 | 1663 | 0.686 | 0.408 |
| RbBr | 0.343 | NaCl | 1.748 | 708 | 653 | 955 | 1619 | 0.683 | 0.403 |
| RbI | 0.366 | NaCl | 1.748 | 664 | 619 | 915 | 1577 | 0.677 | 0.393 |
| CsF | 0.300 | NaCl | 1.748 | 810 | 736 | 976 | 1504 | 0.754 | 0.490 |
| CsCl | 0.356 | CsCl | 1.763 | 688 | 640 | 919 | 1573 | 0.697 | 0.407 |
| CsBr | 0.371 | CsCl | 1.763 | 660 | 628 | 909 | 1573 | 0.690 | 0.399 |
| CsI | 0.395 | CsCl | 1.763 | 620 | 598 | 894 | 1553 | 0.669 | 0.385 |
| MgO | 0.210 | NaCl | 1.748 | 4626 | 3933 | 3073 | 3873 | 1.280 | 1.015 |
| CaO | 0.240 | NaCl | 1.763 | 4082 | 3523 | 3173 | 3773 | 1.110 | 0.934 |
| SrO | 0.257 | NaCl | 1.763 | 3812 | 3309 | 2703 |  | 1.224 |  |
| BaO | 0.276 | NaCl | 1.763 | 3550 | 3125 | 2246 | 3361 | 1.392 | 0.930 |
| MgS | 0.260 | NaCl | 1.748 | 3736 | 3255 | 3099 |  | 1.050 |  |
| CaS | 0.284 | NaCl | 1.763 | 3450 | 3021 | 2798 |  | 1.080 |  |
| SrS | 0.294 | NaCl | 1.763 | 3333 | 2874 | 2500 |  | 1.150 |  |
| BaS | 0.318 | NaCl | 1.763 | 3081 | 2745 | 2503 |  | 1.097 |  |
|  |  |  |  |  |  |  | Average | **0.869** | 0.509 |
|  |  |  |  |  |  |  | StDev | 0.224 | 0.184 |
| ICC NaCl | 1170 | NaCl | 3.65 | 3391 | 3391 | 3890 |  | **0.872** |  |

The similarity between the correlation constants for the simulated ICC systems and the atomic ionic systems makes the results of these simulations questionable despite the great lengths taken to assure its accuracy. A potential source of the discrepancy can be found by going back to Equation 6.15 and grouping the time step and viscosity terms.

$$\Delta r = \sum_{j \neq i} F_{ij} \left( \frac{\Delta t}{\beta_i} \right) + \langle A \rangle \sqrt{6kT} \left( \frac{\Delta t}{\beta_i} \right)^{1/2} \tag{6.34}$$

Written this way, the viscosity simply scales the time-step. This should be expected as the thermodynamic results should not be impacted by either the viscosity or the time step. However, upon a closer examination, this scaled time step does have an impact on the thermodynamics. The impact of interparticle interactions scales linearly with the combined parameter, however the impact of thermal fluctuations scales as the square root of the parameter. Because of this, in effect, dividing the time step (or increasing the viscosity) by a factor of four should double the impact of thermal forces relative to the interparticle forces.

Despite its short-comings, some insight can still be gleaned from particle dynamics if temperatures are scaled appropriately. For example, some information can be obtained about the nucleation behavior of ICCs from these results. By solving Equation 6.30 for the crystallite size versus the melting point of that size, the critical nucleus size as a function of temperature (given as a percentage of the bulk melting point) can be determined. The critical nucleus size at 0 K is found to be approximately 58 particles. Figure 6.16 shows the estimated critical nucleus size at a variety of temperatures. The high critical nucleus sizes observed from these simulations was unexpected and may be an indication of why significant crystallization is not observed experimentally. Note that Figure 6.16 is identical for all particle systems simulated as the results are normalized to the melting point.

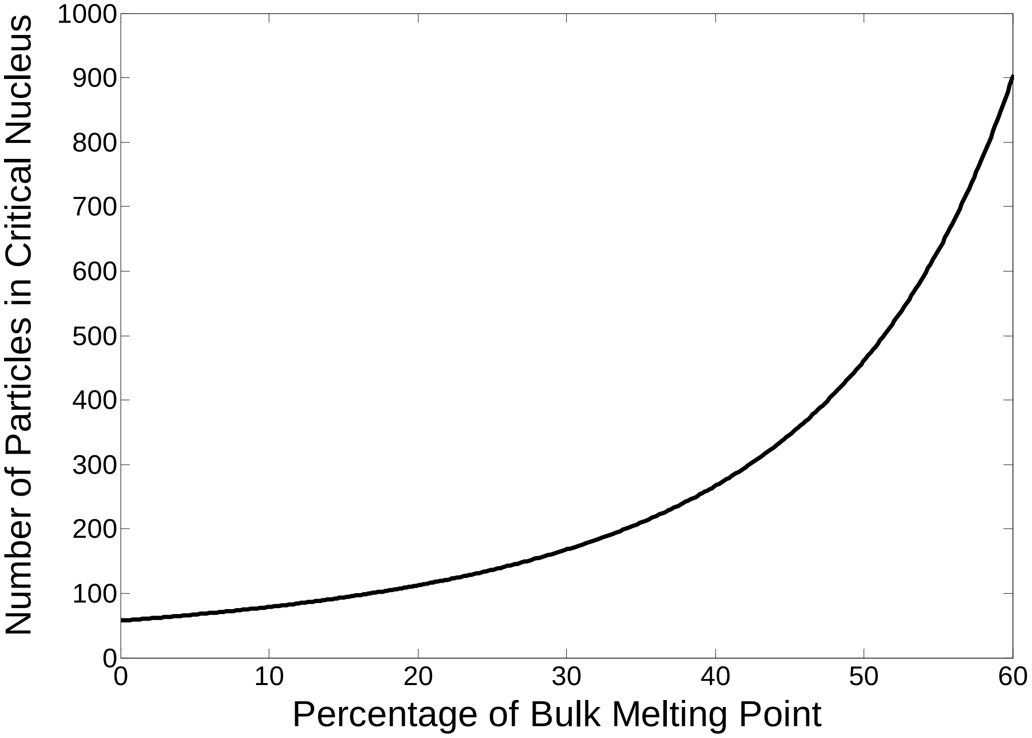

Figure 6.16: The critical nucleus size is plotted versus the temperature relative to the bulk melting point. Due to the large critical nucleus size at 0 K, a very large nucleus is required for even moderate temperatures, where sufficient mobility for crystallization would be expected.

## 6.9 Crystallization from a Disordered State

Brownian dynamics were also used to study the effect of various conditions on crystallization. As the simulation temperatures were maintained relative to the calculated Brownian dynamics melting temperature, the results can be interpreted as a percentage of the calculated melting point (~4000 K). In most cases, disordered structures were observed. In low volume fraction systems small clusters were observed with no longer range order. In high volume fraction systems, connecting gels were generally observed. However, two cases were identified where crystallization was greatly enhanced. The first case had a significantly increased particle density. The second case involved applying a strong gravitational force to the particles. This serves two purposes: it breaks up any gelation that forms and also serves to significantly increase the density of particles at the bottom of the simulation cell. Simulated gravitational forces reproducibly created ICC polycrystals from a variety of initial conditions and parameters.

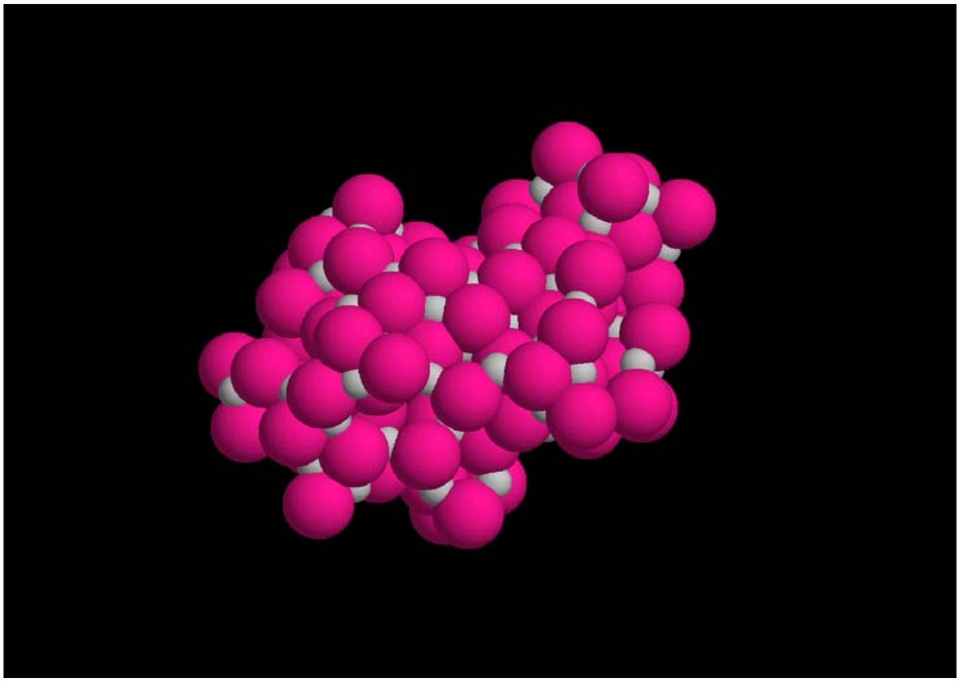

Figure 6.17: A disordered cluster is shown from one attempt at observing nucleation in an ionic colloidal liquid. Notice that some regions appear to have the rocksalt structure, but no long range order exists. This is similar to what is observed experimentally as is discussed in Chapter 5.

Figure 6.18 shows the crystal that resulted from a random initial condition where the particles occupied 50 volume percent. This system is identical to that used for melting point simulations. It therefore had an estimated melting point of 4000 K. The system was first held at 5000 K to allow rearrangement of the liquid, followed by a hold at 3000 K to allow nucleation and growth. Increasing the particle density effectively lowers the critical nucleus size as it decreases the interfacial energy between a crystal and the reference liquid. This is because a higher density liquid is energetically much closer to a crystal than a low density liquid or a gas. Thus, the lower interfacial energy decreases the nucleation barrier. The volume constraint on the system also greatly increases crystallization rates as it does not allow gel formation.

Similarly, Figure 6.19 shows crystallization that resulted from the addition of gravitational forces. In this example, 50 g are used on a system identical to that used for melting point studies. The initial condition is a random arrangement of particles at 15 volume percent. The box was tetragonal to allow more room for settling while maintaining a sufficient areal density perpendicular to the settling direction. If gravitational forces are too strong relative to the electrostatic forces, phase separation can occur. However, if sufficient force is added to break up any low density aggregates, crystallization is greatly enhanced.

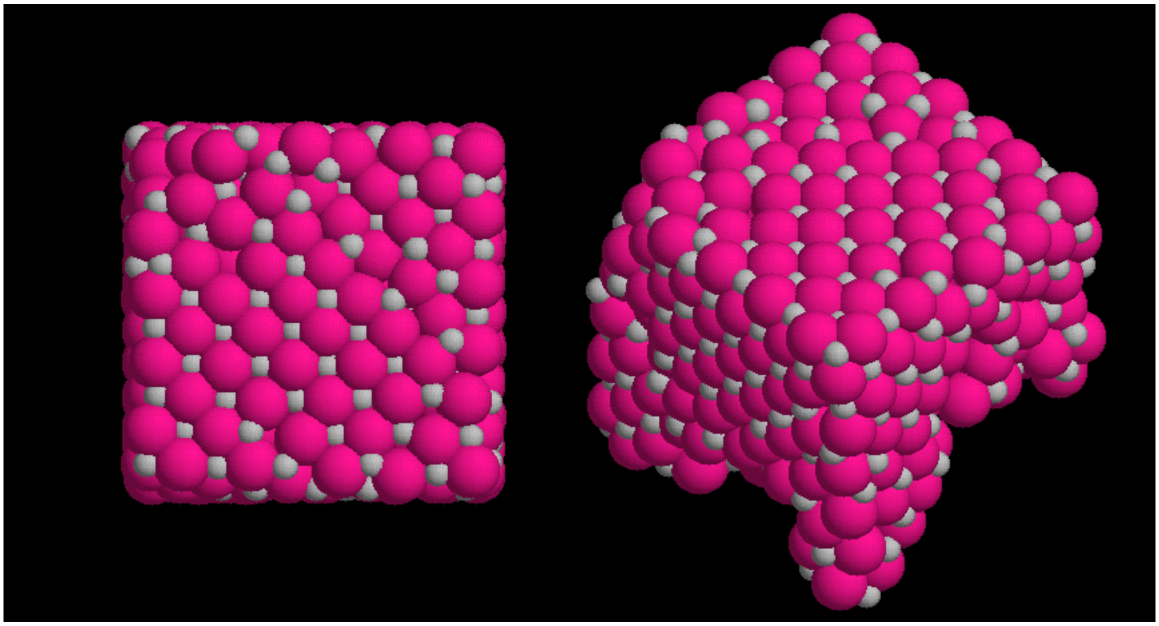

Figure 6.18: Crystallization is demonstrated from a random initial condition. A high volume fraction of particles (50%) greatly enhances crystallization. For low densities, crystallization is not commonly observed.

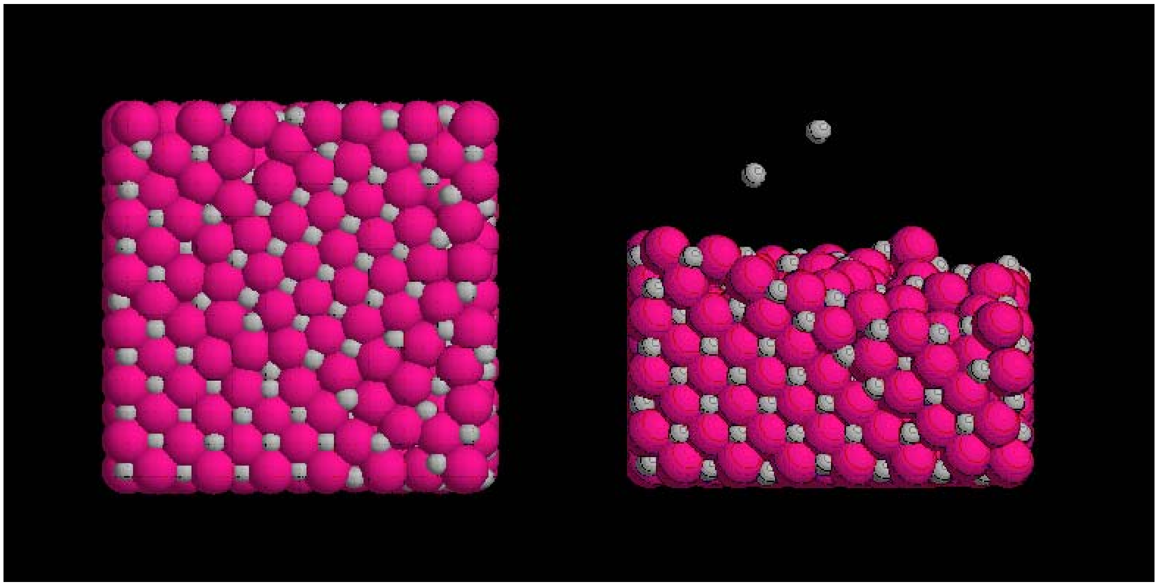

Figure 6.19: Crystallization is also enhanced through the addition of gravity. In this case 50 g's are added to a low density (15 volume percent) system.

# Chapter 7: Monte Carlo Simulations of ICCs

While Brownian dynamics methods are much more widely used to study colloidal behavior[1], Monte Carlo methods are more accurate as they involve many fewer approximations. Because of this, they can be very useful for simulating the thermodynamics of colloidal behavior. In Monte Carlo methods, random system changes are made and accepted or rejected according to predefined rules. The most common rule scheme is the Metropolis algorithm [118]. Under this algorithm, a change is always accepted if it results in a lower system energy, but it is only accepted with a Boltzmann probability if it causes the system energy to be raised. These acceptance rules satisfy the

---

[1] In a simple search on INSPEC, there are 27852 hits for either "particle dynamics" or "Brownian dynamics" (2066 by itself). However, "Monte Carlo" and "colloi*" only shows 384 articles. This illustrates the vast popularity of Brownian dynamics despite its short-comings. This does not correct for those who consider Brownian dynamics simulations a form of Monte Carlo because they incorporate random numbers. In actuality, standard Monte Carlo methods are very different.

conditions of a detailed balance, which requires that the number of transitions from state $A$ to state $B$ must equal the number of transitions from $B$ to $A$ for a many-bodied system in equilibrium. The book *Understanding Molecular Simulation* by Frenkel and Smit is recommended for further reading [119] on Monte Carlo simulations.

The internal energy in a colloidal system is given by the pair-wise summation of all the interaction energies in the system. Under the *NVT* ensemble, the energy change corresponding to the movement of one particle is simply the change in the interaction energy between all other particles in the system and that particle. For the *NVT* ensemble, the acceptance algorithm is given by Equations 7.1 and 7.2.

$$\Delta U_i < 0, \quad acc(A_i \to B_i) = 1 \tag{7.1}$$

$$\Delta U_i > 0, \quad acc(A_i \to B_i) = \exp\left( -\frac{\sum_{j \neq i} \Delta U_{ij}}{kT} \right) \tag{7.2}$$

The acceptance rules in Equation 7.1 and 7.2 are commonly expressed as given in Equation 7.3.

$$acc(A_i \to B_i) = \min\left( 1, \exp\left( -\frac{\sum_{j \neq i} \Delta U_{ij}}{kT} \right) \right) \tag{7.3}$$

Under the *NPT* ensemble, an acceptance rule must be created that accounts for the energy change due to a volumetric change. The volume change is implemented by altering the simulation size and scaling all particle positions by the appropriate ratio. As this expansion or contraction changes the interaction energies of all the particles with respect to one another, the energy change of all of the particles must be counted. The volume change is also done against an external pressure, making it necessary to account for $P\mathrm{d}V$ work. Therefore, the energy used in the acceptance rules is the Helmholtz free energy at constant pressure rather than the internal energy. An additional extra term must appear in the acceptance rules to correct the partition function for the volume changes. This term is dependant on the sampling rules and is given in Equation 7.4 for linear changes in volume ($V=V_0+\Delta V$).

$$acc(A \to B) = \min\left(1, \exp\left(\sum_{i}\sum_{j \neq i} \Delta U_{ij} + PdV - kTN \ln\left(\frac{V + dV}{V}\right)\right)\right) \qquad (7.4)$$

Clearly, the calculation required for this acceptance rule is much more computationally expensive than that needed for the acceptance rules in the *NVT* ensemble. However, it only needs to be done when a volumetric change occurs. When the trial change is just a single particle move, the system remains at a constant volume. In these cases, Equation 7.3 still governs the acceptance of the change. Therefore, a typical implementation of the *NPT* ensemble would involve a certain number of particle moves (commonly one move for every particle in the system) under the *NVT* acceptance rules, followed by an attempted volumetric change with the *NPT* acceptance rules.

Under Monte Carlo, changes should be made such that acceptance occurs approximately 50% of the time. Changes that are almost always accepted are too small to allow the system to equilibrate in a reasonable amount of time. On the other hand, if the change is rejected too frequently because it is too large, the system will also take a long time to reach equilibrium as very few moves will occur.

## 7.1 Simulation Setup

Simulations were conducted to verify the melting point results from Chapter 6 and thereby the ability of Brownian dynamics to accurately predict thermodynamic quantities. All systems were tested with periodic boundary conditions. The first system tested was a perfect crystal of 1000 particles and the second system was amorphous. To create the initial conditions for the second system, a large space was randomly filled with particles and then annealed. After annealing, more particles were added and the system was annealed again. This process was repeated until no more particles could be added. Finally, a long hold under *NPT* conditions was conducted at 3000 K to obtain a sample that had a stable volume. A stable volume was also achieved at 4000 K in this manner. All interactions were under a Yukawa-type potential with an infinite hard sphere repulsion at contact. The particles tested are 2 μm in diameter at 18.4 mV and 1 μm in diameter at -100 mV. The simulations were conducted at Λ=3, giving a charge ratio of one.

A zero pressure was chosen for the simulations. As was discussed in Chapter 6, the energy from the pressure due to unbound colloidal particles in the solution is negligible compared to electrostatic interactions. Because of this and the fact that any pressure selection would be arbitrary, a zero pressure was chosen for the $NPT$ simulations. As discussed in Frenkel and Smit [119], a zero pressure can be used for quick estimations of phase behavior as long as the time scale of the simulation is sufficiently small. The main concern with using zero pressure is that the system could expand infinitely since external pressure may be the only force present to stabilize the volume. However, in ICC simulations, a stable volume was always achieved with zero pressure due to the strong electrostatic interactions.

Once initial conditions were obtained, the systems were held at progressively higher temperatures and allowed to equilibrate. To hasten this step, the initial conditions were rescaled at each simulation temperature to be near the expected stable volume at that temperature. Each simulation was run for 100,000 moves of each particle and 100,000 volume changes. Several systems with slightly different volumes were simulated at each temperature. The volume of all systems at a given temperature tended toward a common value, which was interpolated to find the equilibrium volume and energy for a given temperature. Figure 7.1 shows the results and interpolation for the disordered system at 5000 K. In Figure 7.2, the internal energy variations of the same system are shown. The change in internal energy due to a change in the starting volume is extremely small compared to the energy change due to a variation in temperature.

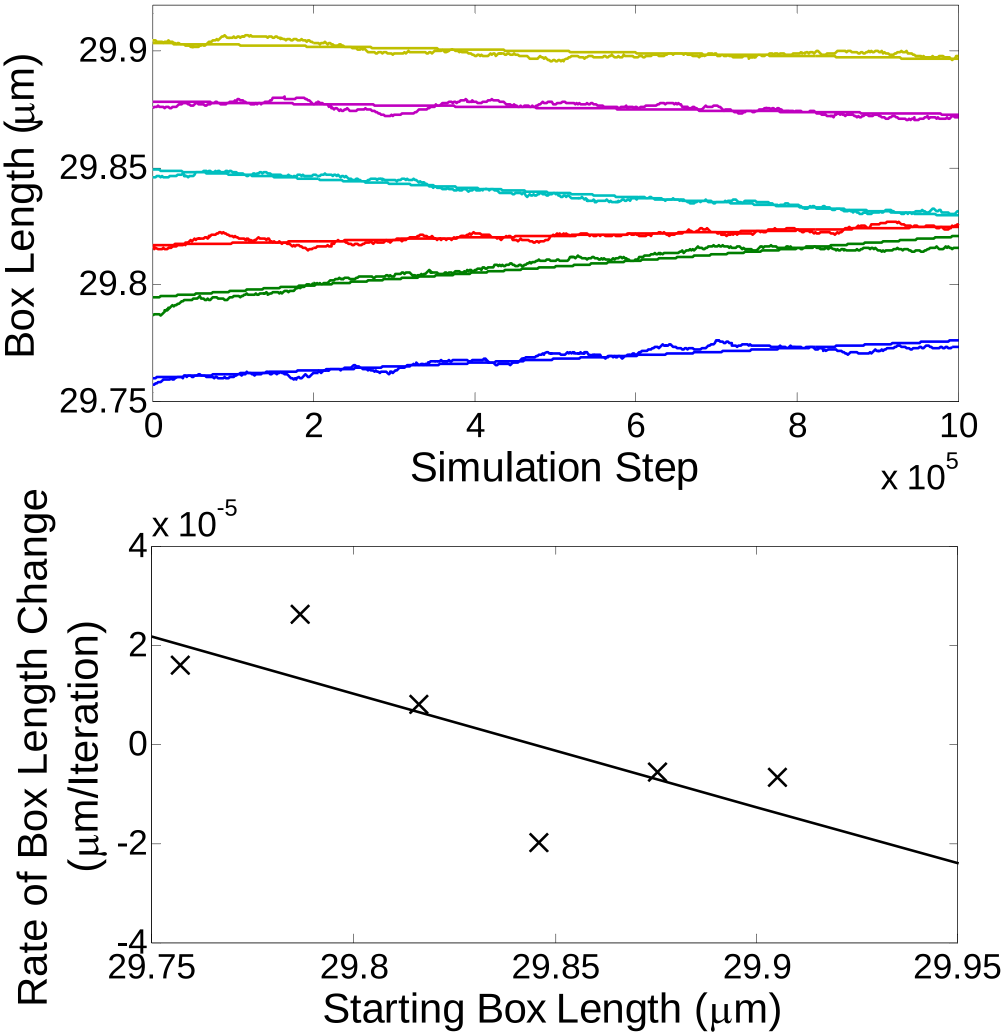

Figure 7.1: The size of the simulation box is shown for the disordered state at several starting box sizes. The temperature for this data was 5000 K. All simulations above a certain box size are decreasing in volume throughout the simulation, while all below that size are increasing. The data is fit to a line (bottom graph) to determine the equilibrium volume. Similar calculations were done at every temperature for both the crystal and the disordered state.

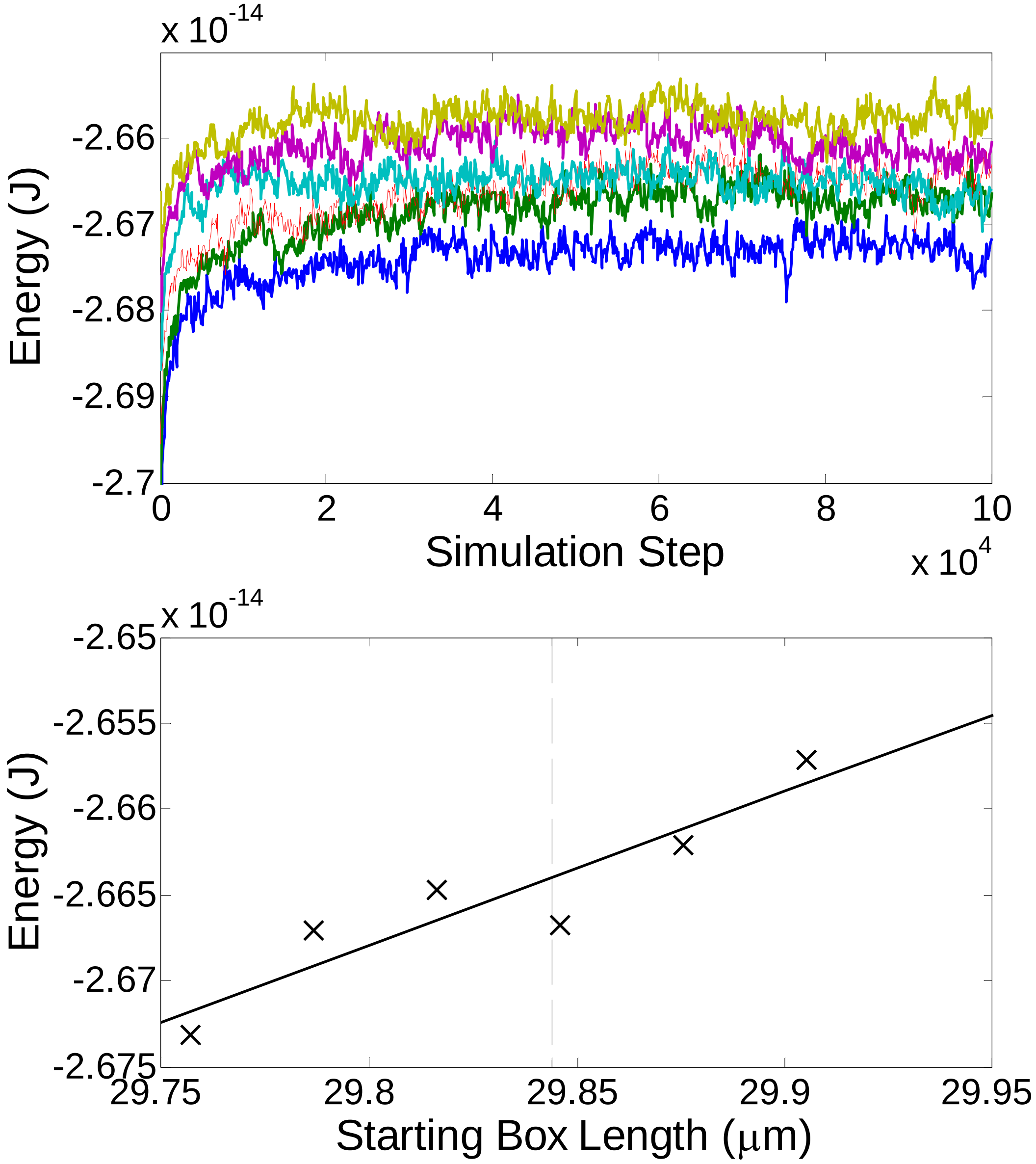

Figure 7.2: The internal energies of the systems from Figure 7.1 are plotted at various box sizes. The energy for a given box size is calculated by averaging over the last 50000 simulation steps. The dotted line in the bottom figure corresponds to the equilibrium volume determined in Figure 7.1. The scatter in energy data is small compared to energy changes with temperature, making the estimated energy from the linear fit only a slight correction to the total internal energy of the system at the equilibrium volume.

## 7.2 Simulation Results

The melting point was determined by calculating the free energy of both the liquid and crystalline states at each temperature and finding the point where they are equal. To do this, the entropy at each temperature needed to be calculated. For an *NPT* system, the entropy at a certain temperature is found by integrating the constant pressure heat capacity over temperature from zero to the temperature of interest.

$$S = \int_0^{T_1} \frac{C_P}{T}\,dT = \int_0^{T_1} \frac{\left.{}^{\partial H}\!/\!{}_{\partial T}\right|_P}{T}\,dT \tag{7.5}$$

For a constant heat capacity, this integral diverges at $T$=0. However, as the entropy should be zero at 0 K, the heat capacity must also tend toward zero at 0 K. To accommodate this, the integration is taken from 1 K to the desired temperature.

$$S = C_P \ln(T)\Big|_1^{T_1} \tag{7.6}$$

The internal energy (which is equal to the enthalpy in this case) for both systems was approximately linear with temperature to 6000 K, allowing Equation 7.6 to be used with little error. When the temperature became nonlinear, the entropy was instead obtained through Equation 7.5.

The equilibrium free volume at every tested temperature is shown for both systems in Figure 7.3. A discontinuity in the slope of the free volume is observed at approximately 7000 K. This may correspond to a glass transition temperature. Similarly, Figure 7.4 shows the internal energy of both systems at each temperature. Again, the crystalline energy shows a smooth increase, while the energy of the disordered state appears discontinuous.

Once the entropy is calculated, the free energy is found using Equation 7.7. Figures 7.5 and 7.6 show the free energy for both the crystalline and disordered states, respectively, with the internal energy and entropy terms plotted separately for comparison.

$$G = U + \overset{\text{0 for this system}}{\cancel{PV}} - TS = U - TS \tag{7.7}$$

The free energy for both systems is plotted together in Figure 7.7. The point where the free energy of the liquid equals that of the crystal is the melting point (8986 K for this system).

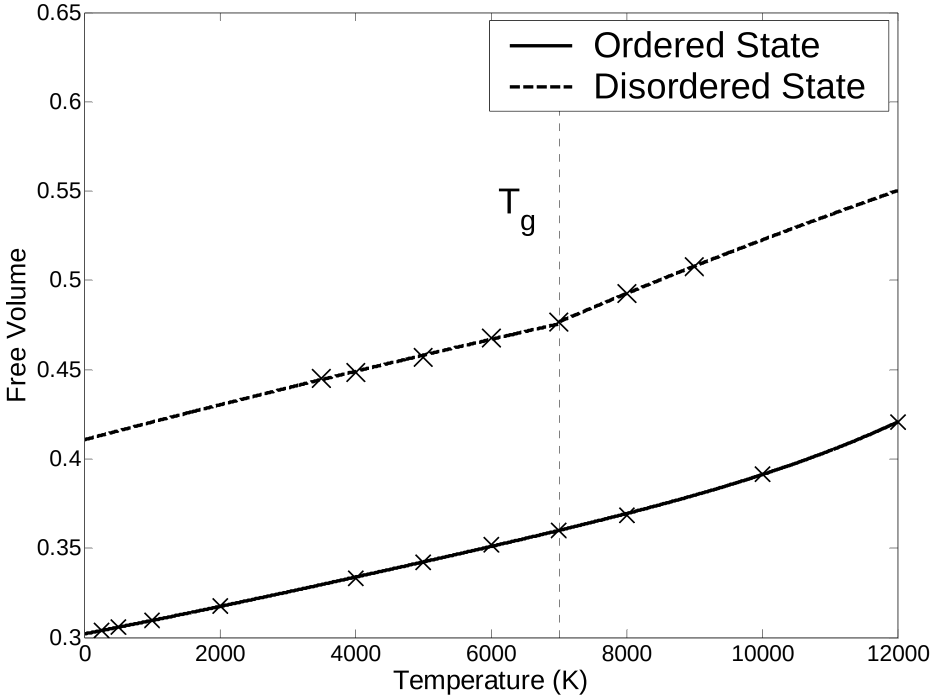

Figure 7.3: The free volume for every tested temperature is shown for both systems. While the ordered state appears to vary smoothly, the disordered state has a discontinuity in the slope at 6960 K. This discontinuity is believed to correspond to the glass transition temperature of the system for a very slow cooling rate.

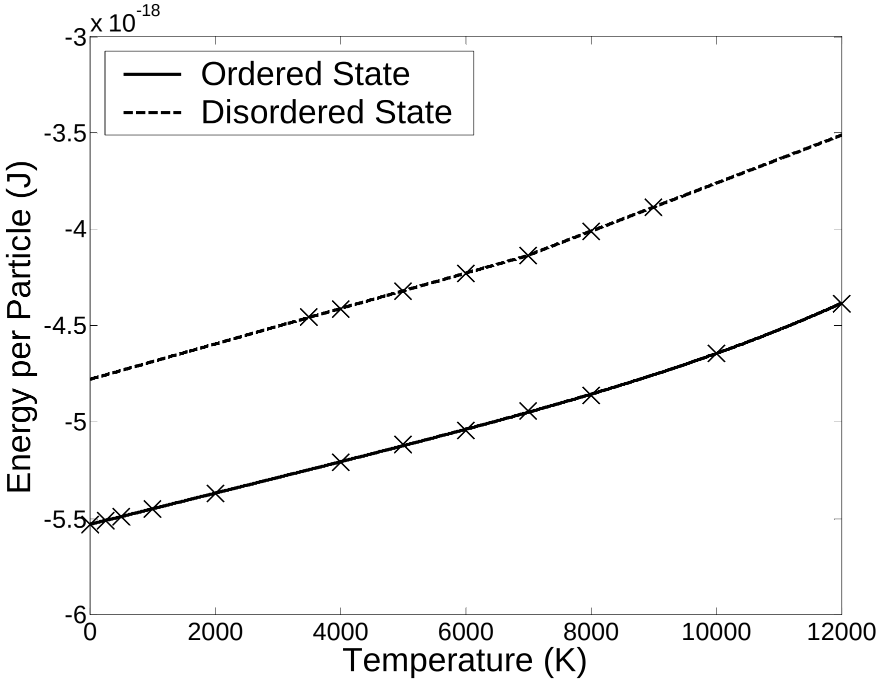

Figure 7.4: The internal energy versus temperature is shown for both tested systems from 0 to 12000 K.

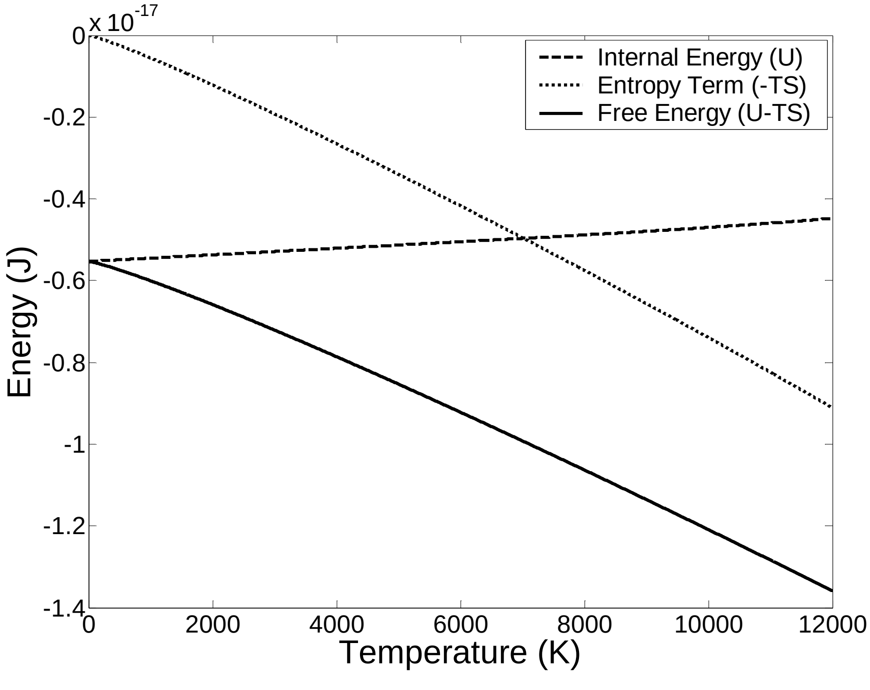

Figure 7.5: The free energy of the crystalline state is shown with the internal energy and entropy contributions.

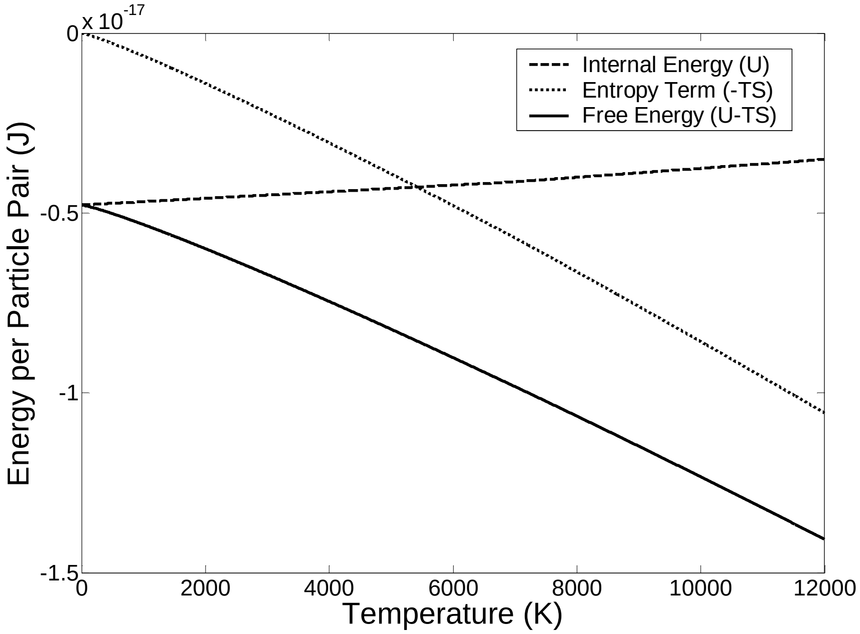

Figure 7.6: The free energy of the disordered state is shown with the internal energy and entropy contributions. While the internal energy is initially lower for the ordered state above, the entropy contribution of the disordered state is larger than that for the ordered state, as would be expected, resulting in a larger slope for the free energy.

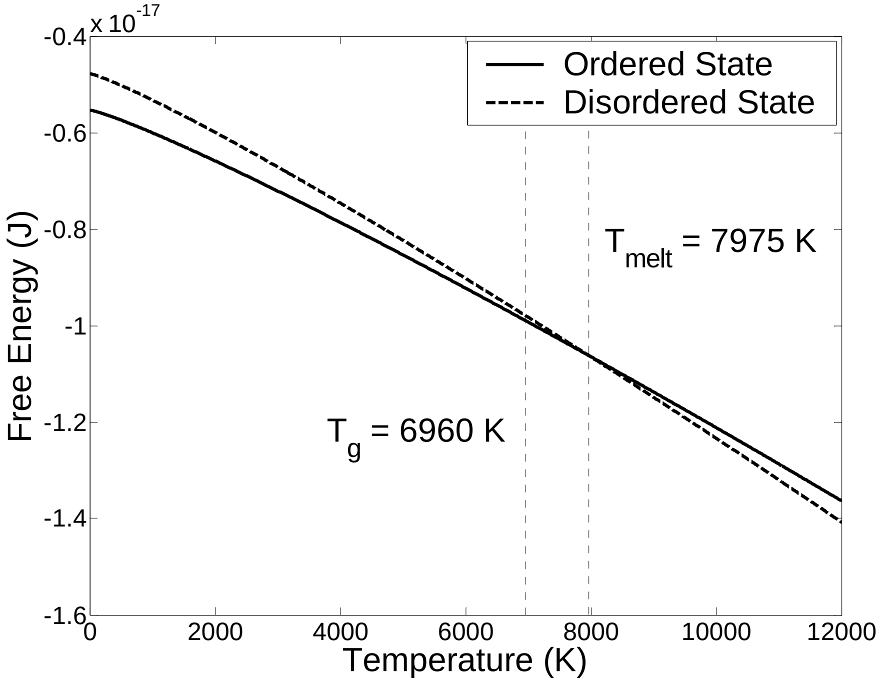

Figure 7.7: The free energy for both states is plotted versus temperature. The melting point is defined as the point where the free energy curves are equal. Melting occurs at 7975 K for this system. A narrow crystallization window is available between the glass transition point and the melting temperature.

## 7.3 Discussion of Simulation Results

The melting temperature can be compared to the bond strength of this system in a manner similar to that presented in Chapter 6. The bond strength is calculated to be 3334 kJ/mol, very similar to the Brownian dynamics system studied in Chapter 6. However, the correlation constant is now 0.418. Note that this is actually closer to the boiling point comparison for atomic systems. This could indicate that even at a $\Lambda$ value of 3, the potential well is already very steep, only allowing movement near the boiling point of an ICC liquid. Because the melting point of an ICC is expected to increase with ionic strength due to the markedly decreased entropy, the fact that these simulations would predict a much higher melting point than is observed in atomic systems is not unexpected.

A glass transition temperature is observed at 6960 K for this system, which is at approximately 87% of the calculated melting point. This is evidenced by a discontinuity in the slope of the free volume curve. Experimentally, it is important to assure the system has enough mobility to allow crystallization. These results provide an estimate of when crystallization may occur and when glassification would be expected instead. The glass transition temperature is expected to become closer to the melting point as the ionic strength is increasesd.

These Monte Carlo results show that despite the great lengths taken to assure the accuracy of the Brownian dynamics simulations, BD still does not accurately predict a basic thermodynamic property such as the melting point. However, the Brownian dynamics results can still be useful after the temperatures are recalibrated with the Monte Carlo results, in this case multiplying by approximately two. The correction to Equation 6.31 for the melting point correlation with system parameters is given in Equation 7.8.

$$T_{melt} = -1.44 \cdot 10^{21} \left( {}^{K}\!/_{J} \right) \cdot U_{crystal} = -1.44 \cdot 10^{21} \left( {}^{K}\!/_{J} \right) \cdot M_{sum} 4\pi\varepsilon_0 \varepsilon_r \psi_{s,1} \psi_{s,2} \frac{a_1 a_2}{a_1 + a_2} \qquad (7.8)$$

Combining the results of both simulations, several important behaviors of ICCs are observed. From the Brownian dynamics simulations, the melting point is shown to scale with the bond strength, and the critical nucleus size of an ICC system is estimated to be large. Furthermore, through densification or the addition of gravity, the nucleation can be greatly facilitated. The Monte Carlo simulations give a means to scale the temperature of the Brownian studies. They also reveal a glass transition temperature, which indicates that a system should not be undercooled more than 20% of its melting point if substantial rearrangement is desired. Of course this value will change with ionic strength, but it provides an estimate for potential systems. Overall, these simulations have revealed some of the problems that were present in the first experimental system. They have also given insight into the properties that a more appropriate experimental system should have.

# Chapter 8: Numerical Solutions of the Poisson-Boltzmann Equation

The Monte Carlo and Brownian dynamics results discussed earlier show a very narrow window where crystallization should occur. As this narrow window will require more exact measurements of interaction energies, a Poisson-Boltzmann equation solver was applied to calculate formation energies. Thus far, only pair interactions have been used to study ionic colloidal crystal behavior in this thesis. The Poisson-Boltzmann solver will provide a more exact calculation to test the validity of the previous results and better ascertain the system conditions necessary to observe ionic colloidal crystal formation.

Before proceeding, a reexamination of the assumptions of the best candidate pair potentials will aid in understanding the need for this study. The Yukawa-type potential assumes the inside of a colloidal particle is identical to that of the solution, but makes no assumption about the surroundings of a particle. If the particle and solution are similar (as is a good approximation for low ionic strengths), this potential should more accurately reproduce colloidal behavior. On the other hand, the Ohshima potential, which gives the exact pair solution for the interaction of two isolated colloidal particles, makes the assumption that no other particles are nearby. This approximation should be more exact at high ionic strengths where screening will prevent other particles in a dense aggregate from affecting the interaction significantly. However, at low ionic strengths, increasing error from this approximation is expected. The last candidate potential is the Wiese-Healy potential, which uses the Derjaguin approximation, limiting the accuracy of the solution to high values of $\kappa a$. The Wiese-Healy potential agrees with the Ohshima potential in the high ionic-strength limit, but significantly underestimates the interaction energy for low ionic strength systems. As no currently available pair potential can exactly capture colloidal behavior, numerical calculations can be used to refine the pair potential results to allow a more accurate evaluation of the energy of dense heterocoagulates. Likewise, these results can also be used to develop higher-order potentials that can then be used to more accurately model colloidal behavior. These new potentials would be useful for the study of a wide variety of colloidal interactions.

## 8.1 Solving the Poisson-Boltzmann Equation

The crystalline structures being studied in this work are a useful medium for studying dense colloidal suspensions. High densities can be obtained without the need for many particles in the simulation cell, which would result in a prohibitive computational expense. An ionic colloidal crystal system, like any other crystalline system, is reduced by symmetry to a small repeat unit. Likewise, the solution of an equation for an infinitely periodic system can be simply treated as the solution of the equation over the repeat unit with the appropriate symmetry-dictated boundary conditions. While in some cases smaller repeat units could be chosen for the ICC systems studied here, the smallest cubic symmetry object was chosen as the repeat unit.

The computational expense of this choice was not prohibitive and it eliminated the potential for errors from using non-perpendicular axes. This geometry also allows the code to be easily adapted for other structures.

A three-dimensional Newton's method [110] solver was written to evaluate the formation energy of an ionic colloidal crystal in the rocksalt structure. While this is the densest binary heterocoagulate, the energetics of formation in this system give insight into the behavior of lower density heterocoagulates as well. A system grid of 100×100×100 elements was commonly used to reduce error without causing a large computational time expense. The resulting Jacobian was a 1,000,000×1,000,000 element sparse matrix, with approximately 7,000,000 non-zero elements. To calculate the potential fields present in a given particle arrangement, the Poisson-Boltzmann equation was solved with Newton's method utilizing a sparse-matrix conjugate gradient method solver from *Numerical Recipes* [110].

The Poisson-Boltzmann equation (Equation 8.1) in its discretized form is shown in Equation 8.2.

$$\nabla(\varepsilon\nabla\psi)-\varepsilon\kappa^2\psi=0,\quad \text{where}\,\kappa=\sqrt{\frac{2000nN_Az^2e^2n}{\varepsilon_0\varepsilon_r kT}} \tag{8.1}$$

$$\frac{\left(\frac{\psi_{i+1,j,k}-\psi_{i,j,k}}{\Delta x}\frac{\varepsilon_{i+1,j,k}+\varepsilon_{i,j,k}}{2}-\frac{\psi_{i,j,k}-\psi_{i-1,j,k}}{\Delta x}\frac{\varepsilon_{i,j,k}+\varepsilon_{i-1,j,k}}{2}\right)}{\Delta x}+$$
$$\frac{\left(\frac{\psi_{i,j+1,k}-\psi_{i,j,k}}{\Delta y}\frac{\varepsilon_{i,j+1,k}+\varepsilon_{i,j,k}}{2}-\frac{\psi_{i,j,k}-\psi_{i,j-1,k}}{\Delta y}\frac{\varepsilon_{i,j,k}+\varepsilon_{i,j-1,k}}{2}\right)}{\Delta y}+$$
$$\frac{\left(\frac{\psi_{i,j,k+1}-\psi_{i,j,k}}{\Delta z}\frac{\varepsilon_{i,j,k+1}+\varepsilon_{i,j,k}}{2}-\frac{\psi_{i,j,k}-\psi_{i,j,k-1}}{\Delta z}\frac{\varepsilon_{i,j,k}+\varepsilon_{i,j,k-1}}{2}\right)}{\Delta z}-\varepsilon\kappa^2\psi_{i,j,k}=0 \tag{8.2}$$

Note that this form of the Poisson-Boltzmann equation is slightly modified from the form reported in Equation 2.27. Here, the dielectric constant appears inside the outer derivative. This is a more general form of the Poisson equation, which applies to systems where the dielectric constant varies spatially. The two derivatives in Equation 8.1 can be evaluated in several ways. The method chosen here involves first evaluating the gradient of the potential at the point between adjacent elements, and then multiplying by the dielectric constant at that point, which is assumed to be the average of the dielectric constants of the two elements. The second derivative is then evaluated at the central element by using the first derivatives at the adjacent nodes. Another method involves applying the chain rule to give two terms: the gradient of the potential dotted with the gradient of the dielectric constant, and the traditional Poisson-Boltzmann equation. In the limit of small Δ*x*, Δ*y*, and Δz, all methods should return identical results. For these simulations, Δ*x*=Δ*y*=Δz due to the cubic symmetry of the repeat unit. Simplifying Equation 8.3, the analytical form of the terms of the Jacobian becomes apparent.

$$\begin{gathered}
-\psi_{i,j,k}\left(3\varepsilon_{i,j,k}+\frac{\varepsilon_{i+1,j,k}+\varepsilon_{i-1,j,k}+\varepsilon_{i,j+1,k}+\varepsilon_{i,j-1,k}+\varepsilon_{i,j,k+1}+\varepsilon_{i,j,k-1}}{2}+\varepsilon\kappa^2\right)+\\
\psi_{i+1,j,k}\left(\frac{\varepsilon_{i+1,j,k}+\varepsilon_{i,j,k}}{2}\right)+\psi_{i-1,j,k}\left(\frac{\varepsilon_{i,j,k}+\varepsilon_{i-1,j,k}}{2}\right)+\psi_{i,j+1,k}\left(\frac{\varepsilon_{i,j+1,k}+\varepsilon_{i,j,k}}{2}\right)+\\
\psi_{i,j-1,k}\left(\frac{\varepsilon_{i,j,k}+\varepsilon_{i,j-1,k}}{2}\right)+\psi_{i,j,k+1}\left(\frac{\varepsilon_{i,j,k+1}+\varepsilon_{i,j,k}}{2}\right)+\psi_{i,j,k-1}\left(\frac{\varepsilon_{i,j,k}+\varepsilon_{i,j,k-1}}{2}\right)=0
\end{gathered} \tag{8.3}$$

The energy of a colloidal system is found by multiplying the magnitude of each surface charge by the electrostatic potential at their location. The mobile ions are not considered in this calculation as their energy is zero due to a balance of electrical and chemical contributions. This can be seen by the fact that the Boltzmann term of the Poisson-Boltzmann equation can be derived by setting the electrochemical potential of the ions equal to zero. This definition of system energy results in a non-zero energy at infinite particle separation. This offset is easily calculated by treating isolated particles with the Poisson-Boltzmann equation.

## 8.2 Cell Setup for the Calculations

Each element in the simulation space has to have the appropriate dielectric constant (ε) and screening (κ) associated with them. While this is trivial for elements inside the particle and in the solution, these values become more complicated at the interface elements. Here, the values of these parameters are based upon the approximate percentages of the element volume taken up by the particle or the solution. Interface elements were identified by checking for different materials at the corner nodes of each element. Once these elements were found, the percentage of the volume occupied by the particle was determined by splitting the element into 8000 sub-cells (20 on a side) and determining if the center of the sub-cell was in the particle or in the solution. Each sub-cell was weighted with the dielectric constant and ionic strength of the material in the center of the sub-cell. The overall values of these parameters for the element were then calculated by averaging the values of all the sub-cells. This acts to smooth the interface between the particle and the solution, reducing effects that would otherwise result from a blocky boundary.

A constant charge distribution boundary condition was selected as it does not give an infinite potential field at particle contact. Furthermore, as was argued in Chapter 3, this boundary condition provides the best physical description of a heterocoagulating system as charge regulating surfaces will tend to become fully charged in those systems. The amount of charge in a surface element was determined by scanning the angles $\theta$ and $\phi$ across the particle surface (with one million total steps) and recording the amount of area in each scanned element. This area was then weighted by the charge per unit area on the surface and the resulting charge was placed in the corresponding element.

The Yukawa-type potential was used as an initial condition for the solution of the Poisson-Boltzmann equation. While any solution can be used, one that is close to the exact solution will converge more quickly and will minimize the chance of finding a region of non-convergence or a non-global minimum.

## 8.3 Verification of Calculation Accuracy

Once the code was functioning, two systems with exact solution were tested to verify the accuracy of the results. The first was a classical ionic crystal and the second was an ionic colloidal crystal with ion-penetrable spheres, which should match the results from Chapter 4.

### 8.3.1 Classical Ionic Crystal Calculation

A dense colloidal system with dielectric constants of one and with no shielding ions was tested and compared to analytical solutions from classical electrostatics. This system was composed of 1 μm particles with +1000 electrons of surface charge and 0.5 μm particles with -1000 electrons of surface charge. The grid size was varied to be 50, 75, 100, or 125 boxes on an edge. The exact solution was calculated by taking the isolated particle energies, which is equal to the charge on the surface multiplied by the surface potential, and subtracting the Madelung energy. The isolated particle energy must be divided by two to balance the number of sites.

$$U_{isolated} = (1000e_c)\psi_{S,1} + (-1000e_c)\psi_{S,2} = \frac{(1000e_c)^2}{4\pi\varepsilon_0(1\cdot 10^{-6})} + \frac{(1000e_c)^2}{4\pi\varepsilon_0(0.5\cdot 10^{-6})} \tag{8.4}$$

$$U_{MSum} = -1.747565\frac{(1000e_c)^2}{4\pi\varepsilon_0 R_{AB}} \tag{8.5}$$

$$U_{Exact} = \frac{(1000e_c)^2}{8\pi\varepsilon_0(1\cdot 10^{-6})} + \frac{(1000e_c)^2}{8\pi\varepsilon_0(0.5\cdot 10^{-6})} - 1.747565\frac{(1000e_c)^2}{4\pi\varepsilon_0 R_{AB}} \tag{8.6}$$

Figures 8.1 through 8.4 show the calculation results. The energy of formation is the primary value of interest in these simulations. It is calculated by subtracting the minimum crystal energy from the isolated particle energy. Figures 8.2 and 8.4 show that the error in the energy calculation increases significantly as the particles become very small relative to the grid.

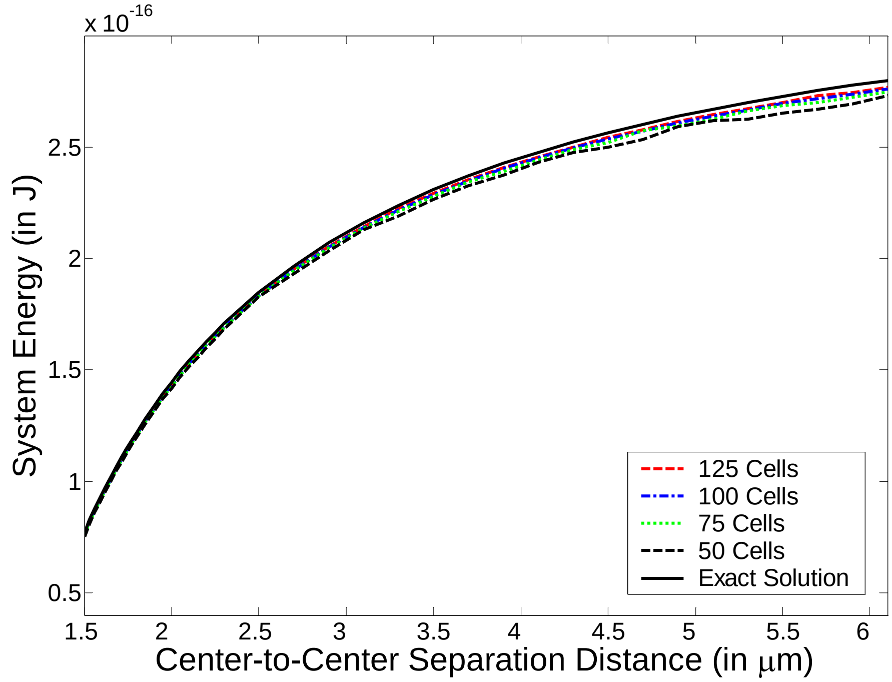

Figure 8.1: For a classical electrostatic system, the calculated energy for a variety of system meshes is compared to the exact solution calculated via a Madelung summation. Even with a coarse mesh, the system energy is quite accurate.

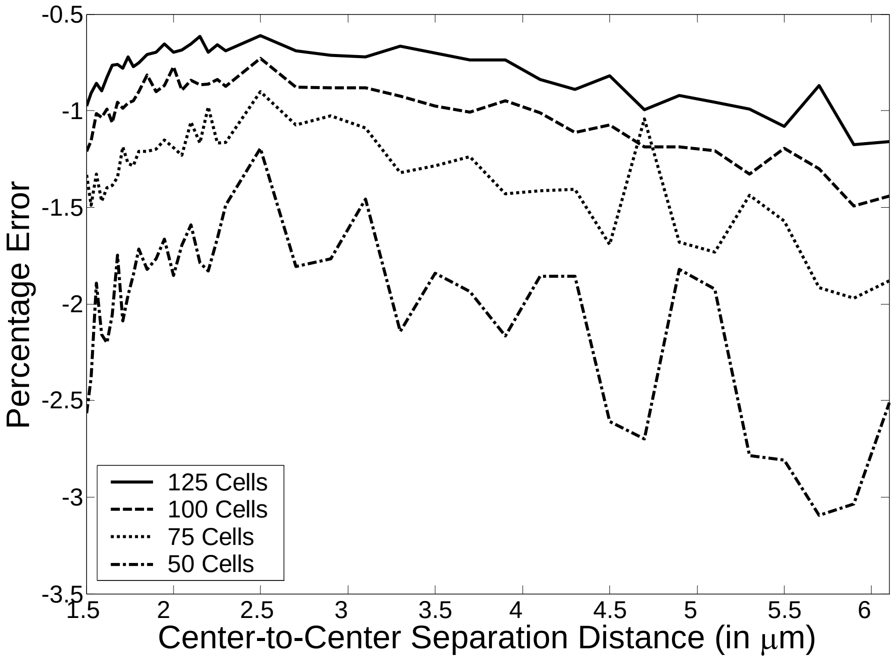

Figure 8.2: The percentage error between the exact solution and that calculated via the various grid sizes is plotted. Even for the coarsest grid (50×50×50), the total error is at most 3%.

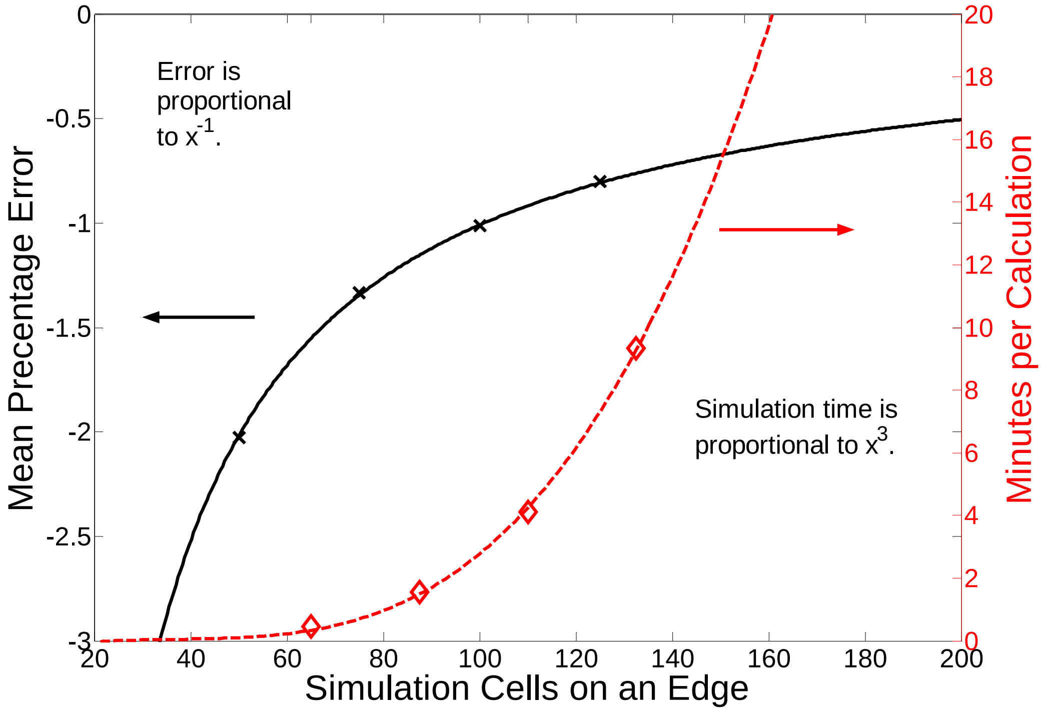

Figure 8.3: The average error from Figure 8.2 is plotted versus the simulation size and the time to complete the calculation of a single energy point. The simulation time increases as the size cubed, while the error decrease as 1/x. As many points at various separations are calculated to find the energy minimum, the computational expense of using fine meshes quickly becomes prohibitive. In this work, all grid sizes are 100×100×100 cells as this reduces the mean error to approximately 1%, while still maintaining reasonable computational times.

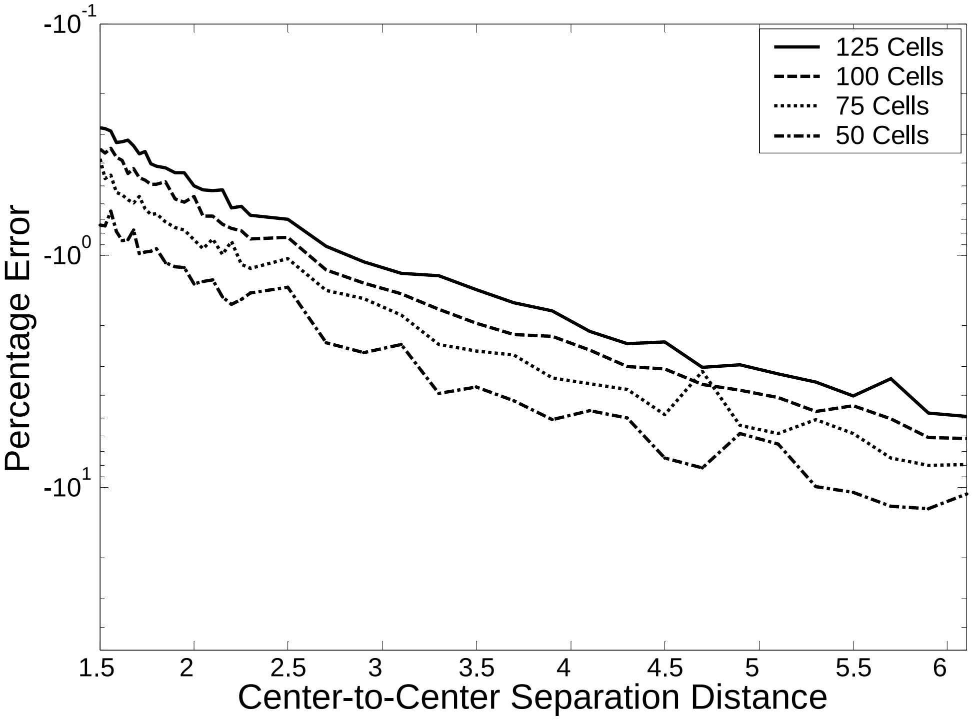

Figure 8.4: The error of the calculation, given as a percentage of the energy at the corresponding separation distance, is plotted versus that separation distance. The minimum energy occurs at the point of closest approach, and therefore, the lowest error also occurs at that point. Thus, the error for the calculated minimum energy of this system would only be approximately 0.5%.

## 8.3.2 Ion Penetrable Sphere Test

The Poisson-Boltzmann solver was also tested with a system composed of ion-penetrable spheres. The energy for this system is accurately described by the Madelung summation method discussed in Chapter 4. The surface potentials are calculated via Equation 2.41. The calculations were conducted with a charge of +1000 $e_c$ (1 μm radius) on one particle and -1000 $e_c$ (0.5 μm radius) on the other. With increased separation distance, the value of Λ needs to be modified to reflect the nearest-neighbor spacing instead of simply the sum of the radii. Figure 8.5 shows the comparison of the calculated energy to the know value.

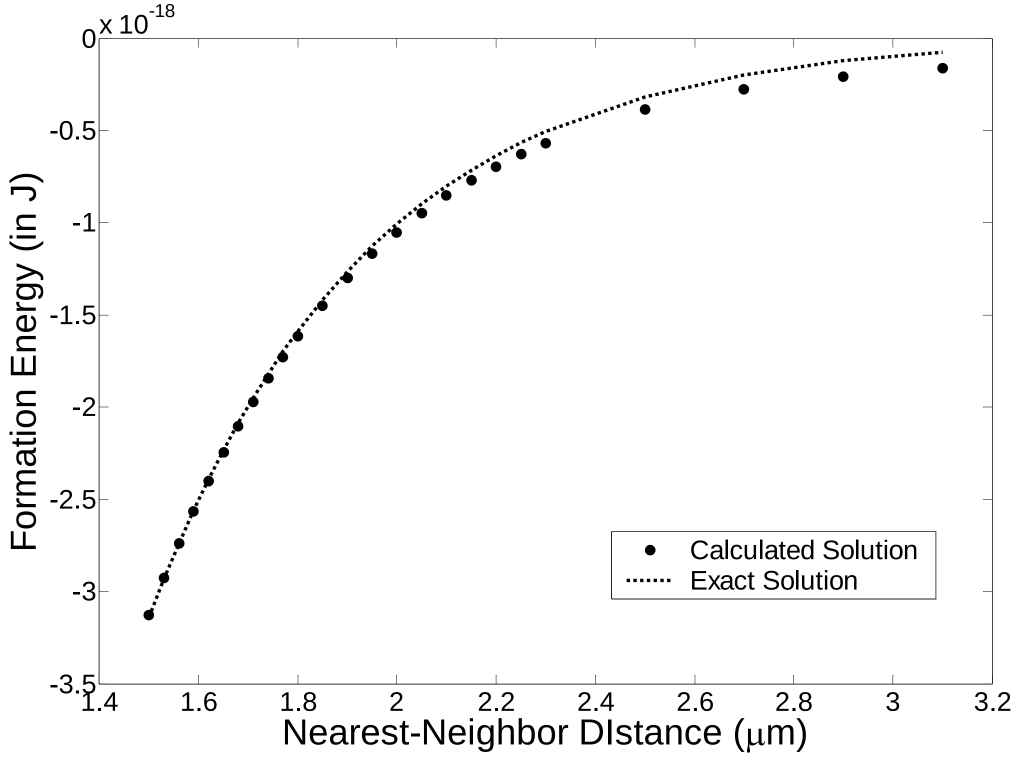

Figure 8.5: The exact solution of the energy of a rocksalt crystal composed of ion penetrable spheres is shown in comparison to the energy from the Poisson-Boltzmann equation solver. As in the previous example, the error is very small for small separations. The increased error at large nearest-neighbor distances is likely due to the coarse discretization of the fields inside of the particles.

## 8.4 Calculation Results

The crystal energy of a rocksalt ICC was calculated with respect to several parameters, including the particle sizes, the amount of charge on the particle surfaces, the dielectric constant of the solution and spheres, and the amount of screening in the solution. Calculations were done similarly to those above, with small increases in particle separation from contact. In some cases, the potential energy minimum was very close to the particle surface, while in others, it was much further from the surface or only occurred at an infinite separation distance. In this section, the results of these calculations are examined to determine how the energy of formation of an ICC, as well as dense heterocoagulates, varies.

## 8.4.1 Variation of Energy with Charge

The variation of the energy with the amount of charge on the surface of the particles was calculated first. For these calculations, the linear case of the Poisson-Boltzmann equation is examined so that the results can be compared to those found with the LSA and Ohshima potentials. The amount of charge on the surface is varied from +500 $e_c$ to +1000 $e_c$ on the 1.0 μm particle and from -500 $e_c$ to -1000 $e_c$ on the 0.5 μm particle, in steps of 100 $e_c$. This gives a charge asymmetry of up to 2:1 on either particle. The energy minimum was calculated by taking the average isolated particle energy, given in Equation 8.7, for each case and subtracting the energy calculated by the simulation.

$$U_{isolated} = \frac{q_1\psi_1 + q_1\psi_1}{2} = \frac{q_1^2}{8\pi\varepsilon_0\varepsilon_e a_1(\kappa a_1 + 1)} + \frac{q_{21}^2}{8\pi\varepsilon_0\varepsilon_e a_2(\kappa a_2 + 1)} \qquad (8.7)$$

Figures 8.6 and 8.7 show the data for values of Λ equal to one and three, respectively. Figure 8.8 illustrates the values along the diagonal, where the surface charge on both the large and small particles is identical. The energy increases with the product of the charges on the two particles and is not symmetric with respect to particle type (i.e. the value of the energy for a given charge ratio depends on which particle has the higher surface charge). After normalizing the energy by the product of the charges, the off-diagonal terms collapse onto a single curve if plotted versus the difference in charges over the square root of the product of the charges. This parameter is a measure of the charge asymmetry of the system, in terms of the total charge. These curves, shown in Figure 8.9, are clearly asymmetric. However, when they are instead plotted versus the square of the charge asymmetry, two separate plots matching the rational expression in Equation 8.8 are obtained for each curve.

$$\frac{U_{Well,Q_1=Q_2} - \Delta U_{Well}}{U_{Well,Q_1=Q_2}} = \frac{1+cx}{1+dx} \qquad (8.8)$$

The two parameters, *c* and *d*, in this equation capture some critical information about the system. The inverse of the first parameter, $c^{-1}$, gives the point where the energy minimum disappears  This is the point where the structure is no longer stable relative to isolated particles. The second parameter captures the rate at which the energy changes with charge asymmetry. Figure 8.10 shows the fits to Equation 8.8 for the Λ=3 data. Table 8.1 gives the fit parameters for all three tested cases mentioned here, as well as the two additional cases of Λ=1 for particles ½ and ¼ of the original sizes.

Figure 8.11 shows the position of the energy minimum scaled by the sum of the particle radii. This corresponds to the lattice spacing of the ICC. Although this is invariant with changes in the product of the charges, it does change with the charge asymmetry. Furthermore, the curve-shape changes with the value of Λ but not with particle size.

### 8.4.2 Variation of Energy with Other Parameters

Once the basic trends with respect to the charge product and asymmetry were determined, the formation energy was also examined as a function of the sum of the particle sizes, Λ, and the solvent dielectric constant. Figures 8.12 through 8.14 show the results of these calculations. These simulations were done with the size of the small particle fixed at 50% of the large particle size.

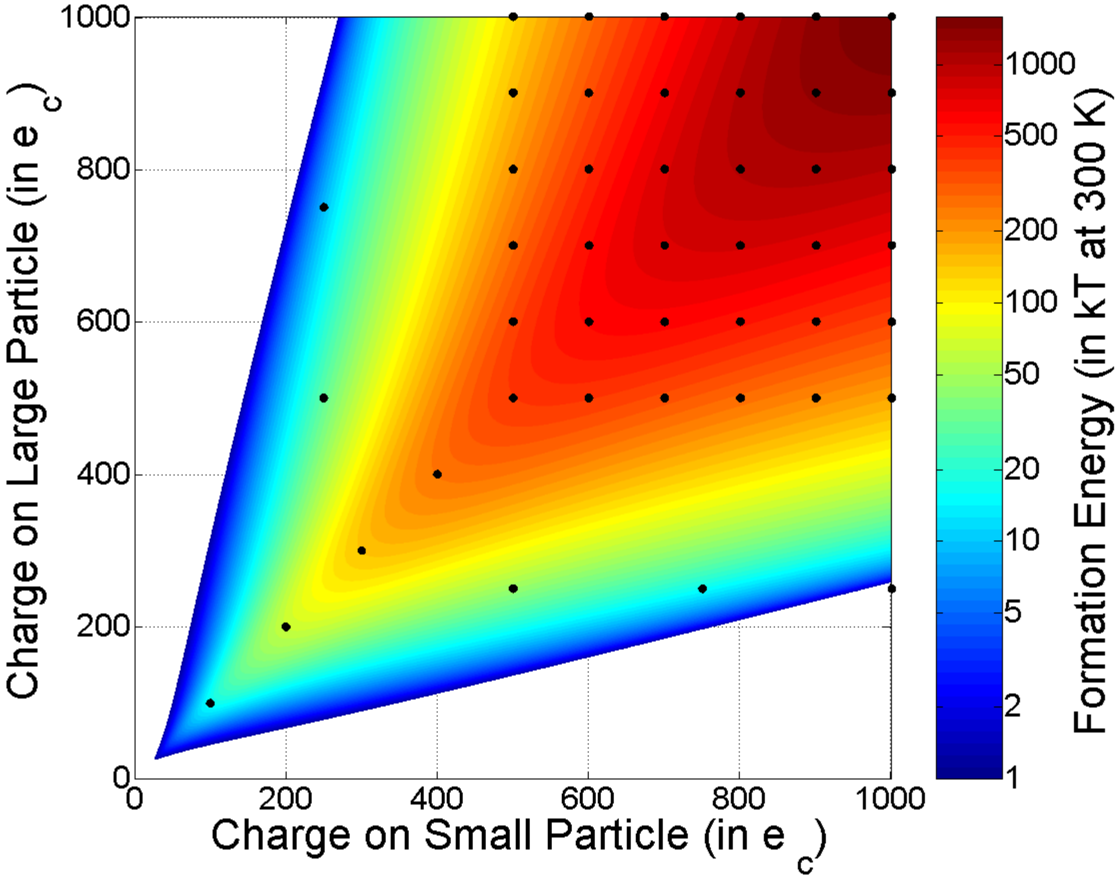

Figure 8.6: Simulation data for the condition of Λ=1 for 1 μm and 0.5 μm particles in the rocksalt structure are shown relative to the fit of the data. The black dots represent each calculation. The surface plot is calculated by the fits versus $Q_1Q_2$ and $(Q_1-Q_2)^2/(Q_1Q_2)$. $Q_1$ and $Q_2$ are the absolute magnitudes of charges on each particle in units of electron charge. Note that the deepest energy well occurs when the amount of surface charge on both particles is equal. This matches the classical electrostatic case even with increasing Λ, and is in contradiction to the presently available potentials that describe colloidal behavior.

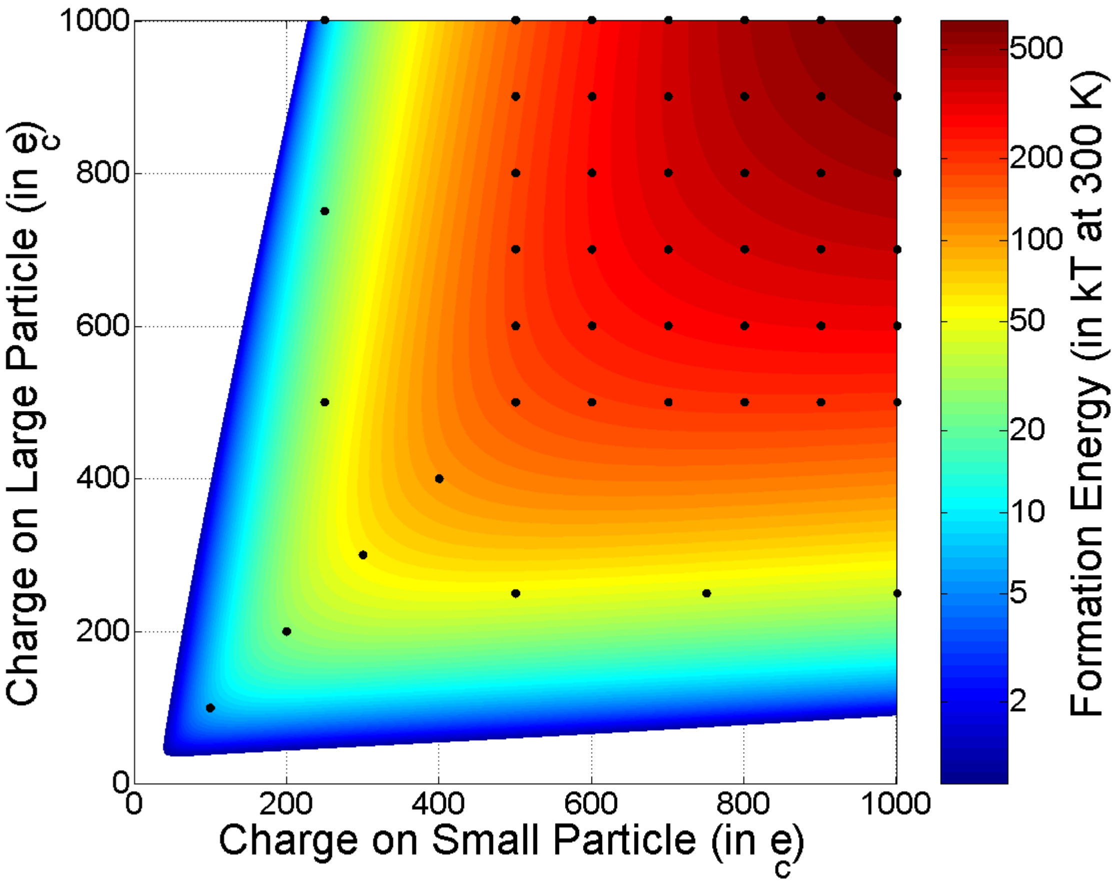

Figure 8.7: Calculation results for the Λ=3 case are given relative to the fit of the data. Note that this system is more asymmetric than the Λ=1 system. A much larger energetic penalty is present for a system with excess charge on the larger particles as they are closer to one another than the small particles. When no screening is present, the penalty is identical, while with screening, the system becomes more sensitive to charge excess on the larger particle. Also note that the formation energy for the structures has dropped by a factor of two.

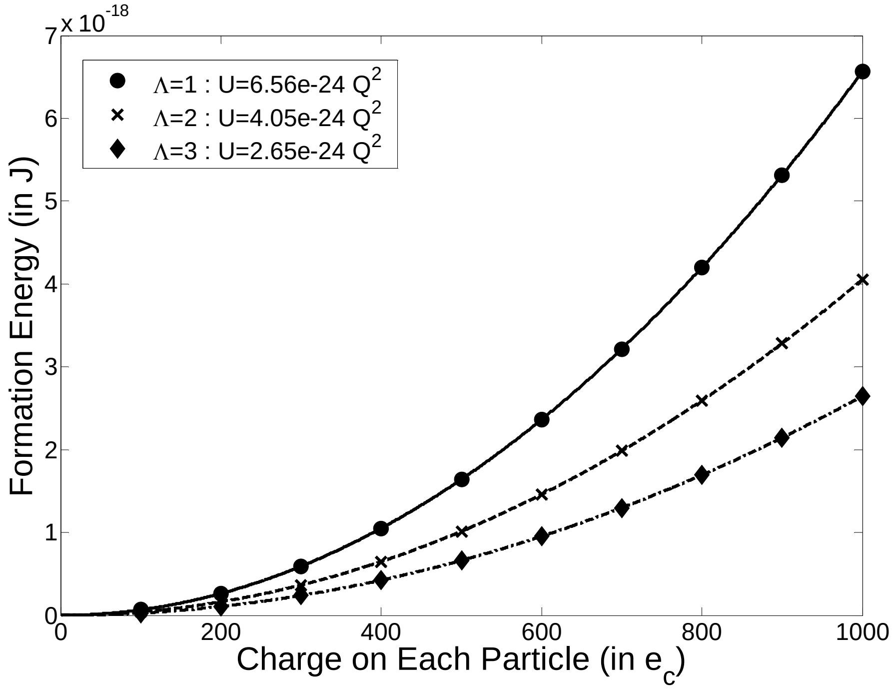

Figure 8.8: The formation energy of the rocksalt structure for the case of equal charges on both particles is shown versus the charge on each particle. The data falls on a parabola centered at $Q_1$=$Q_2$=0.

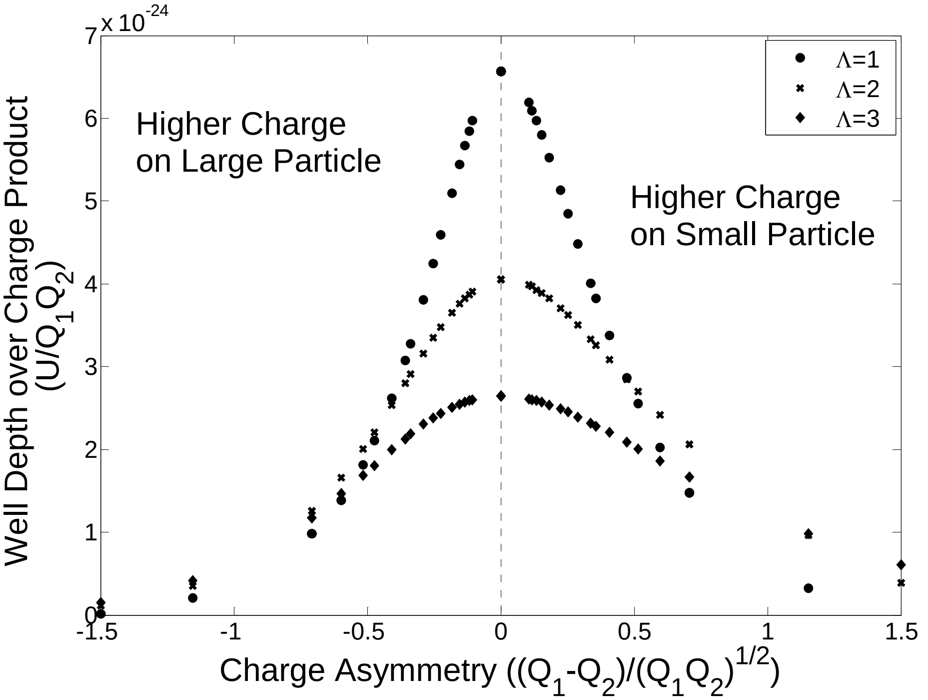

Figure 8.9: The effect of charge asymmetry on the formation energy of an ICC is shown. The magnitude of the energy minimum decreases more slowly if the higher charge is on the smaller particle. Again, $Q_1$ and $Q_2$ are absolute magnitudes of charge, with $Q_1$ corresponding to the magnitude of charge on the small particle and $Q_2$ to that on the larger particle.

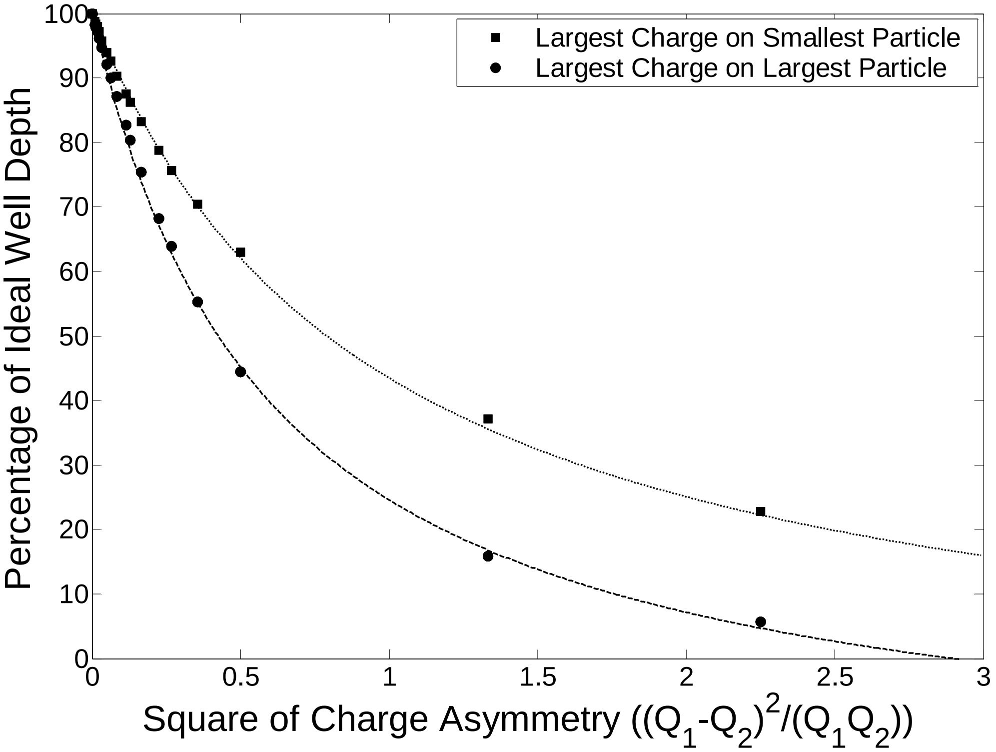

Figure 8.10: The percentage of the normalized well depth for the Λ=3 case is given versus the charge asymmetry squared. The functions fall off differently depending on which particle has the excess charge.

Table 8.1: The fit parameters for both variables, $Q_1Q_2$ and $(Q_1-Q_2)^2/(Q_1Q_2)$, for five tested cases. The fit of Equation 8.12 does not change with particle size variations. All systems were calculated with a solvent $\varepsilon_r$ of 20 and a particle $\varepsilon_r$ of 2.5281, corresponding to 2-propanol and polystyrene, respectively.

| | | | | Excess Q on a1 | | Excess Q on a2 | |
|---|---|---|---|---|---|---|---|
| a1 (μm) | a2 (μm) | Λ | Q1Q2 Coeff | c | d | c | d |
| 0.5 | 1 | 1 | 6.56E-24 | -0.43 | 4.95 | -0.45 | 8.07 |
| 0.5 | 1 | 2 | 4.05E-24 | -0.27 | 1.47 | -0.40 | 3.01 |
| 0.5 | 1 | 3 | 2.65E-24 | -0.12 | 1.04 | -0.35 | 1.66 |
| 0.5 | 1 | 4 | 1.81E-24 | -0.07 | 0.91 | -0.29 | 1.06 |
| 0.5 | 1 | 5 | 1.30E-24 | -0.06 | 0.92 | -0.28 | 0.63 |
| 0.25 | 0.5 | 1 | 1.31E-23 | -0.45 | 4.85 | -0.48 | 7.96 |
| 0.125 | 0.25 | 1 | 2.67E-23 | -0.44 | 4.99 | -0.49 | 8.05 |

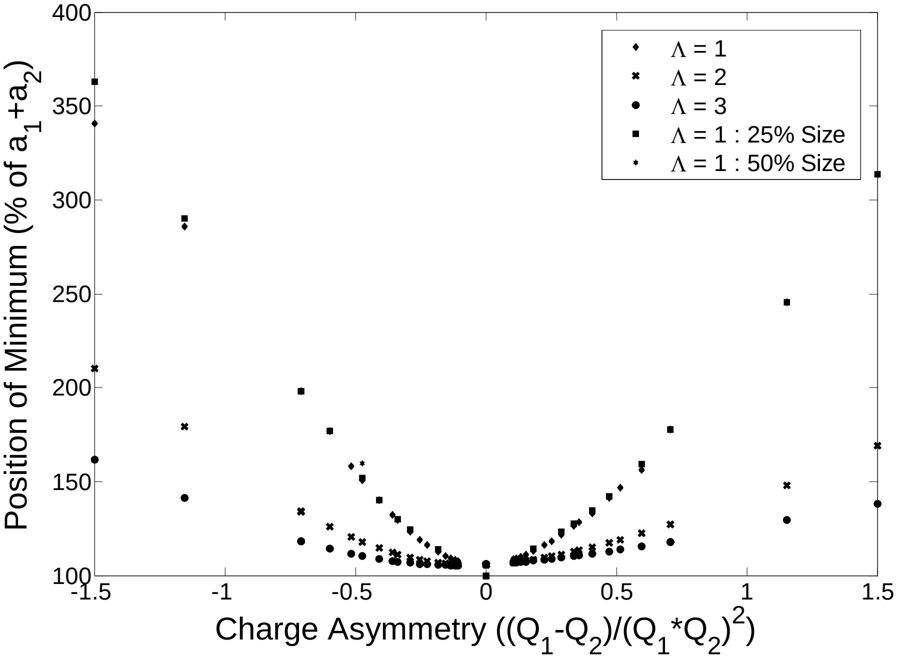

Figure 8.11: The position of the energy minimum relative to the sum of the particle radii is shown for the five systems tested. Note that all curves for Λ=1 fall on top of one another when scaled in this fashion.

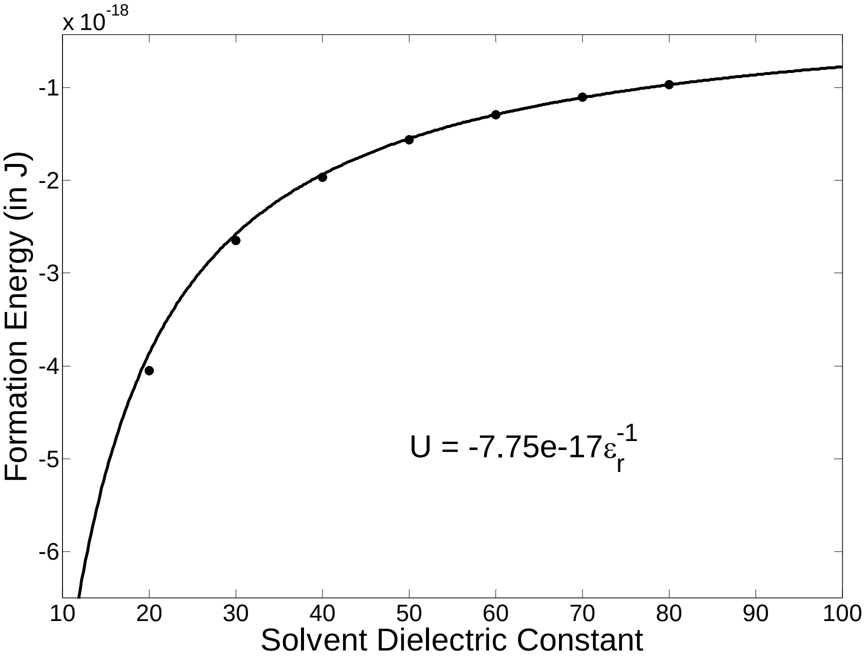

Figure 8.12: The system energy varies as one over the solvent dielectric constant for the $Q_1=Q_2$ case. At the lower extreme, the energy begins to diverge from the $\varepsilon^{-1}$ behavior. This is most likely due to the solvent dielectric constant approaching that of the particles and thereby increasing the impact of the particle core on the electrical fields.

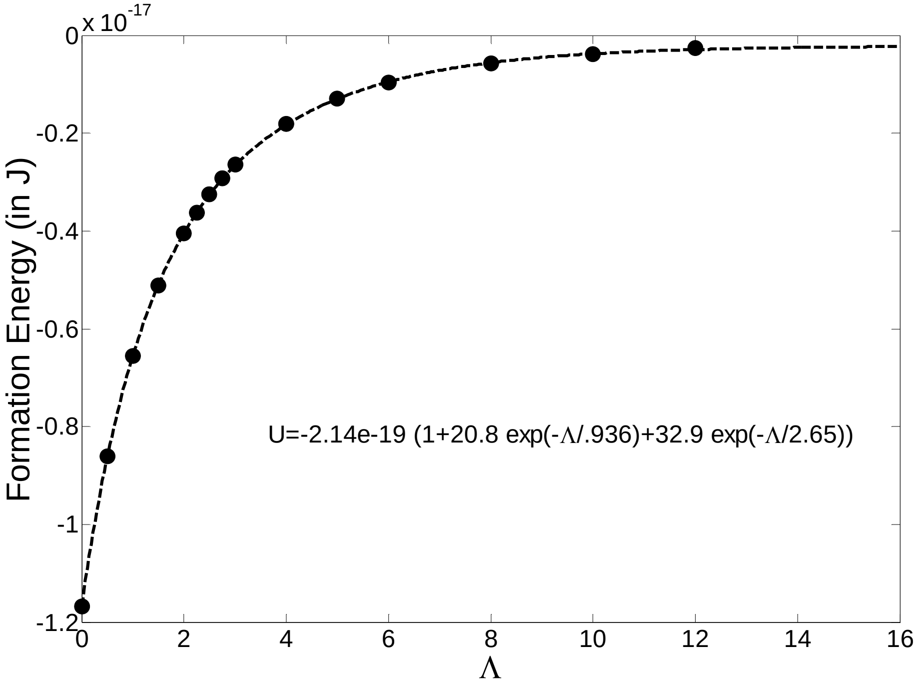

Figure 8.13: The variation of the well depth with screening is calculated for the $Q_1$=$Q_2$ case. For a constant surface charge on both particles, the formation energy quickly approaches zero with increasing Λ.

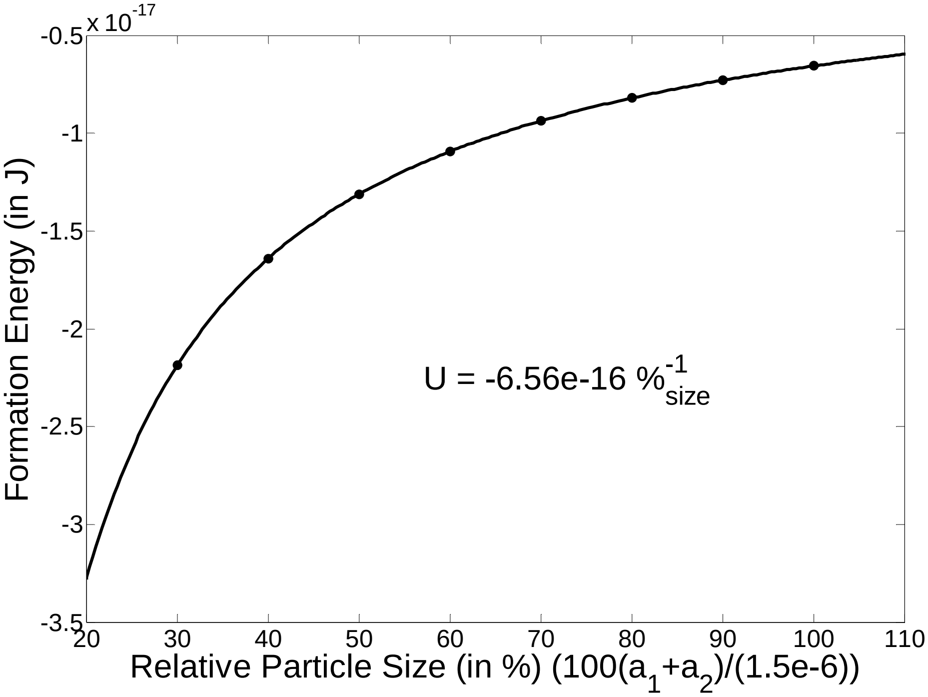

Figure 8.14: The variation of the formation energy with relative particle size, $(a_1+a_2)/(1.5e\text{-}6)$, is shown. The data fit very well to the function $x^{-1}$.

This analysis now allows the heterocoagulate energy per particle to be written in terms of these parameters. This expression is given in Equation 8.9, with $Q_1$ corresponding to the charge on the small particle and $Q_2$ to the charge on the large particle.

$$U = \frac{0.0278}{4\pi\varepsilon_0\varepsilon_{r,solvent}}\frac{Q_1Q_2e_c^2}{(a_1+a_2)}\frac{1+c\dfrac{(Q_1-Q_2)^2}{Q_1Q_2}}{1+d\dfrac{(Q_1-Q_2)^2}{Q_1Q_2}}\left(1+20.8\exp\left(-\frac{\Lambda}{0.936}\right)+32.9\exp\left(-\frac{\Lambda}{2.65}\right)\right) \tag{8.9}$$

The two constants $c$ and $d$ are given by Equations 8.10 and 8.11, respectively.

$$\begin{cases} \text{if } Q_1 > Q_2\,, \quad c = -0.435 + \dfrac{0.182}{0.378\sqrt{\pi/2}}\exp\left(\dfrac{-2}{\Lambda^4\, 0.378^2}\right) \\ \text{if } Q_1 < Q_2\,, \quad c = -0.451 + \dfrac{0.063}{0.298\sqrt{\pi/2}}\exp\left(\dfrac{-2}{\Lambda^4\, 0.298^2}\right) \end{cases} \tag{8.10}$$

$$\begin{cases} \text{if } Q_1 > Q_2\,, \quad d = 29.07\exp\left(\dfrac{-\Lambda}{0.506}\right) + 0.922 \\ \text{if } Q_1 < Q_2\,, \quad d = 20.862\exp\left(\dfrac{-\Lambda}{0.945}\right) + 0.667 \end{cases} \tag{8.11}$$

The full-width at half max of the charge asymmetry effect, shown in Figure 8.9, is given by Equation 8.12.

$$FWHM = \sqrt{\frac{1}{d-2c}} \tag{8.12}$$

Figure 8.15 shows the formation energy versus the percentage error between the fit in Equation 8.9 and the actual results from the calculation. While complex, this expression captures the energy of a rocksalt ordered heterocoagulate over a broad range of system conditions. The only constraint on these results is that one particle must be one half of the size of the other. This formulation can be used to evaluate the occurrence of heterocoagulation in general. Likewise, this expression can be compared to the energy obtained by applying the pair-wise Yukawa, Ohshima, or Wiese-Healy potentials to an ICC.

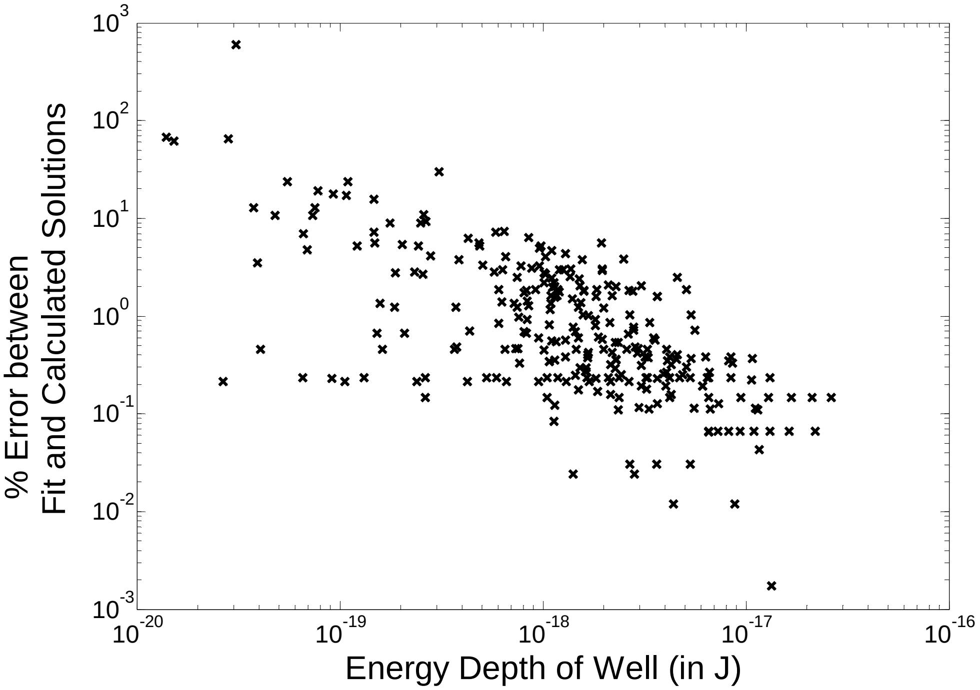

Figure 8.15: The error between the fit given in Equation 8.12 and the solver calculation as a function of formation energy. Notice the percentage error is substantially lower for large energies.

## 8.5 Comparison to Available Pair-Potentials

Comparison to the Yukawa-type potential is straight-forward as the lowest system energy occurs at particle contact under this model. However, the Ohshima and Wiese-Healy potentials require multiple lattice spacings to be calculated as there is a minimum in the potential away from contact, similar to that observed earlier in this section. These calculations show that all three pair-potentials underestimate the energy of the $Q_1=Q_2$ colloidal aggregate at low ionic strengths. Also, the minimum energy position in terms of charge ratio is different for all three cases.

Figure 8.16 shows the formation energy of an ICC rocksalt structure for the three potentials as a function of surface charge asymmetry. The Wiese-Healy and Ohshima potentials underestimate the crystalline energy, especially at low ionic strengths. This difference is more severe for the Wiese-Healy solution at a charge asymmetry equal to zero. Alternatively, the Yukawa potential overestimates the energy, with the error increasing rapidly with ionic strength. Although the Ohshima potential is closer than the Yukawa at higher ionic strengths, the Yukawa potential becomes more accurate for low ionic strengths, which is the relevant regime for ICCs. At a charge ratio equal to one, the exact solution is always between the Yukawa solution and the Ohshima solution.

The position of the minimum potential in Figure 8.16 should also be considered. For the Yukawa-type potential, the value of the potential is always a minimum at particle contact. However, for the Ohshima potential and the exact solution, the minimum of the potential well is away from the particle surface. For a charge ratio equal to one, the Ohshima potential overestimates the ideal nearest-neighbor separation distance, consistently giving a larger separation distance than the exact case. This is illustrated in Figures 8.17 and 8.18.

The Ohshima potential becomes more accurate at high ionic strengths because the potential fields are reaching a shorter distance preventing nearby particles from contributing to the pair interaction energy. However, at these high ionic strengths, the potential does not reach past the nearest neighbor as is desired for ICC formation. At lower ionic strengths, the potential field is impacted by more than just the nearest particle in a given direction, causing the pair-potential to become inaccurate.

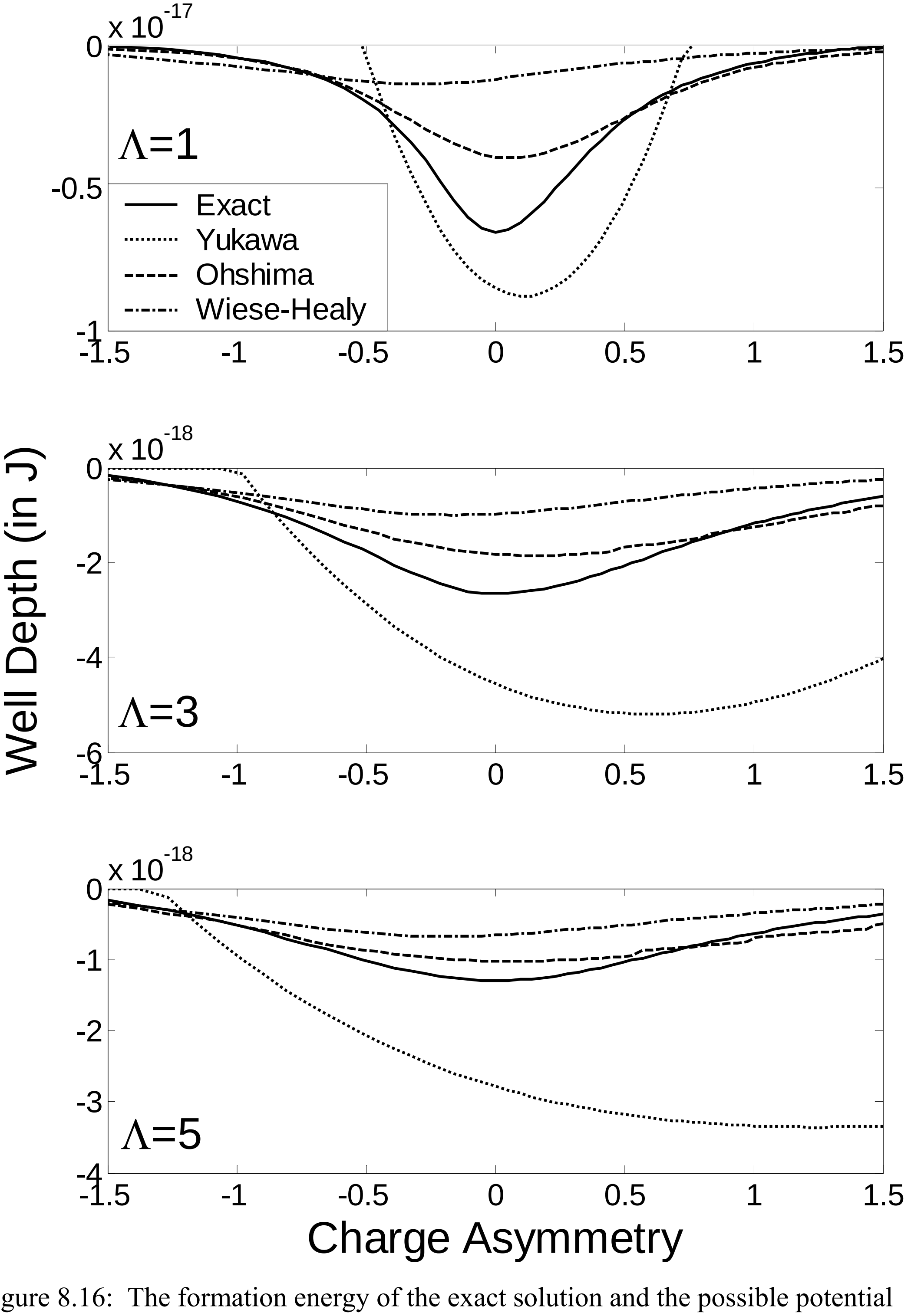

Figure 8.16: The formation energy of the exact solution and the possible potential models for a constant charge boundary condition are shown. For low ionic strengths, the Yukawa type potential is much closer to the exact solution than at higher ionic strengths. At high ionic strengths, the Ohshima model is more accurate.

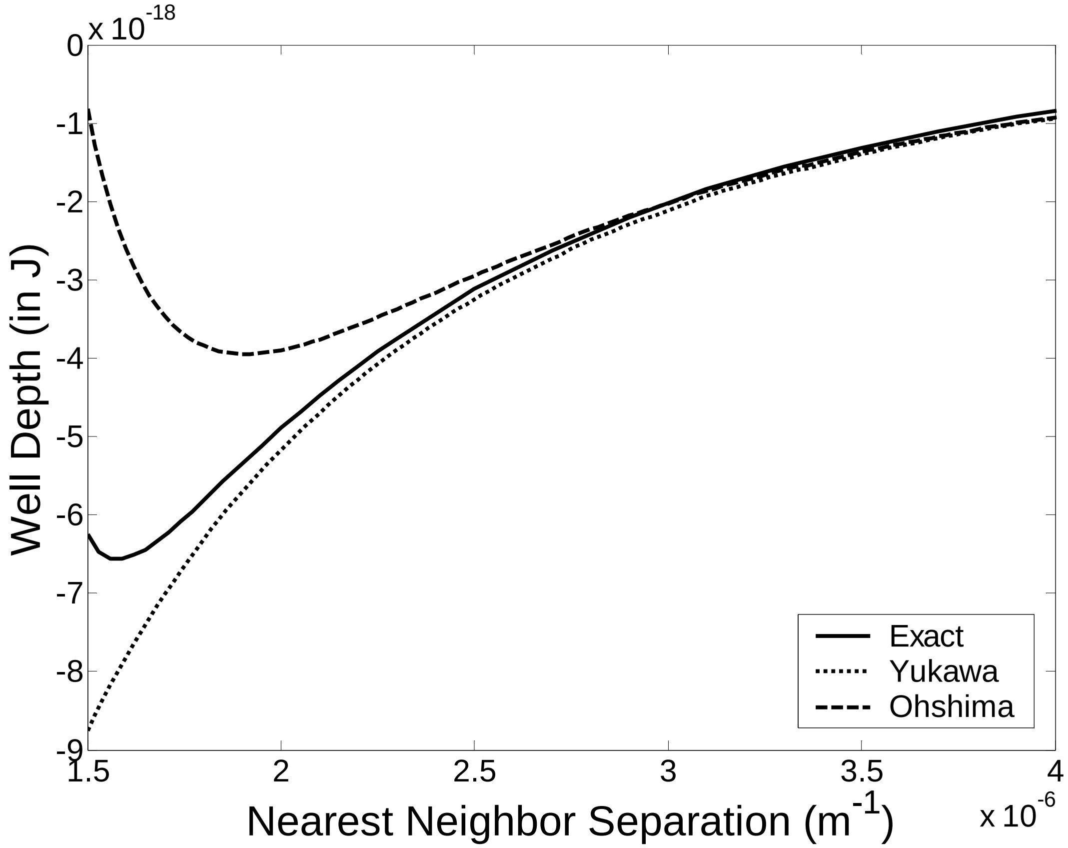

Figure 8.17: The crystalline formation energy is shown versus nearest neighbor separation distance for a 1 μm and 0.5 μm particle system with 1000 electron charges on each at $\Lambda$=1. The Yukawa potential has a minimum at particle contact, while the exact solution has a minimum at approximately 110% of $a_1+a_2$. However, the Ohshima solution places the particles nearly 130% of $a_1+a_2$ apart. In this regime, the Yukawa potential is more accurately modeling the colloidal behavior.

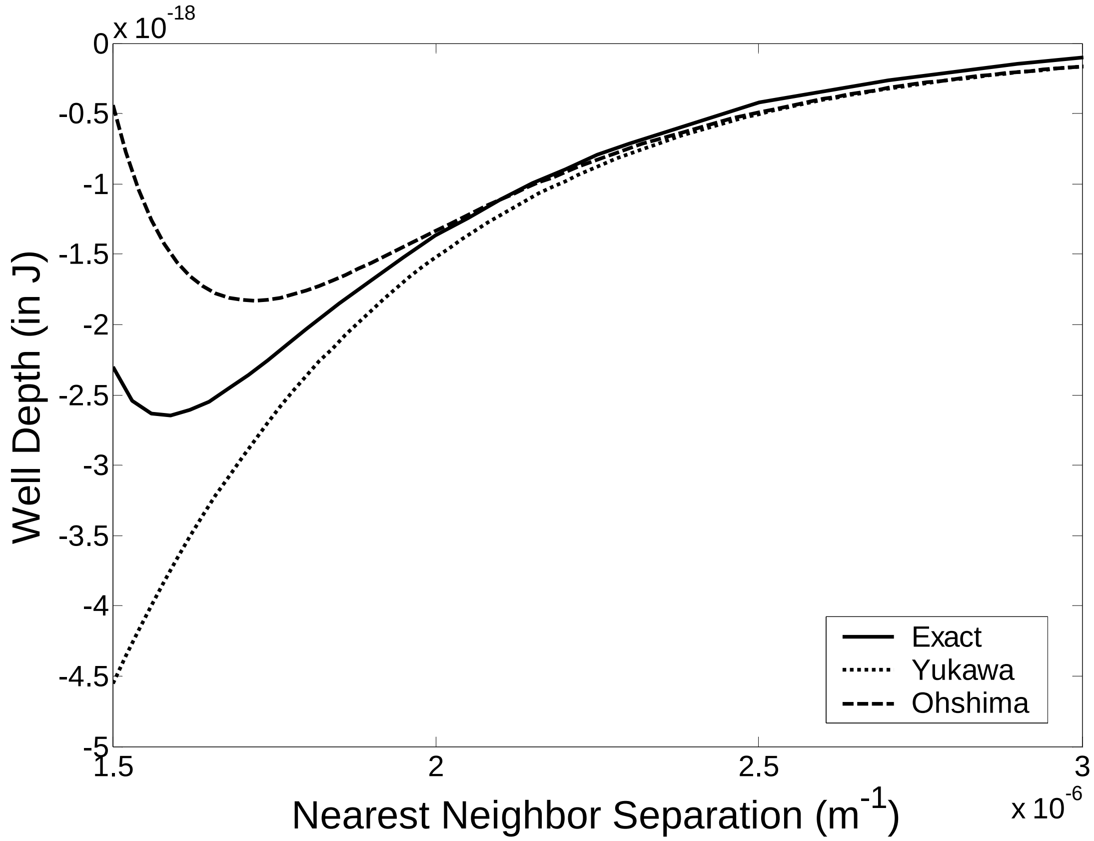

Figure 8.18: The crystalline formation energy for a similar system to that in Figure 8.20 is shown for Λ=3. Note that the Ohshima potential still significantly overestimates the optimal particle separation distance. This regime is a crossover between the regimes where the Yukawa and Ohshima potentials are most accurate. In this regime, a higher order potential would be very advantageous for colloidal modeling.

## 8.6 Implications of PBE Solver Results

The Poisson-Boltzmann equation solver illustrates several new and important concepts in colloidal science. Due to their approximations, all currently available pair potentials are useful only in certain regimes for dense heterocoagulates. This result points to the need for a higher order potential, such as a colloidal equivalent of an embedded atom potential or a force-fitted potential, can be developed for use in dense colloidal modeling. The results of these calculations provide a framework in which to test new colloidal potentials for accuracy. As discussed earlier, despite the shortfalls of the Yukawa-potential, it is frequently used to model many aspects of colloidal behavior even at high ionic strengths. Due to the approximation regarding the particle dielectric and ionic properties, the Yukawa-type potential was expected to be more accurate at lower ionic strengths where this assumption is more valid. Also, the longer reach of the potentials at low ionic strengths make any assumptions regarding the presence of other particles less valid. The Ohshima potential, even with its large complexity does not capture dense colloidal behavior at low ionic strengths due to these extra interactions. For high ionic strengths, where additional particles do not impact the local potential fields, the Ohshima potential is much more accurate. Until higher order potentials can be developed, the Yukawa potential should be used for low ionic strength suspension, while the Ohshima potential should be used at high ionic strengths. For very high ionic strengths ($\Lambda>10$), the Ohshima and Wiese-Healy potentials agree and either may be used with little error.

The second important result from these calculations lies in the definition of charge ratio, which is shifted from that predicted by any of the pair potentials. The relevant parameter is shown to be the surface charge ratio. The new ratio is given in terms of more easily measured parameters by Equation 8.13.

$$Q_{ratio} = \frac{a_1 \psi_1 (\kappa a_1 + 1)}{a_2 \psi_2 (\kappa a_2 + 1)} \tag{8.13}$$

This equation is the first two terms of the Taylor expansion for the charge ratio given by the Yukawa methodology (Equation 4.9). This supports the conclusion that the Yukawa potential is accurate for low screening ratios.

Beyond the implications to colloidal simulation and modeling, the Poisson-Boltzmann equation solver results also illustrate several important aspects of heterocoagulate behavior. Two constant charge distribution surfaces will be separated in equilibrium as predicted by the Ohshima and Wiese-Healy potentials. However, for a dense system at low ionic strengths, these models overestimate the repulsion, thereby underestimating the interaction energy. Interestingly, as shown in Figure 8.14, a highly charge asymmetric system is at equilibrium at large separations up to 300% of the sum of the radii. Such a system could be used to make binary ordered colloidal crystalline arrays. Presently such colloidal crystalline arrays (CCA) are only made with repulsive interactions by gradually increasing the extent of the iteractions by removing salt ions through ion exchange or dialysis. The AB attraction would provide a means to obtain both $A_xB_{1-x}$ alloys and $A_xB_y$ ordered superlattices that would not be obtainable through normal CCA methods.

Finally, the energetics of ICC structures are now more accurately calculated allowing a better estimation of the melting point of such systems. Further applications of the Poisson-Boltzmann equation solver developed here include the study of other ionic structures, as well as the energetics in purely repulsive systems. As the model has been shown to accurately predict the energy for close particle approaches, the solver can be easily adapted to test pair potentials in a purely repulsive system.

# Chapter 9: Experimental Verification of Calculations

In Chapter 8, the lowest energy state for a dense heterocoagulate was shown to occur when the magnitudes of the surface charge on both particles are equal. This result is verified through further experiments presented in this chapter. Additionally, the analysis presented in Chapter 8 can be used to verify otherwise unexplained heterocoagulation behavior in the literature. From these results, heterocoagulation behavior is not dominated by the apparent point charge, but instead by the total surface charge present in the system. No pair potential currently in the literature describes this behavior. Also, charge ratio is shown to be an important parameter in determining the stability of a heterocoagulate, with several cases showing no heterocoagulation due to charge ratio effects. The effect of charge ratio on heterocoagulation behavior has not, to our knowledge, been previously explored. This result becomes especially significant for systems with low screening ratios, such as low ionic strength systems or increasingly important small particle systems.

## 9.1 System Selection and Preparation

To test the heterocoagulation behavior described above, a variety of particles were selected for possible ICC systems. The particles were all made of functionalized polystyrene to ensure constant charge boundary conditions. As the particle sizes included many particles less than 500 nm, it was necessary to find a new method to resuspend the particles in 2-propanol. Dialysis was explored as a technique to remove impurities from the starting particles. The particles were dialyzed against deionized water in Float-a-lyzer dialysis bags from Spectrum Labs. As the colloidal particles are greater than 100 nm in size, any pore size smaller than 1,000,000 Daltons was useful for these purposes. Due to limited supply of 300,000 Dalton bags, occasionally 100,000 Dalton bags were used. Dialysis was continued until no change in the conductivity of the reference solvent was observed during the dialysis time. This often required 4 to 5 iterations for 5 mL of particles against one liter of deionized water. The final conducitivty of the water was 1 MΩ-cm. After removing the majority of impurities from the water, the particle solutions were diluted with 2-propanol at least five times. Before use, the particles were again diluted around 10 times. The final amount of water is then estimated to be less than 2%. Also, the ions producing the conductivity in the water would be diluted ($8\times10^{-8}$ mol/L) to below the native level of ions present in the 2-propanol. Thus, the remnant ions caused little impact on the screening ratio. The conductivity after mixing is estimated to be 100 MΩ-cm, giving an ionic strength of approximately $3.3\times10^{6}$ mol/L and a value of $\kappa$ of $3.75\times10^{6}$ m$^{-1}$.

Due to the nature of dialysis, only a minority component can be exchanged. For example, dialysis done on water against 2-propanol would be unsuccessful. In this case a large osmotic pressure would develop and the water would move into the 2-propanol much faster than the flux in the other direction. Thus, the bag containing the water would rapidly shrink during this process. It is possible to first dilute the particles with 2-propanol and then dialyze the solution against pure 2-propanol. In this case the water could be removed with a maximum 20% change in volume of the dialysis bag. This procedure would require many dialysis steps against pure 2-propanol. For these purposes, Float-a-lyzer dialysis bags are unacceptable as the sealant dissolves in 2-propanol. Instead PVDF dialysis bags can be obtained from Spectrum Labs for this purpose. One end of the bag is heat sealed and the other is clamped. As a dialysis bag is destroyed if allowed to dry, once a dialysis bag is wetted with 2-propanol, it is necessary to immediately switch the bag from one solvent to another due to the high evaporation rate of 2-propanol. The particles used here are all purified using the first method discussed above in Float-a-lyzer dialysis bags.

Once resuspended in 2-propanol, zeta potential and concentration measurements were made as outlined in Chapter 5. The compiled results for the systems used in later experiments are included in Table 9.1.

Table 9.1: The eight particle systems considered in this work are shown. The particle systems are all very monodisperse with CV's of less than 4%. Most functionalization groups exhibited very similar zeta potentials except for the 415 nm sulfate group.

**Negatively Charged Particles**

| Size (nm) | Surface Group | CV (%) | Batch | Mobility | St. Dev. | St. Err. | Zeta Pot. (mV) |
|---|---|---|---|---|---|---|---|
| 113 | Sulfate | 3.7 | 940 | -0.529 | 0.091 | 0.023 | -85.7 |
| 143 | Sulfate | 2.3 | 10-307-57 | -0.538 | 0.051 | 0.023 | -87.0 |
| 209 | Sulfate | 3.1 | 1312 | -0.532 | 0.067 | 0.015 | -85.9 |
| 415 | Sulfate | 3.6 | 1951 | -0.306 | 0.142 | 0.021 | -49.7 |
| 1310 | Sulfate | 2.7 | 1279 | -0.507 | 0.115 | 0.036 | -81.8 |

**Positively Charged Particles**

| Size (nm) | Surface Group | CV (%) | Batch | Mobility | St. Dev. | St. Err. | Zeta Pot. (mV) |
|---|---|---|---|---|---|---|---|
| 215 | Q. Amine | 2.2 | 791 | 0.549 | 0.102 | 0.011 | 88.6 |
| 622 | Amidine | 3.1 | 1500 | 0.512 | 0.101 | 0.032 | 82.7 |
| 749 | Amidine | 3.2 | 1559.0 | 0.590 | 0.054 | 0.010 | 95.4 |

## 9.2 Preliminary Mixing Experiments

Particle combinations were mixed in 1:1 and 2:1 ratios. These combinations were dried as well as left to settle in centrifuge tubes. A variety of behaviors were observed in both the dried and settled states. Figure 9.2 exhibits the 1:1 mixed samples and Figure 9.3 exhibits the 2:1 mixtures. These figures illustrate the varied behaviors of these experimental systems, including dense heterocoagulates, loose heterocoagualtes, and stable suspensions. These results suggest a method for determining charge ratio in heterocoagulating systems, which is described in the following section.

## 9.3 Further Mixing Experiments

From these results, it is clear that number ratio of particles can have a large impact on heterocoagulation behavior. If charge ratio is a critical parameter in heterocoagulation, heterocoagulation should be fastest when the charge ratio and number ratio are matched, corresponding to net zero charge coagulates. For example, a system with a charge ratio of 3:1 may not form rapid heterocoagulates at a 1:1 number ratio, but may heterocoagulate rapidly in a 1:3 mixture. Four different systems were used to test and confirm this hypothesis. Figures 9.3 through 9.6 show the results of these tests for the four systems. Note that the number ratio corresponding to the fastest settling rate varies from sample to sample. As these systems all target an approximate 1:2 size ratio, this parameter was not a factor in the changing heterocoagulation behavior observed in these experiments. Note that in one system, no heterocoagualtion is visible in the vials at any of the tested number ratios. The number ratios reported here are given in terms of large:small and the ionic strength of the 2-propanol was assumed to be equal to that calculated in Chapter 5.

Figure 9.1 A variety of 1:1 mixed samples are shown in both a dried and wet state. Samples 1-6 and 1-11 are repulsive control samples. The heterocoagulated samples show a variety of behavior, including a stable solution (1-14), a frosted appearance (1-12), complete heterocoagultion (1-21) and a low density aggregate (1-16). The variety of behavior indicates vast differences in the interaction forces in these samples.

Figure 9.2: The 2:1 mixtures matching those in Figure 9.1 are shown. There are some marked changes in behavior from the 1:1 mixtures: 2-10 is frosted, while 1-10 is not; 2-13 is more widely spread out; 2-21 is lower in density. These changes in behavior are believed to indicate a method to determine charge ratios in the systems.

b

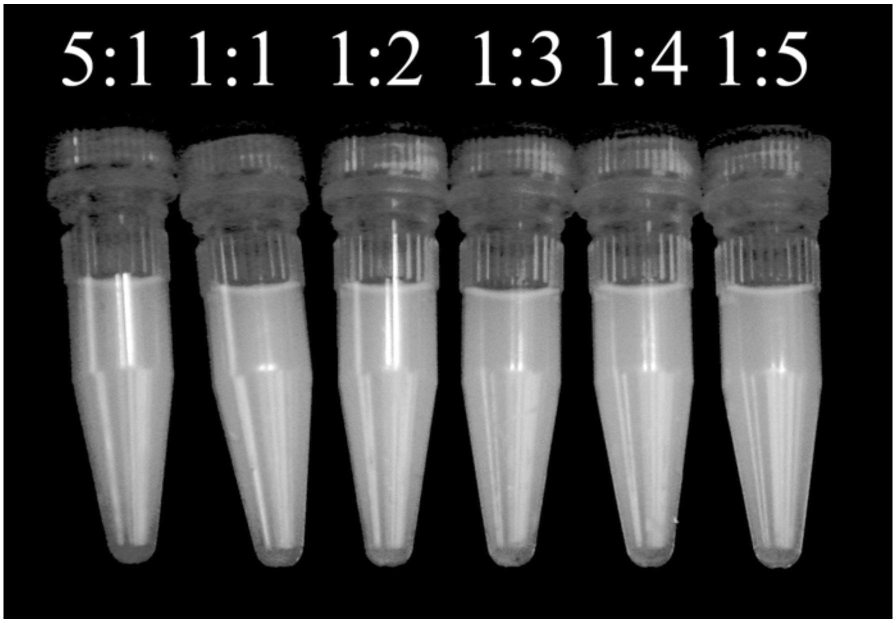

Figure 9.3: After 1200 minutes, the 113 nm PS-S and 215 nm PS-QA system shows no signs of settling. Two possible explanations are that the small Λ of this system (due to the small particle size) limits the heterocoagulation range to a value in between two of the tested values, or the small particle size results in a heterocoagulation energy below the effective boiling point of the heterocoagulate.

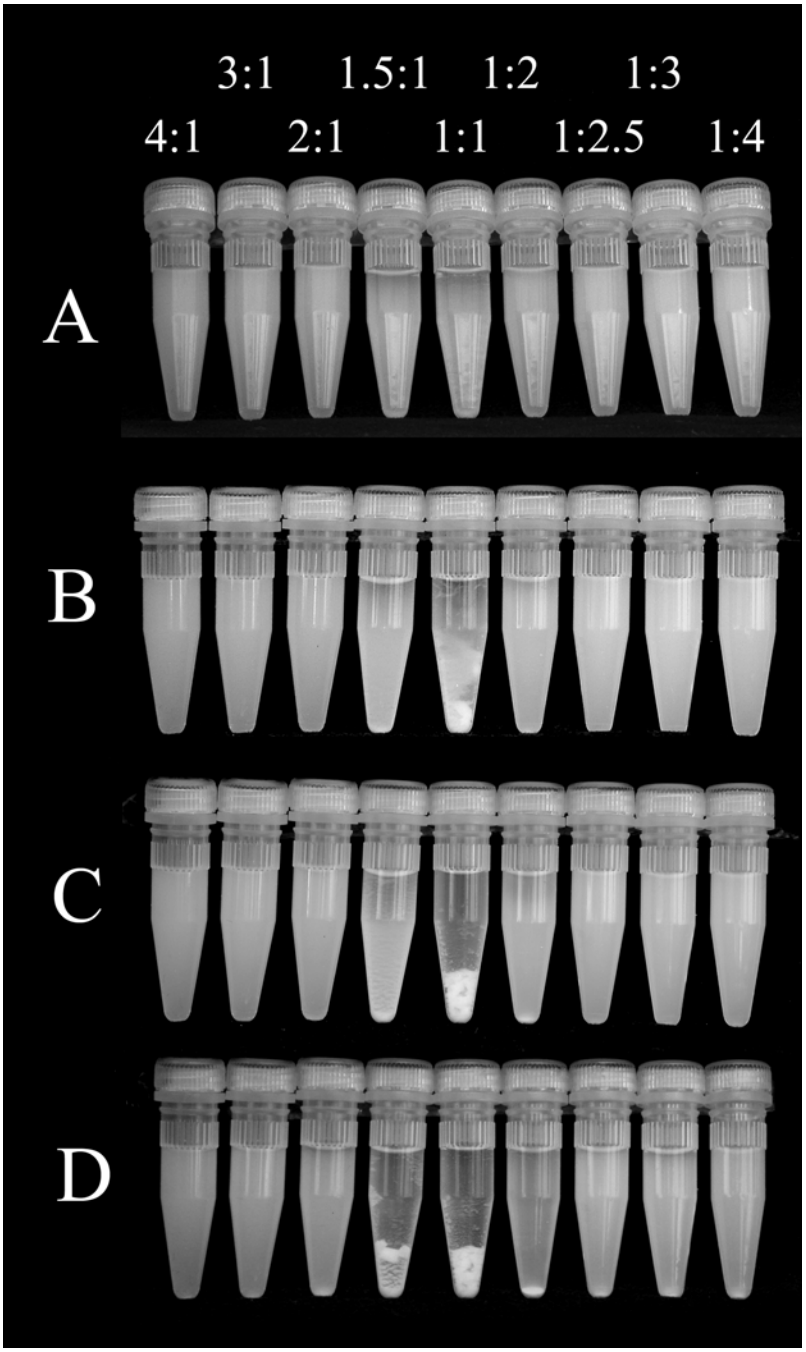

Figure 9.4: Settling experiments results are shown for the 415 nm PS-S and 215 nm PS-QA system. Images are taken at 60, 90, 250, and 1200 minutes (A-D, respectively). Note that the 1:1 number ratio settles much more rapidly than other number ratios. From these results, the charge ratio in this system is estimated to be 1:1. This is consistent with the charge ratio calculated using the information in Table 9.1 for this system.

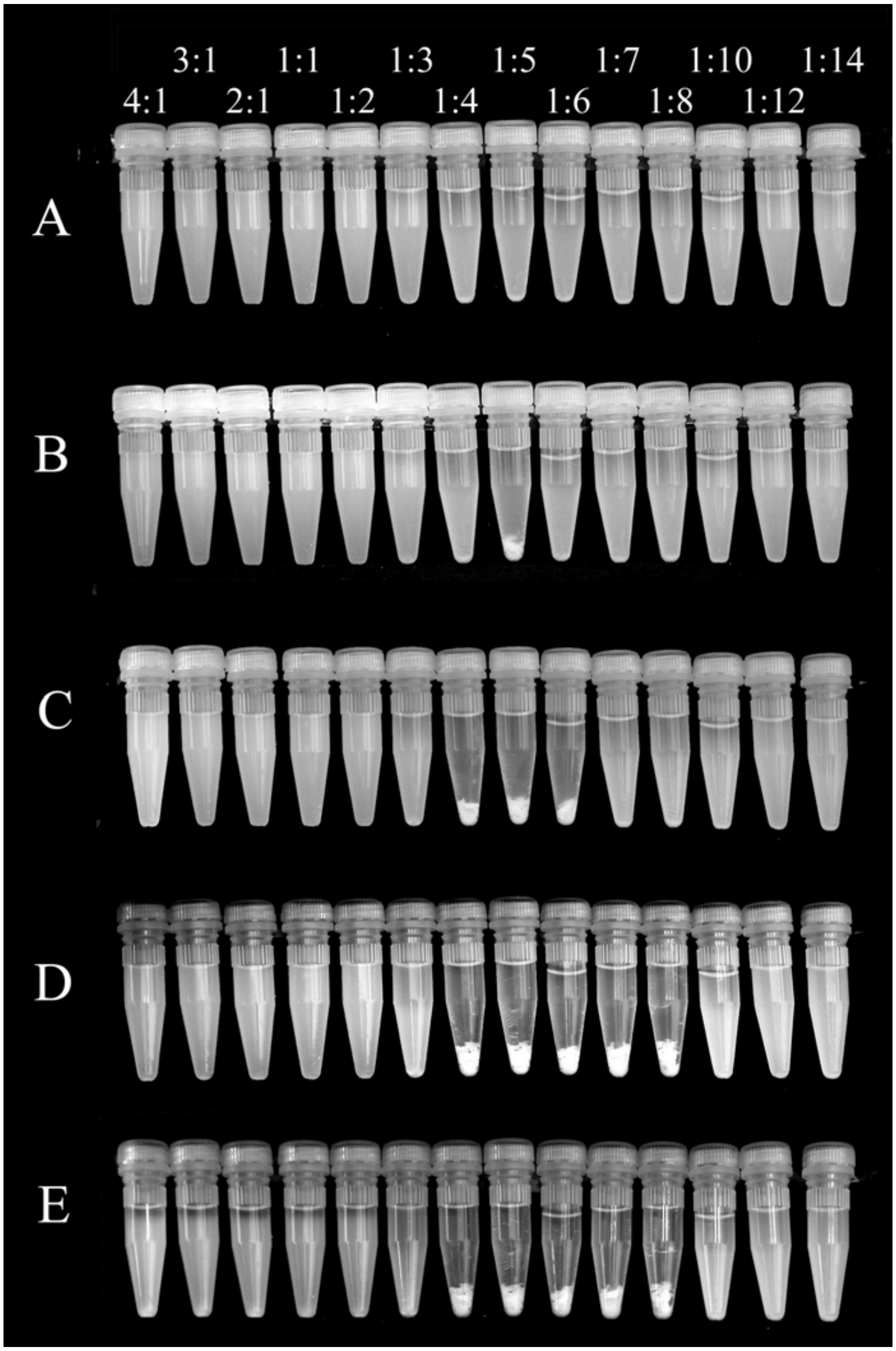

Figure 9.5: The mixing experiment results for the 415 nm PS-S and 749 nm PS-A system are shown. The fastest settling number ratio is at 1:5 (large:small). This indicates that the charge ratio for this system is substantially higher than that in Figure 9.4. Note that this larger particle size system shows heterocoagulation over more samples. The settling times are 90, 120, 200, 350, and 1200 minutes (A-E, respectively). Again, these results are consistent with the calculated charge ratio using Table 9.1.

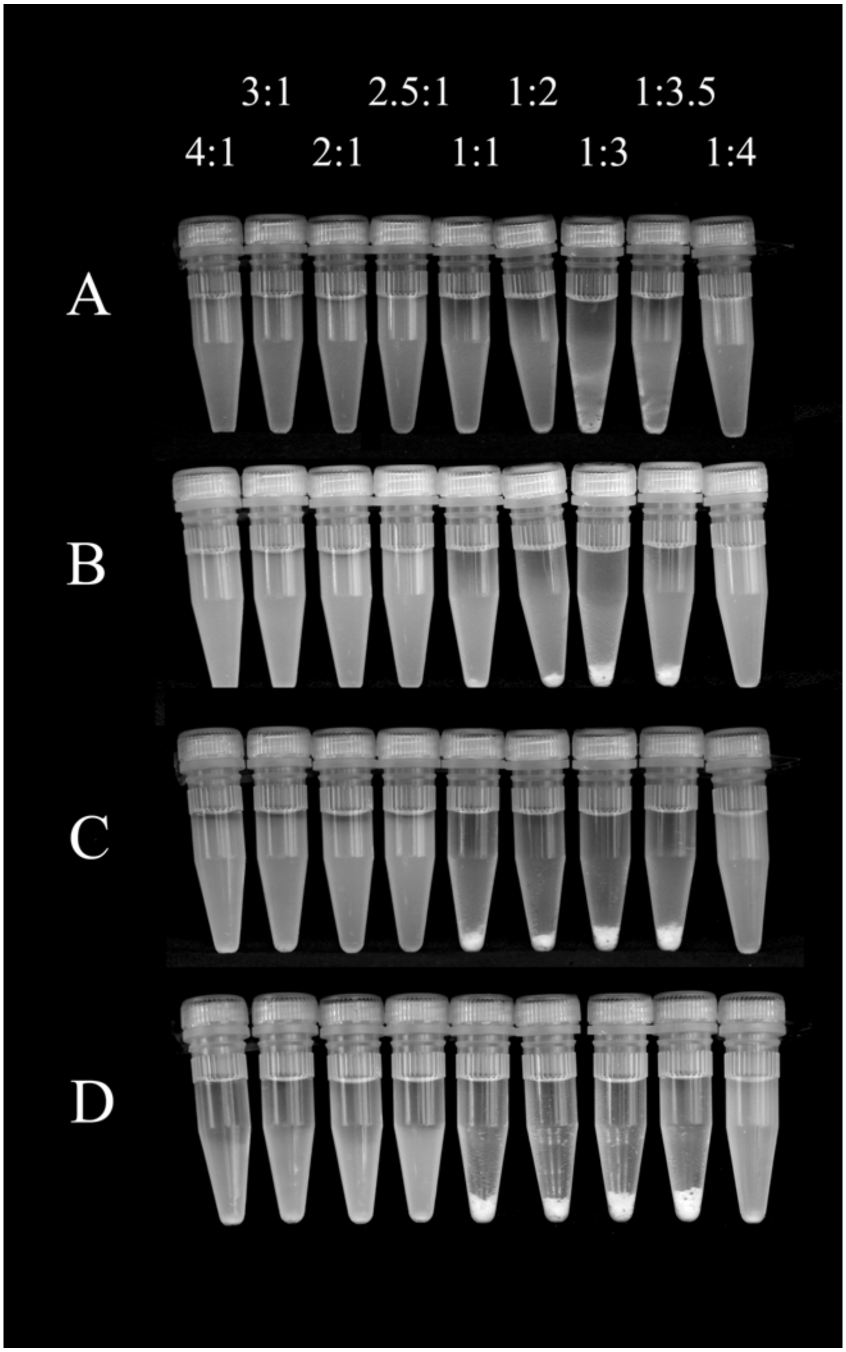

Figure 9.6: The results of mixing experiments for the 749 nm PS-A and 1310 nm PS-S system are shown. The settling times are 120, 200, 350, and 1200 minutes (A-D, respectively). Settling occurs rapidly in all three 2:1, 3:1, and 3.5:1 (large:small) number ratio samples, but may be slightly faster in the 3:1 sample as some heterocoagulation is evident after only 120 minutes. At long times, all samples begin to show signs of settling due to the settling of the large 1310 nm particles. Again, these results are consistent with the calculated charge ratio using Table 9.1.

## 9.4 Discussion of Mixing Experiments

In Chapter 8, it was shown that the lowest energy 1:1 number ratio heterocoagulates form when the surface charges ratio is 1:1. It is proposed here that the lowest energy heterocoagulate for a surface charge ratio other than 1:1 would form when the number ratio would result in a zero net charge.

$$\frac{N_2}{N_1} \rightarrow N_{Ratio} = Q_{Ratio} \leftarrow \frac{\psi_{s,1} a_1 \left(\kappa a_1 + 1\right)}{\psi_{s,2} a_2 \left(\kappa a_2 + 1\right)} \tag{9.1}$$

All possible charge ratios are shown in Figure 9.7. Comparing all three cases that heterocoagulated, a narrow window of Debye parameters can satisfy all three experimental observations. The Debye parameter must be bounded between $2\times10^{6}$ $\mathrm{m}^{-1}$ and $6\times10^{6}$ $\mathrm{m}^{-1}$, which corresponds to salt concentrations between $9.5\times10^{-8}$ and $8.6\times10^{-7}$ mol/L. Recalling from Chapter 5, the lowest possible ionic strength for the 2-propanol was estimated to be $6.7\times10^{-8}$ mol/L. This corresponds to an increase in salt concentration and therefore conductivity of 13 times at most. Using the conductivity of 1% deionized water in 2-propanol, the Debye parameter of the experimental system is found to be approximately $3.75\times10^{6}$ $\mathrm{m}^{-1}$. This is in excellent agreement with the calculation.

From these results, the conclusion is drawn that the surfaces behave as constant charge distribution boundary conditions, as the models explaining their behavior are developed in that context. A system with constant potential boundary conditions would heterocoagulate at all charge ratios due to the infinite potential well in that model. Secondly, it is shown that the colloidal mobility can be significantly relative to the heterocoagulate energy. This mobility is necessary for the formation of ICCs and these results demonstrate the first (to our knowledge) intentional tailoring of electrostatic interactions to bring about varying heterocoagulate behavior.

This experimental setup allows the estimation of ionic strength and charge ratio for a potential ionic colloidal crystal system. Clearly a charge ratio much above three would be undesirable for crystal formation as no potential structures are obvious. The ideal system for further ICC experimentation is the 215/415 system as the charge ratio is very close to 1:1.

As was shown in Chapter 6, the melting and boiling points for a given system can be estimated from the crystal energy. Utilizing the energetics calculation from Chapter 7, the melting points of these potential ICC systems are evaluated. The relation between the crystal energy and the melting point is known for two values of Λ. For Λ=0, the known values of the atomic crystal energy and their melting points give a correlation constant of 0.87 KJ/mol·K. For Λ=3, the results from chapter 7 give a constant of 0.418 KJ/mol·K. Table 9.2 shows the melting points that would result from both known correlation constants for several systems. This allows the actual melting point for each system to be estimated based on the real value of Λ for that system. From the range of melting points shown, two systems have a melting point well below room temperature for a 1:1 mixture. In the case of 415/769 system, this result is due to the high charge asymmetry. However, in the case of the 113/215 system, the result is a combination of the increased importance of charge ratio at low values of Λ, which makes the relatively small charge asymmetry very costly, and the small particle sizes. The other two systems show a melting point that is well above room temperature. The best candidate system appears to be the 215/415 system, however this sytem is still likely to be heavily quenched due to the estimated melting point of between 600 and 1000 K. Ideally, a better charge asymmetry, reduced Λ, and reduced melting point would be required to reduce the melting point further.

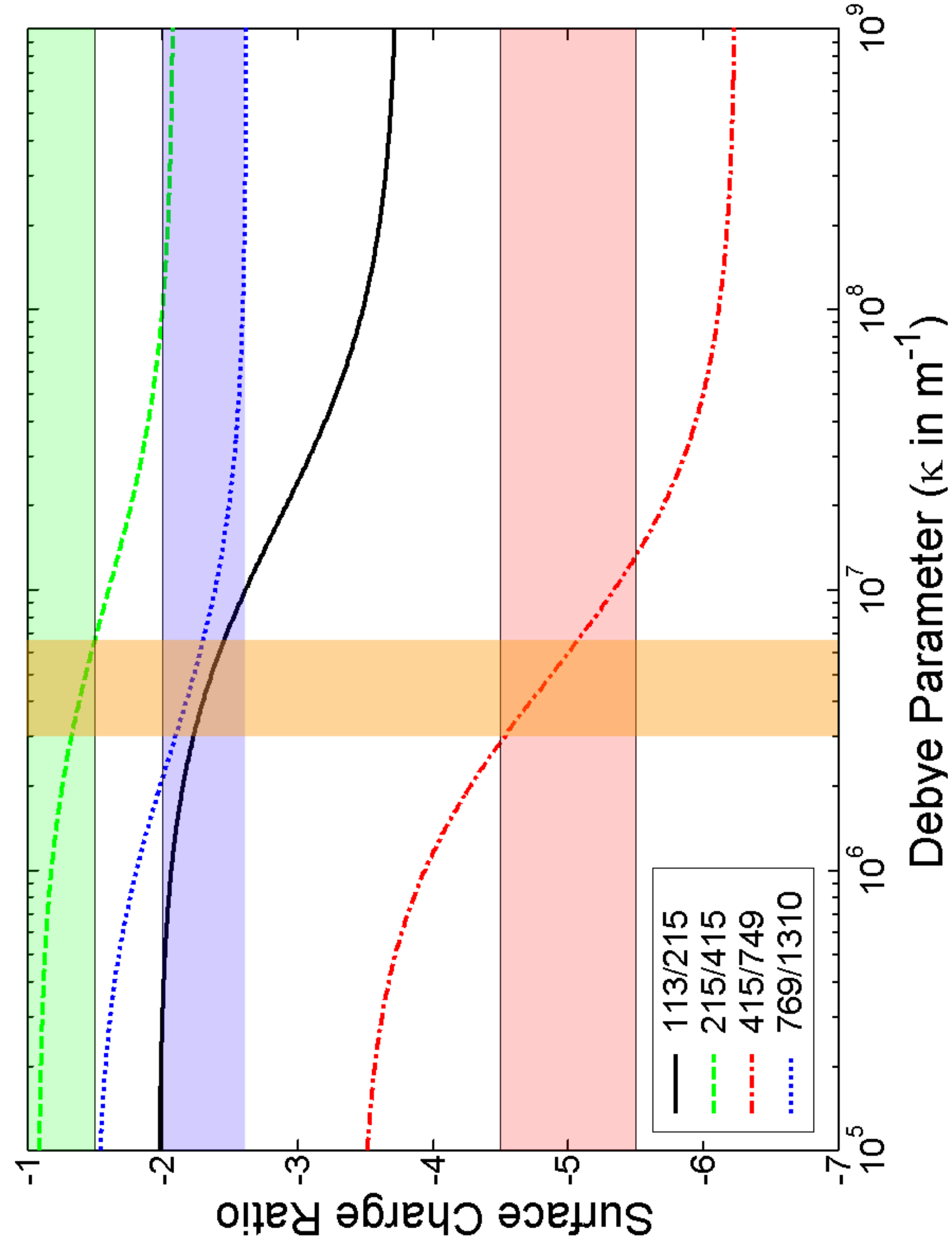

Figure 9.7: Shown are the possible surface charge ratios calculated using the properties from Table 9.1 and Equation 9.1. The constant surface charge ratio bars indicate the combinations that are closest to the inverse of the fastest settling number ratios. No box is drawn for the 113/215 system as no settling was observed despite number ratios in this range being tested. Only the small range between $2\times10^6$ m$^{-1}$ and $6\times10^6$ m$^{-1}$ could meet all of the constraints. The estimated κ value of $3.75\times10^6$ m$^{-1}$ falls directly in the middle of this range.

Table 9.2: The formation energy and estimated critical temperatures are shown for all tested systems forming in an ICC rocksalt structure. Two estimates are taken, the first from atomic systems for low ionic strengths and the second from the Monte Carlo simulations. These results show that two systems are not expected to form large heterocoagulates when mixed in a 1:1 ratio due to a low estimate melting point. These results are confirmed in the experiments in this section. The 215/415 system has a charge asymmetry closest to zero and also has a melting point close to room temperature, making it an ideal candidate for further ICC experimentation.

| System | $\kappa$ (1/m) | $\Lambda$ | Qasym | Formation Energy (kJ/mol) | $\Lambda$=0 Estimate Melting Point (K) | $\Lambda$=3 Estimate Melting Point (K) |
|---|---|---|---|---|---|---|
| **113/215** | 2.0E+06 | 0.33 | -0.78 | 45 | 51 | 110 |
| | 6.0E+06 | 0.98 | -0.91 | 59 | 68 | 146 |
| **215/415** | 2.0E+06 | 0.63 | -0.23 | 458 | 525 | 1131 |
| | 6.0E+06 | 1.89 | -0.39 | 524 | 601 | 1293 |
| **415/769** | 2.0E+06 | 1.16 | -1.59 | -13 | -15 | -31 |
| | 6.0E+06 | 3.49 | -1.79 | 7 | 8 | 17 |
| **769/1310** | 2.0E+06 | 2.06 | -0.70 | 1748 | 2005 | 4316 |
| | 6.0E+06 | 6.18 | -0.85 | 2589 | 2969 | 6393 |

# Chapter 10: Conclusions and Future Work

Ionic colloidal crystals have been explored through the employment of thermodynamic models, Brownian dynamics and Monte Carlo simulations, a Poisson-Boltzmann equation solver, and experimental tests. Through this study, a much more complete picture of ICC formation and heterocoagulation in general has been formed. The problem of ICC formation is effectively reduced to one of engineering appropriate particles to meet the many crystallization constraints on such a system.

A thermodynamic framework is presented that assesses the regions of ICC stability. This framework is developed based on the Yukawa (or LSA) potential. While this is only exact for ion penetrable spheres, this approximate form is later shown to be the most accurate pair potential for a constant charge boundary condition at low ionic strengths. As was detailed in Chapter 4, low ionic strengths are essential for ICC formation. Therefore, the Yukawa potential is currently the best available pair potential to model ICC formation. The Madelung sum framework facilitates the examination of the effect of ionic strength on next-nearest neighbor interactions, showing that a Λ of approximately three or below is necessary for electrostatic interactions to significantly impact long range order. Also, this model enables the study of the effects of dispersity on ICC formation, finding that systems with low CVs are necessary to stabilize ICCs. Finally, the model makes it clear that heterocoagulates may be unstable in systems with highly asymmetric charge ratios at low screening ratios. While later development changed the definition of the charge ratio, the implication that heterocoagulation may not occur due to charge asymmetry has not, to our knowledge, been previously proposed. This result caused the focus of the initial experiments to shift toward selecting particle properties to give a charge ratio around one, with a low CV and low Λ.

The implications of the range of the potential to colloidal ordering has also not been widely explored. For example, Milam et al [103] study DNA-assisted assembly which allows a widely tunable short-range interaction. This interaction only shows either liquid or glassy behavior. These results are explained in this work by the necessity of long range repulsive interactions in creating the mobility necessary for colloidal rearrangement into a crystalline state. Likewise, a system dominated by van der Waals or attractive electrostatic interactions will have no mobility if long range electrostatic repulsion is not present and tuned to allow rearrangement. These results apply to any system where significant rearrangement of colloidal particles is desired.

Preliminary experiments were based on the thermodynamic results discussed above. These experiments showed only small ordered regions. While attempts to increase their size failed, these regions had not been previously observed in heterocoagulating systems. These observations were not believed to be simply the result of random settling as dipole pairs should form immediately in solution resulting in diffusion limited cluster aggregation. Later results show these systems to be deeply undercooled, so rearrangement likely occurred during the settling of the dipole pairs but not after the suspension had densified. Thus, these experiments indicated that more study of the thermodynamics and kinetics was needed to understand the observations.

Brownian dynamics and Monte Carlo simulations were both used to model ICC melting behavior in an effort to understand what parameters must be changed to allow particle rearrangement. While the Brownian dynamics (BD) results gave an unexpectedly close match to atomic behavior, more accurate Monte Carlo (MC) methods showed the expected increase in melting temperature with ionic strength. These results indicate that, despite its widespread use in modeling colloidal behavior, the temperature in BD simulations of dense systems must be rescaled to accurately reflect the true modeled temperature . The MC results can be applied to obtain this rescaling parameter and a more exact prediction of melting behavior can be achieved due to far fewer approximations in that method. The melting point of the early experimental system was determined to be almost 8000 K when rescaled with the Monte Carlo results. Thus, this system was substantially undercooled at room temperature, making ICC formation unlikely due to kinetics. The MC results also revealed a glass transition point at ~87% of the melting point. These result can be used to tailor future experimental systems to assure that crystallites are stable and that enough mobility is present to allow crystallization.

A Poisson-Botlzmann equation solver was implemented in order to more accurately calculate ICC formation energies. This allows experimental systems to be better tailored to meet the narrow crystallization window. The method is shown to be robust and accurate through calculations of test systems with known analytical formation energies. The formation energy of ICCs is calculated and found to be higher than that predicted by the LSA, but lower than that predicted by the Ohshima potential (Yukawa overestimated and Ohshima underestimated the magnitude of the formation energy), especially at low ionic strengths. For high ionic strengths, where most interactions are only nearest-neighbor in nature, the Ohshima potential result more accurately describes the system energy. However, it is important to note that the Yukawa potential more accurately matched the calculated potential at low ionic strengths, where ICC formation is expected to result due to the higher mobility. The calculated result shows that a new potential, perhaps a higher order non-pair-wise potential, would be beneficial for modeling of all dense colloidal systems for intermediate $\Lambda$ regimes. Furthermore, these results provide a framework in which to test new potentials for dense colloidal systems.

For any systems with constant charge boundary conditions, this work gives insight into the choice of appropriate pair potentials in describing colloidal behavior. Again, this work illustrates the importance of modeling any dense colloidal systems or systems with attractive electrostatic interactions with constant charge distribution boundary conditions. The choice of the Yukawa potential for modeling low screening ratio systems (small particle size or low ionic strength), is a result that can be applied generally to the modeling of most electrostatic interactions. However, at higher screening ratios (>~5), the Ohshima potential should be used with enough terms to reach convergence. However, when the screening ratio is greater than 10, the much simpler Wiese-Healy potential accurately models colloidal interactions. Again, the most interesting regimes for self-organization are low ionic strengths as systems will have the largest mobility.

The Poisson-Boltzmann equation solver results also indicate that, for a 1:1 number ratio system, it is necessary to match the surface charges, not the representative point charges, to obtain the most stable system energy. In higher number ratio systems, the product of the number ratio and surface charge ratio should be one, giving an equal amount of positive and negative charges in the system. While this results is not explained by any current colloidal pair potentials, it can be understood by considering a dipole pair in a dense heterocoagulate. If there is an equality of surface charge, the dipole pair is charge neutral. Therefore, adjacent dipole will therefore not repel one another due to net charges, resulting in a more stable system.

The results from the Poisson-Boltzmann solver were experimentally verified by observing the heterocoagulation behavior of several systems with varying charge ratios. Additionally, the results of the Poisson-Boltzmann solver were used to explain why no heterocoagulation was observed in experimental systems that would generally be expected to heterocoagulate based on current heterocoagulation literature. Charge asymmetry becomes increasingly important for low screening ratios. Therefore, as many particulate systems are being used in smaller and smaller sizes, classical heterocoagulation models will no longer be adequate to model these systems. These experimental results also demonstrate that the attraction in an electrostatic system can be lower than thermal energy, resulting in a stable suspension despite attractive electrostatic forces. The ability to tailor mobility in colloidal systems is necessary to obtain crystallization.

This work has shown the importance of identifying and controlling the ionic strength, surface charges, particle sizes, particle dispersities, and the total system energy. The parameters under which ICCs should be stable are very restrictive, making them difficult to obtain. Full realization of the ICC concept will require tailoring of particle systems to obtain low screening ratios, charge ratios near one, melting points near room temperature, and low coefficients of variation. As very small sizes generally have higher CVs, obtaining all three constraints requires further refinement of the emulsion polymerization technique.

Of the systems tested, most exhibited a surface potential of magnitude 80 mV in 2-propanol. As a charge ratio near one is necessary, if the particle system has a size ratio away from one, one particle must have a lower surface potential than the other to obtain a charge ratio near one. This can be achieved by reducing the initiator concentration and thereby reducing the available charging groups. However, this change must not come about with an increased CV.

It is also difficult to maintain low CVs while still achieving both a charge ratio of one and a near-room-temperature melting point. For example, the 215 nm quaternary amine particles were unable to be reproduced by the manufacturer upon repeated efforts. Low CVs in similar systems could only be obtained for sizes around 500 nm. Clearly these particles are possible to produce, however unknown conditions prevent them from being made again easily. A better understanding of these conditions would allow many batches with these properties to be produced.

One remaining question regarding particle fabrication is the impact of any variations in charge distributions across the surface and between particles. Currently no means of measuring the distribution of zeta potentials in a colloidal system is feasible, making an assessment of experimental systems in this regard currently impossible. Similar to the CV, a variation of less than 3% should be targeted.

Future systems could incorporate ultrapure water as the κ value is very similar to that of the 2-propanol used. This would greatly simplify processing, as dialysis could be done simply against the ultrapure water. However, it is necessary to assure that the conductivity of the final solution remains very close to 18.2 MΩ-cm. Also, the increased bond strength due to an increased dielectric constant must be compensated by reducing the particle size. Finally, a freeze drying approach could be used to combat the strong forces present in the drying front of water, allowing examination of the state in which the particles settled while in solution. This approach was not used with the 2-propanol because freeze drying of 2-propanol is extremely difficult due to its very low freezing point and the resulting low sublimation rate.

Summarizing the constraints that have been developed throughout this work, an ideal system would have a value of $\Lambda$ below approximately three. The charge ratio (as defined by Equation 8.16) should be very close to the ideal ratio for the structure targeted (i.e. 1:1 for rocksalt). Kinetically, it is important to target a system where room temperature is between the glass transition temperature and the melting point. At $\Lambda=3$, this corresponds to a system that has a bond strength between approximately 90 and 120 kJ/mol. For $\Lambda=0$, this corresponds to a bond strength between approximately 180 and 240 kJ/mol. Additionally, flow fields or centrifugation forces can be used to aid nucleation if necessary.

Furthermore, the effect of monodispersity can be analysed under the model developed in Chapter 8. A coefficient of variation of 3% on both particles will vary a starting charge ratio of 1 from 0.94 to 1.06 at $\Lambda<<1$, and from 0.89 to 1.11 for large $\Lambda$. However, the impact on the crystal energy is very different, where at low $\Lambda$ some charge ratio combinations may be unstable, while large screening ratio systems will have a much wider stability field with respect to charge asymmetry.

Despite the proven difficulty in fabricating ICCs, the potential technological advancements they offer make their continued study worthwhile. Combinatorial mixing experiments, such as those posed in Chapter 9, should be used to identify systems with useful charge ratios. Ideally, particle systems will be produced cheaply in large quantities so that sufficient material remains after mixing experiments to allow many variations of experimental conditions. Further calculations should be done to evaluate a potential that can represent dense colloidal suspensions. This will allow the prediction of nucleation barriers, aiding the further tailoring of ICC fabrication.

# Bibliography

---

1. Xia, Y.N., B. Gates, and Z.Y. Li, *Self-assembly approaches to three-dimensional photonic crystals.* Advanced Materials, 2001. **13**(6): p. 409-413.
2. Stein, A. and R.C. Schroden, *Colloidal crystal templating of three-dimensionally ordered macroporous solids: materials for photonics and beyond.* Current Opinion in Solid State & Materials Science, 2001. **5**(6): p. 553-564.
3. Bardosova, M. and R.H. Tredgold, *Ordered layers of monodispersive colloids.* Journal of Materials Chemistry, 2002. **12**(10): p. 2835-2842.
4. Simeonov, S., U. Bass, and A.R. McGurn, *Photonic band structure of zinc blende type periodic dielectric media.* Physica B, 1996. **228**(3-4): p. 245-250.
5. Yoshino, K., et al., *Spectral narrowing of photoluminescence in conducting polymer and fluorescent dyes infiltrated in photonic crystal, synthetic opal.* Japanese Journal of Applied Physics Part 2-Letters, 1998. **37**(10A): p. L1187-L1189.
6. Shkunov, M.N., et al., *Tunable, gap-state lasing in switcbable directions for opal photonic crystals.* Advanced Functional Materials, 2002. **12**(1): p. 21-26.
7. Polson, R.C., A. Chipouline, and Z.V. Vardeny, *Random lasing in pi-conjugated films and infiltrated opals.* Advanced Materials, 2001. **13**(10): p. 760-764.
8. Shkunov, M.N., et al., *Photonic versus random lasing in opal single crystals.* Synthetic Metals, 2001. **116**(1-3): p. 485-491.
9. Frolov, S.V., et al., *Laser-like emission in opal photonic crystals.* Optics Communications, 1999. **162**(4-6): p. 241-246.
10. Yoshino, K., et al., *Amplified spontaneous emission and lasing in conducting polymers and fluorescent dyes in opals as photonic crystals.* Applied Physics Letters, 1999. **74**(18): p. 2590-2592.
11. Scott, R.W.J., et al., *Electronically addressable SnO2 inverted opal gas sensors fabricated on interdigitated gold microelectrodes.* Chemical Communications, 2003(6): p. 688-689.
12. Sharma, A.C., et al., *A general photonic crystal sensing motif: Creatinine in bodily fluids.* Journal of the American Chemical Society, 2004. **126**(9): p. 2971-2977.
13. Asher, S.A., et al., *Photonic crystal aqueous metal cation sensing materials.* Analytical Chemistry, 2003. **75**(7): p. 1676-1683.
14. Velikov, K.P., et al., *Layer-by-layer growth of binary colloidal crystals.* Science, 2002. **296**(5565): p. 106-109.
15. Bartlett, P., R.H. Ottewill, and P.N. Pusey, *Freezing of Binary-Mixtures of Colloidal Hard-Spheres.* Journal of Chemical Physics, 1990. **93**(2): p. 1299-1312.

16. Schofield, A.B., *Binary hard-sphere crystals with the cesium chloride structure.* Physical Review E, 2001. **6405**(5): p. art. no.-051403.
17. Hunt, N., R. Jardine, and P. Bartlett, *Superlattice formation in mixtures of hard-sphere colloids.* Physical Review E, 2000. **62**(1): p. 900-913.
18. Trizac, E., M.D. Eldridge, and P.A. Madden, *Stability of the AB crystal for asymmetric binary hard sphere mixtures.* Molecular Physics, 1997. **90**(4): p. 675-678.
19. Underwood, S.M., W. Vanmegen, and P.N. Pusey, *Observation of Colloidal Crystals with the Cesium-Chloride Structure.* Physica A, 1995. **221**(4): p. 438-444.
20. Eldridge, M.D., et al., *Binary Hard-Sphere Mixtures - a Comparison between Computer-Simulation and Experiment.* Molecular Physics, 1995. **84**(2): p. 395-420.
21. Pusey, P.N., et al., *Phase-Behavior and Structure of Colloidal Suspensions.* Journal of Physics-Condensed Matter, 1994. **6**: p. A29-A36.
22. Bartlett, P. and P.N. Pusey, *Freezing of Binary-Mixtures of Hard-Sphere Colloids.* Physica A, 1993. **194**(1-4): p. 415-423.
23. Bartlett, P., R.H. Ottewill, and P.N. Pusey, *Superlattice Formation in Binary-Mixtures of Hard-Sphere Colloids.* Physical Review Letters, 1992. **68**(25): p. 3801-3804.
24. AlSunaidi, A., et al., *Cluster-cluster aggregation in binary mixtures.* Physical Review E, 2000. **61**(1): p. 550-556.
25. Fernandez-Nieves, A., et al., *Structure formation from mesoscopic soft particles.* Physical Review E, 2001. **6405**(5): p. art. no.-051603.
26. Kim, A.Y. and J.C. Berg, *Fractal aggregation: Scaling of fractal dimension with stability ratio.* Langmuir, 2000. **16**(5): p. 2101-2104.
27. Hunter, R.J., *Foundations of colloid science*. 2nd ed. 2001, Oxford New York: Oxford University Press. xii, 806.
28. Hiemenz, P.C. and R. Rajagopalan, *Principles of colloid and surface chemistry*. 3rd , rev. and expanded / ed. 1997, New York: Marcel Dekker. xix, 650.
29. Adamson, A.W. and A.P. Gast, *Physical chemistry of surfaces*. 6th ed. 1997, New York: Wiley. xxi, 784.
30. Israelachvili, J.N., *Intermolecular and surface forces*. 2nd ed. 1991, London San Diego: Academic Press. xxi, 450.
31. Shaw, D.J., *Introduction to colloid and surface chemistry*. 4th ed. 1992, Oxford Boston: Butterworth-Heinemann. vi, 306.
32. Myers, D., *Surfaces, interfaces, and colloids : principles and applications*. 2nd ed. 1999, New York: Wiley-VCH. xx, 501.
33. Stokes, R.J. and D.F. Evans, *Fundamentals of interfacial engineering*. Advances in interfacial engineering series. 1997, New York: Wiley-VCH. xxviii, 701.
34. Russel, W.B., D.A. Saville, and W.R. Schowalter, *Colloidal dispersions*. Cambridge monographs on mechanics and applied mathematics. 1989, Cambridge New York: Cambridge University Press. xvii, 525 , [1] leaf of plates.
35. Trau, M., *Optical Barcoding of Colloidal Suspensions: Applications in Genomics, Proteomics and Drug Discovery.* Chemical Communications, 2002. **14**: p. 1435-1441.

36. Wong, S., V. Kitaev, and G.A. Ozin, *Colloidal crystal films: Advances in universality and perfection.* Journal of the American Chemical Society, 2003. **125**(50): p. 15589-15598.
37. French, R.H., *Origins and Applications of London Dispersion Forces and Hamaker Constants in Ceramics.* Journal of the American Ceramic Society, 2000. **83**(9): p. 2117-2146.
38. Keesom, W.H., *On the Deduction of the Equation of State from Boltzmann's Entropy Principle.* Communications Physical Laboratory, 1912. University of Leiden Supplement 24a to No. 121-132: p. 3-20.
39. Keesom, W.H., *On the Deduction from Boltzmann's Entropy Pinciple of the Second Virial Coefficient fro Materials Partilces (in the Limit of Rigid Spheres of Central Symmetry) which Exert Central Forces Upon Each Other and for Rigid Spheres of Central Symmetry Containing an Electric Doublet at Their Centers.* Communications Physical Laboratory, 1912. University of Leiden Supplement 24b to No. 121-132: p. 23-41.
40. Keesom, W.H., *On the Second Virial Coefficient for Di-atomic Gases.* Communications Physical Laboratory, 1912. University of Leiden Supplement 25 to No. 121-132: p. 3-19.
41. Debye, P.J.W., *Molekularkrafte und ihre Elektrische Deutung.* Physikalische Zeitschrift, 1921. **22**: p. 302-308.
42. Debye, P.J.W., *Die van der Waalsschen Kohasionskrafte.* Physikalische Zeitschrift, 1920. **21**: p. 178-187.
43. London, F., *The General Theory of Molecular Forces.* Transactions of the Faraday Society, 1937. **33**: p. 8-26.
44. London, F., *Zur Theorie und Systematik der Molekularkrafte.* Zeitschrift fur Physik, 1930. **63**: p. 245-279.
45. Hamaker, H.C., *The London-van der Waals Attraction between Spherical Particles.* Physica, 1937. **4**(10): p. 1058-1072.
46. Hough, D.B. and L.R. White, Advances in Colloid and Interface Science, 1980. **14**: p. 3-41.
47. Pailthrope, B.A. and W. Russel, Journal of Colloid and Interface Science, 1982. **89**: p. 563-566.
48. Ninham, B.W. and V.A. Parsegian, Biophysical Journal, 1970. **10**: p. 646.
49. Tabor, D. and R.H.S. Winterton, *The Direct Measurement of Normal and Retarded van der Waals Forces.* Proc. R. Soc. London A, 1969. **312**: p. 435-450.
50. Velasco, E., G. Navascues, and L. Mederos, *Phase behavior of binary hard-sphere mixtures from perturbation theory.* Physical Review E, 1999. **60**(3): p. 3158-3164.
51. Urakami, N. and M. Imai, *Dependence on sphere size of the phase behavior of mixtures of rods and spheres.* Journal of Chemical Physics, 2003. **119**(4): p. 2463-2470.
52. Tuinier, R., J. Rieger, and C.G. de Kruif, *Depletion-induced phase separation in colloid-polymer mixtures.* Advances in Colloid and Interface Science, 2003. **103**(1): p. 1-31.

53. Shah, S.A., et al., *Phase behavior and concentration fluctuations in suspensions of hard spheres and nearly ideal polymers.* Journal of Chemical Physics, 2003. **118**(7): p. 3350-3361.
54. Roth, R., R. Evans, and S. Dietrich, *Depletion potential in hard-sphere mixtures: Theory and applications.* Physical Review E, 2000. **62**(4): p. 5360-5377.
55. Einstein, A., Ann. Physik, 1906. **19**: p. 371.
56. Smoluchowski, M.V., Ann. Physik, 1906. **21**: p. 756.
57. Balluffi, R., S.M. Allen, W.C. Carter, Kinetic Processes in Materials, February 2, 2002 preprint edition, John Wiley & Sons, 1997-2002.
58. Gouy, G., J. Phys. Radium, 1910. **9**: p. 457.
59. Chapman, D.L., Phil. Mag., 1913. **25**: p. 475.
60. S. H. Behrens, M.B., *Exact Poisson-Boltzmann solution for the interaction of dissimilar charge-regulating surfaces.* Physical Review E, 1999. **60**(6): p. 7040-7048.
61. Biesheuvel, P.M., *Dynamic Charge Regulation Model for the Electrostatic Forces between Ionizable Materials.* Langmuir, 2002. **18**: p. 5566-5571.
62. Ohshima, H., *Electrostatic Intreraction between Two Spherical Colloidal Particles.* Journal of Colloid and Interface Science, 1994. **53**: p. 77-102.
63. Eric W. Weisstein, e.a., *"Uniqueness Theorem"*, From MathWorld--A Wolfram Web Resource.
64. Ohshima, H., *Electrostatic Interaction between Two Dissimilar Spheres: Image-Interaction Correction to the Linear Superposition Approximation.* Journal of Colloid and Interface Science, 1995. **176**: p. 7-16.
65. Ohshima, H., *Electrostatic Interaction between Two Dissimilar Spheres with Constant Surface Charge Density.* Journal of Colloid and Interface Science, 1995. **170**: p. 432-439.
66. Kuhn, P.S., et al., *Melting of a colloidal crystal.* Physica a-Statistical Mechanics and Its Applications, 1997. **247**(1-4): p. 235-246.
67. Fu, D., et al., *Study on osmotic pressure and liquid-liquid equilibria for micelle, colloid and microemulsion systems by Yukawa potential.* Chinese Journal of Chemistry, 2004. **22**(7): p. 627-637.
68. Hoy, R.S. and M.O. Robbins, *Fcc-bcc transition for Yukawa interactions determined by applied strain deformation.* Physical Review E, 2004. **69**(5).
69. Dobnikar, J., et al., *Poisson-Boltzmann Brownian dynamics of charged colloids in suspension.* Computer Physics Communications, 2004. **159**(2): p. 73-92.
70. Tavares, F.W. and J.M. Prausnitz, *Analytic calculation of phase diagrams for solutions containing colloids or globular proteins.* Colloid and Polymer Science, 2004. **282**(6): p. 620-632.
71. Chen, Y., *Effect of size polydispersity on melting of charged colloidal systems.* Chinese Physics Letters, 2003. **20**(9): p. 1626-1629.
72. Schmitz, K.S., A.K. Mukherjee, and L.B. Bhuiyan, *Screened Coulomb pair potential in colloidal interactions in suspensions revisited.* Journal of Physical Chemistry B, 2003. **107**(37): p. 10040-10047.
73. Yeomans-Reyna, L., et al., *Self-consistent theory of collective Brownian dynamics: Theory versus simulation.* Physical Review E, 2003. **67**(2).

74. Petris, S.N., et al., *Modeling the structure of charged binary colloidal dispersions.* Langmuir, 2003. **19**(4): p. 1121-1126.
75. Lai, S.K. and K.L. Wu, *Liquid-liquid and liquid-solid phase separation and flocculation for a charged colloidal dispersion.* Physical Review E, 2002. **66**(4).
76. Auer, S. and D. Frenkel, *Crystallization of weakly charged colloidal spheres: a numerical study.* Journal of Physics-Condensed Matter, 2002. **14**(33): p. 7667-7680.
77. Dzubiella, J., G.P. Hoffmann, and H. Lowen, *Lane formation in colloidal mixtures driven by an external field.* Physical Review E, 2002. **65**(2).
78. Yeomans-Reyna, L. and M. Medina-Noyola, *Self-consistent generalized Langevin equation for colloid dynamics.* Physical Review E, 2001. **64**(6).
79. Pesche, R. and G. Nagele, *Dynamical properties of wall-confined colloids.* Europhysics Letters, 2000. **51**(5): p. 584-589.
80. Lowen, H. and G.P. Hoffmann, *Melting of polydisperse colloidal crystals in nonequilibrium.* Physical Review E, 1999. **60**(3): p. 3009-3014.
81. Branka, A.C. and D.M. Heyes, *Algorithms for Brownian dynamics computer simulations: Multivariable case.* Physical Review E, 1999. **60**(2): p. 2381-2387.
82. Hogg, R., Healy T.W., and Fuerstenau D.W., *Mutual Coagulation of Colloidal Dispersions.* Transactions of the Faraday Society, 1966. **62**(6): p. 1638-1651.
83. Derjaguin, B.V., Discussions of the Faraday Society, 1954. **18**: p. 85.
84. Devereux, O.F. and P.L. De Bruyn, *Interaction of plane-parallel double layers.* 1963, Cambridge, Mass.: M. I. T. Press. 361.
85. Derjaguin, B.V., Kolloid-Z., 1934. **69**: p. 155.
86. Verwey, E.J.W., J.T.G. Overbeek, and K. van Nes, *Theory of the stability of lyophobic colloids; the interaction of sol particles having an electric double layer.* 1948, New York,: Elsevier Pub. Co. xi, 205.
87. Wiese, G.R. and T.W. Healy, Transactions of the Faraday Society, 1970. **66**: p. 490.
88. Islam, A.M., B.Z. Chowdhry, M.J. Snowden, Advances in Colloid and Interface Science, 1995. **62**: p. 109-136.
89. Stern, O., Z. Elektrochem., 1924. **30**: p. 508.
90. Huckel, E., Physik. Z., 1924. **25**: p. 204.
91. Smoluchowski, M.V., *Handbuch der Electrizitat und des Magnetismus.* Vol. 2. 1921, Barth, Leipzig.
92. Henry, D.C., Proc. Roy. Soc., 1931. **A133**: p. 106.
93. Wiersma P.H., L.A.L., and Overbeek J.T.G., J. Colloid Interface Sci., 1966. **22**: p. 78.
94. Landau, D.a., Acta physicochim, 1941. **14**: p. 633.
95. Sogami, I.I., N., *On the electrostatic interaction in macroionic solutions.* Journal of Chemical Physics, 1984. **81**(12): p. 6320-6332.
96. Bergstrom, L., *Hamaker constants of inorganic materials.* Advances in Colloid and Interface Science, 1997. **70**: p. 125-169.
97. Dagastine, R.R., D.C. Prieve, and L.R. White, *Calculations of van der Waals forces in 2-dimensionally anisotropic materials and its application to carbon black.* Journal of Colloid and Interface Science, 2002. **249**(1): p. 78-83.

98. Dagastine, R.R., D.C. Prieve, and L.R. White, *The dielectric function for water and its application to van der Waals forces.* Journal of Colloid and Interface Science, 2000. **231**(2): p. 351-358.
99. J.R. Krivacic and D.W. Urry, *Ultraviolet and Visible Refractive Indices of Spectro-Quality Solvents.* Analytical Chemistry, 1970. **42**(6): p. 596-599.
100. Caccamo, C., D. Costa, and G. Pellicane, *A comprehensive study of the phase diagram of symmetrical hard-core Yukawa mixtures.* Journal of Chemical Physics, 1998. **109**(11): p. 4498-4507.
101. Zhou, S.Q., *Solid-liquid phase transition of the hard-core attractive Yukawa system and its colloidal implication.* Journal of Physical Chemistry B, 2004. **108**(24): p. 8447-8451.
102. Trokhymchuk, A., et al., *Liquid-vapor coexistence in the screened Coulomb (Yukawa) hard sphere binary mixture in disordered porous media: The mean spherical approximation.* Journal of Colloid and Interface Science, 1998. **207**(2): p. 379-385.
103. Milam, V.T., et al., *DNA-driven assembly of bidisperse, micron-sized colloids.* Langmuir, 2003. **19**(24): p. 10317-10323.
104. Pauling, L., *The Nature of the Chemical Bond and the Structure of Molecules and Crystals: an Introduction to Modern Structural Chemistry*. 3 ed. 1960, Ithaca, NY: Cornell Univ. Press.
105. Wu, Y.C., and P.A. Berezansky, *Low Electrolytic Conductivity Standards.* Journal of Research of the National Institute of Standards and Technology, 1995. **100**(5): p. 521-528.
106. Stober, W., A. Fink, E Bohn, *Controlled growth of monodisperse silica spheres in the micron size range.* J. Colloid Interface Sci., 1968. **26**(1): p. 62-69.
107. Satoh, A., *Introduction to molecular-microsimulation of colloidal dispersions*. Studies in interface science, v. 17. 2003, Amsterdam: Elsevier. xvii, 344.
108. Verlet, L., *Computer 'experiments' on classical fluids. I. Thermodynamical properties of Lennard-Jones molecules.* Physical Review, 1967. **159**: p. 98-103.
109. Gear, C.W., *Numerical initial value problems in ordinary diffrential equations*. 1971, Englewood Cliffs, NJ: Prentice-Hall.
110. Press, W.H., *Numerical recipes in C++ : the art of scientific computing*. 2nd ed. 2002, Cambridge, UK New York: Cambridge University Press. xxvii, 1002.
111. Schulten, K., and I. Kosztin, *Lectures in Theoretical Biophysics*. 2000, Department of Physics and Beckman Institute.
112. Allen, M.P. and D.J. Tildesley, *Computer simulation of liquids*. 1987, Oxford Oxfordshire New York: Clarendon Press ; Oxford University Press. xix, 385.
113. Buffat, Ph., and J.-P. Borel, *Size effect on the melting temperature of gold particles.* Physical Review A, 1976. **13**(6): p. 2287-2298.
114. Goldstein, A.N., C.M. Echer, A.P. Alivisatos, *Melting in semiconductor nanocrystals.* Science, 1992. **256**(5062): p. 1425-1427.
115. Bishop, C.M., *Continuum Models for Intergranular Films in Silicon Nitride and Comparison to Atomistic Simulations*, in *Materials Science and Engineering*. 2003, Massachusetts Institute of Technology: Cambridge, MA. p. 155.
116. Sutton, A.P., *Modelling of atomic and electronic structures of interfaces.* Materials Research Society Proceedings, 1988. **122**: p. 81-96.

117. Nguyen T., H.P.S., Kwok T., Nitta C., Yip S., *Thermal structural disorder and melting at a crystalline interface.* Physical Review B, 1992. **46**(10): p. 6050-6060.

118. Metropolis, N., A.W. Rosenbluth, M.N. Rosenbluth, A.N. Teller, and E. Teller, *Equation of state calculations by fast computing machines.* Journal of Chemical Physics, 1953. **21**: p. 1087-1092.

119. Frenkel, D. and B. Smit, *Understanding molecular simulation : from algorithms to applications*. 2nd ed. 2002, San Diego, Calif. London: Academic. xxii, 638.